



MEASUREMENTS OF NEUTRAL KAON DECAYS TO
TWO ELECTRON-POSITRON PAIRS

BY EVA HALKIADAKIS

A dissertation submitted to the
Graduate School—New Brunswick
Rutgers, The State University of New Jersey
in partial fulfillment of the requirements
for the degree of
Doctor of Philosophy
Graduate Program in Physics and Astronomy

Written under the direction of
Sunil V. Somalwar
and approved by

New Brunswick, New Jersey

May, 2001

© 2001

Eva Halkiadakis

ALL RIGHTS RESERVED

ABSTRACT OF THE DISSERTATION

Measurements of Neutral Kaon Decays to Two Electron-Positron Pairs

by Eva Halkiadakis

Dissertation Director: Sunil V. Somalwar

We observed 441 $K_L \rightarrow e^+e^-e^+e^-$ events with a background of 4.2 events in the KTeV/E799II experiment at Fermilab. We present here a measurement of the $K_L \rightarrow e^+e^-e^+e^-$ branching ratio (B), a study of CP symmetry and the first detailed study of the e^+e^- invariant mass spectrum in this decay mode.

We used the e^+e^- mass spectrum in $K_L \rightarrow e^+e^-e^+e^-$ to measure the $K_L\gamma^*\gamma^*$ form factor which sheds light on the structure of $K_L \rightarrow \gamma^*\gamma^*$ transitions. The parameter α_{K^*} of Bergström, Massó and Singer [1] describes the relative strength of an intermediate pseudoscalar decay amplitude and a vector meson decay amplitude. We measured $\alpha_{K^*}^{\text{eff}} = -0.14 \pm 0.16_{\text{stat}} \pm 0.15_{\text{syst}}$, which takes into account both the form factor and radiative effects. This is the first form factor measurement using $K_L \rightarrow e^+e^-e^+e^-$. We also measured $B(K_L \rightarrow e^+e^-e^+e^-) = (3.72 \pm 0.18_{\text{stat}} \pm 0.23_{\text{syst}}) \times 10^{-8}$.

Using the the distribution of the angle between the planes of the e^+e^- pairs, we measured the CP parameters $\beta_{\text{CP}} = -0.23 \pm 0.09_{\text{stat}} \pm 0.02_{\text{syst}}$ and $\gamma_{\text{CP}} = -0.09 \pm 0.09_{\text{stat}} \pm 0.02_{\text{syst}}$ for $M_{ee} > 8\text{MeV}$. The parameter β_{CP} is an indicator of the CP eigenstate of K_L and γ_{CP} measures the amount of CP violation in the decay. We found that the 90% CL limit on $|\gamma_{\text{CP}}|$ is < 0.21 . The CP measurements are based on a restricted sample of 264 events, a factor of 10 more than the previous measurement.

Acknowledgements

I was introduced to the world of experimental particle physics roughly eight years ago thanks to my electromagnetism professor who was looking for a student to work in his lab for a new experiment. The experiment was KTeV and that E&M professor was Sunil Somalwar, my thesis advisor, and the rest is history. I would like to thank Sunil for introducing me to high energy physics and for teaching me how to be a true experimentalist. I am also grateful to have worked on a particle physics experiment from its early stages to its fruition, an opportunity that I realize is very rare.

I am indebted to the entire KTeV collaboration and the Fermilab staff for collecting such beautiful and diverse data and whose hard work contributed to this thesis. It is not possible to thank everyone, however, I would like to acknowledge the following collaborators and friends: Ashkan Alavi-Harati, Theo Alexopoulos, Tony Barker, Angela Bellavance, Marj Corcoran, Greg Graham, Bob Hsiung, Jason LaDue, Vivian O'Dell, Pat Toale, Yau Wah, Bruce Winstein, Herman White, Taku Yamanaka, Eric Zimmerman. The contributions of Tony, Eric and Theo made it possible to turn the results of this analysis into a clear, coherent paper acceptable for publication.

I would also like to thank all my Rutgers colleagues for their immense help over the years: Doug Bergman, Steve Schnetzer, Sunil Somalwar, Bob Stone, Rick Tesarek, Gordon Thomson. Special thanks go to Suzie Averitte, John Belz and Amit Lath; this thesis would not be what it is today without the many discussions we had at New Muon Lab and at Rutgers. I am truly grateful for their advice and their friendship.

These six years of my graduate student life I was lucky to be surrounded by many good friends, old and new. Life would have been particularly difficult and unpleasant without these friends: Angeliki (Kasapidis) Pagliaro, Suzie Averitte, Josh Holden, Bala Subramanian, Tim and Michelle Koeth, Angela Bellavance, Benoit Tremblay, and many

others. Three years ago I had the good fortune to meet Rob Morgan, who has been a great source of support in my life since then.

Finally, I wish to thank my (big) family for always believing in me. I especially wish to thank my parents, Mike and Amalia, for their support and encouragement, which made and continue to make my goals a reality. I hope I have made you proud.

Eva Halkiadakis

New Brunswick, NJ

May 2001

Dedication

To my parents.

Table of Contents

Abstract	ii
Acknowledgements	iii
Dedication	v
List of Tables	xi
List of Figures	xiii
1. Introduction	1
1.1. A Little Bit of History	1
1.2. Overview of the Neutral Kaon System	1
1.3. An Introduction to the $K_L \rightarrow \gamma^{(*)}\gamma^{(*)}$ Family of Decays	3
1.4. Branching Ratio of $K_L \rightarrow e^+e^-e^+e^-$	7
1.4.1. QED Calculation	7
1.4.2. Other Predictions	9
1.4.3. Previous Measurements	12
1.5. CP Studies with $K_L \rightarrow e^+e^-e^+e^-$	13
1.5.1. How to Study CP Symmetry in $K_L \rightarrow e^+e^-e^+e^-$	13
1.5.2. Previous Measurements	15
1.6. Form Factor Models	16
1.7. Thesis Overview	20
2. The KTeV Experiment	22
2.1. The KTeV Beam	22
2.1.1. Primary Proton Beam	23
2.1.2. Secondary K_L Beams	24

2.2.	The KTeV Detector	25
2.2.1.	Decay Volume	27
2.2.2.	Spectrometer	27
	Drift Chambers and Magnet	28
	Spectrometer Anti	31
2.2.3.	Calorimeter	31
	Crystal Array	33
	Readout System	35
	CsI Anti and Collar Anti	36
2.2.4.	TRD's	36
2.2.5.	Trigger Hodoscopes	37
2.2.6.	Lead Wall and the Hadron Anti	38
2.2.7.	Muon System	39
2.2.8.	Accidental Counter	40
3.	Event Selection	42
3.1.	Trigger	42
3.1.1.	Level 1	42
3.1.2.	Level 2	43
	Hit Counting	43
	In-time Pair Finding	43
	Hardware Cluster Counting	44
	Y-track Finding	44
3.1.3.	4TRACK Trigger	44
3.1.4.	Level 3	45
3.2.	Data Reduction	45
3.2.1.	E799 Split	46
3.2.2.	4TRACK Crunch	46

4. Event Reconstruction	48
4.1. Track Finding	48
4.1.1. Hit Pairing	48
4.1.2. X and Y Tracks	51
4.1.3. Drift Chamber Calibration	53
Time-to-Distance Calibration	53
Drift Chamber Alignment	53
4.2. Cluster Finding	56
4.2.1. Hardware and Software Clusters	56
4.2.2. Cluster Energy Calibration	57
4.2.3. Cluster Energy Corrections	58
4.3. Decay Vertex Finding	59
5. Monte Carlo Simulation	61
5.1. Event Generation	61
5.1.1. Kaon Production	61
5.1.2. Kaon Decay	62
5.2. Particle Tracing	63
5.3. Detector Simulation	63
5.3.1. Photon Vetos	63
5.3.2. Drift Chambers	64
5.3.3. Calorimeter	64
5.4. Accidental Activity	65
5.5. Trigger Simulation	66
5.6. Individual Decay Generators	66
5.6.1. Monte Carlo Simulation of $K_L \rightarrow e^+e^-e^+e^-$	67
5.6.2. Monte Carlo Simulation of $K_L \rightarrow \pi^0\pi_D^0\pi_D^0$	67
6. Signal Extraction	69
6.1. Event Signature and Backgrounds to $K_L \rightarrow e^+e^-e^+e^-$	69

6.2.	Selecting Candidate $K_L \rightarrow e^+e^-e^+e^-$ Events	69
6.3.	Signal Events	78
6.4.	Background Estimation in $K_L \rightarrow e^+e^-e^+e^-$	79
6.4.1.	Photon Conversions	80
6.4.2.	Background from $K_L \rightarrow \pi e \nu e e$	83
6.4.3.	Summary of All Backgrounds to $K_L \rightarrow e^+e^-e^+e^-$	85
6.5.	Data vs. Monte Carlo	85
6.6.	Summary of $K_L \rightarrow e^+e^-e^+e^-$ Signal Extraction	89
7.	Normalization Mode	90
7.1.	Event Signatures and Backgrounds to $K_L \rightarrow \pi^0\pi_D^0\pi_D^0$	90
7.2.	Selecting Candidate $K_L \rightarrow \pi^0\pi_D^0\pi_D^0$ Events	90
7.3.	Normalization Events	94
7.4.	Background Estimation in $K_L \rightarrow \pi^0\pi_D^0\pi_D^0$ (Normalization Mode)	95
7.4.1.	Crossover Background	95
7.4.2.	Photon Conversions	103
7.4.3.	Summary of All Backgrounds (Normalization Mode)	106
7.5.	Normalization Mode Summary	107
8.	Form Factor Analysis	108
8.1.	The $K_L \rightarrow e^+e^-e^+e^-$ Form Factor	108
8.1.1.	Fitting for the BMS Form Factor	109
8.1.2.	Fitting for the DIP Form Factor	114
8.1.3.	Fitting for a Linear Form Factor	114
8.1.4.	Sources of Systematic Error for the $K_L \rightarrow e^+e^-e^+e^-$ Form Factor	114
8.1.5.	Results of the $K_L \rightarrow e^+e^-e^+e^-$ Form Factor	122
9.	Branching Ratio Analysis	125
9.1.	The Branching Ratio of $K_L \rightarrow e^+e^-e^+e^-$	125
9.1.1.	Systematic Error Estimates for $B(K_L \rightarrow e^+e^-e^+e^-)$	126

QED Radiative Corrections and Form Factor	126
“Two-part” Studies	128
Specific Systematic Studies	131
9.1.2. Summary of Branching Ratio of $K_L \rightarrow e^+e^-e^+e^-$ Results	132
List of Errors	132
Results	132
10. Angular Distribution Analysis	133
10.1. $K_L \rightarrow e^+e^-e^+e^-$ Angular Distribution	133
10.1.1. M_{ee} Dependence on Angular Distribution	134
10.1.2. Fitting the Acceptance Corrected Angular Distribution	136
10.1.3. Systematic Studies for the $K_L \rightarrow e^+e^-e^+e^-$ Angular Distribution Analysis	143
10.1.4. Results of Angular Distribution Analysis	146
Summary of Errors of β_{CP} and γ_{CP}	146
Results	146
11. Conclusions	148
Appendix A. Log Likelihood Method of Fitting for the Form Factor . .	153
Appendix B. Fitting for BMS Form Factor Using the χ^2 method	155
Appendix C. Fitting for the DIP Form Factor Using the χ^2 method . .	158
C.1. Fitting for the Linear Term α_{DIP}	158
C.2. Fitting for the Quadratic Term β_{DIP}	158
Appendix D. Fitting for a Linear Form Factor Using the χ^2 method . .	162
References	163
Vita	167

List of Tables

1.1. Predictions for the ratio of decay rates $\frac{\Gamma(K_L \rightarrow e^+e^-e^+e^-)}{\Gamma(K_L \rightarrow \gamma\gamma)}$	12
1.2. Predictions for $B(K_L \rightarrow e^+e^-e^+e^-)$	12
2.1. Positions and Dimensions of the Ring Counters.	28
2.2. Positions and Dimensions of the Spectrometer elements.	30
2.3. Positions and Dimensions of the Spectrometer Anti.	33
2.4. Positions and Dimensions of the CIA and CA.	36
6.1. $K_L \rightarrow e^+e^-e^+e^-$ Selection Cuts	79
6.2. Total Number of Signal Mode Events	79
6.3. $K_L \rightarrow e^+e^-e^+e^-$ Conversion Background Estimate	80
6.4. Summary of $K_L \rightarrow e^+e^-e^+e^-$ Backgrounds	85
7.1. $K_L \rightarrow \pi^0\pi_D^0\pi_D^0$ Selection Cuts	94
7.2. Total Number of Normalization Mode Events	95
7.3. $K_L \rightarrow \pi^0\pi_D^0\pi_D^0$ Conversion Background Estimate	106
7.4. Summary of $K_L \rightarrow \pi^0\pi_D^0\pi_D^0$ Backgrounds	106
8.1. Expected values of α_{Taylor} from measurements of α_{K^*} and α_{DIP} using the log likelihood method.	117
8.2. Measurements of α_{Taylor} and $\alpha_{\text{Taylor}}^{\text{eff}}$ using the log likelihood method. . .	117
8.3. Form Factor Systematic Studies	120
8.4. Table of Errors for Form Factor Measurements.	122
9.1. Branching Ratio with and without radiative corrections in MC Acceptance.	128
9.2. Branching Ratio Systematic Studies	131
9.3. Table of Branching Ratio Errors	132
10.1. β_{CP} and γ_{CP} with different MC used for acceptance.	143
10.2. Systematic Studies of Angular Distribution	145

10.3. Table of Errors on Angular Distribution Measurements	146
C.1. Table of DIP Form Factor Parameters vs. χ^2	161
D.1. Expected values of α_{Taylor} from measurements of α_{K^*} and α_{DIP} using the χ^2 method.	162
D.2. Measurements of α_{Taylor} and $\alpha_{\text{Taylor}}^{\text{eff}}$ using the χ^2 method.	162

List of Figures

1.1.	Diagram of $K_L \rightarrow \gamma^* \gamma^* \rightarrow e^+ e^- e^+ e^-$.	4
1.2.	The Feynman diagrams for $K_L \rightarrow \gamma^{(*)} \gamma^{(*)}$.	5
1.3.	Short-Distance Feynman diagrams of $K_L \rightarrow \mu^+ \mu^-$.	6
1.4.	Long-Distance Feynman diagram of $K_L \rightarrow \mu^+ \mu^-$.	6
1.5.	The Feynman diagrams for $K_L \rightarrow e^+ e^- e^+ e^-$.	7
1.6.	Vector Meson Dominance diagram.	10
1.7.	Long-distance pole diagram with a vector-vector transition.	18
1.8.	The form factor as a function of x for different values of α_{K^*} .	19
2.1.	Fermilab fixed-target area schematic.	23
2.2.	The KTeV beam elements.	24
2.3.	The KTeV E799-II detector.	26
2.4.	A sketch of a Ring Counter.	28
2.5.	The Spectrometer elements.	29
2.6.	The configuration of the planes and wires within a DC.	32
2.7.	A sketch of a Spectrometer Anti.	33
2.8.	Schematic of the CsI Calorimeter.	34
2.9.	Schematic of the Collar Anti.	37
2.10.	Schematic of the trigger hodoscopes.	38
2.11.	Schematic of the Hadron Anti.	39
2.12.	Schematic of the Muon System counters.	41
4.1.	Illustration of different SOD categories.	49
4.2.	SOD distribution.	50
4.3.	Illustration of a corkscrew rotation.	54
4.4.	E/p distribution before and after the energy calibration.	57

5.1. Generated kaon momentum and decay Z position.	62
6.1. Events vs. Run Number for Signal Mode Events.	70
6.2. E/P distribution for normalization events.	71
6.3. Cluster energy distribution for normalization events.	72
6.4. Maximum Photon Veto energy distributions for normalization events.	72
6.5. Vertex Z position distribution for signal events.	73
6.6. Kaon momentum distribution for signal events.	73
6.7. The distribution of P_T^2 vs. $M_{e^+e^-e^+e^-}$ for signal events.	74
6.8. Vertex χ^2 distribution for normalization events.	75
6.9. Magnet offset χ^2 distribution for normalization events.	75
6.10. The $M_{e^+e^-e^+e^-}$ distribution for signal events.	76
6.11. Event display of a $K_L \rightarrow e^+e^-e^+e^-$ data event.	77
6.12. The distribution of the minimum track separation at DC1 for MC.	81
6.13. Data vs. MC distribution of the minimum track separation at DC1.	82
6.14. $K_L \rightarrow \pi e \nu e e$ background plots.	84
6.15. Vertex Z position distribution for signal events with PHOTOS in the MC.	86
6.16. Kaon momentum distribution for signal events with PHOTOS.	86
6.17. The $M_{e^+e^-e^+e^-}$ distribution for signal events using PHOTOS in the MC.	87
6.18. The $M_{e^+e^-e^+e^-}$ distribution for signal events without radiative corrections in the MC.	88
7.1. Events vs. Run Number for Normalization Mode Events.	91
7.2. Vertex Z position distribution for normalization mode events.	92
7.3. Kaon momentum distribution for normalization mode events.	92
7.4. The distribution of P_T^2 for normalization mode events.	93
7.5. The $M_{e^+e^-e^+e^- \gamma \gamma \gamma \gamma}$ distribution for the normalization mode events.	93
7.6. $m_{\gamma\gamma}$ and m_{eee} for $K_L \rightarrow \pi^0 \pi^0 \pi_{DD}^0$ Monte Carlo.	96
7.7. $m_{\gamma\gamma}$ and $m_{ee\gamma}$ for $K_L \rightarrow \pi^0 \pi_D^0 \pi_D^0$ Monte Carlo.	96
7.8. The best δM_{2D}^2 versus the best δM_{DD}^2	97
7.9. The δM_{DD}^2 and δM_{2D}^2 distributions for for $K_L \rightarrow \pi^0 \pi_D^0 \pi_D^0$ MC.	98

7.10. The δM_{DD}^2 and δM_{2D}^2 distributions for for $K_L \rightarrow \pi^0 \pi^0 \pi_{DD}^0$ MC.	98
7.11. $M_{e^+e^-e^+e^-}$ distribution for eight-body events.	99
7.12. $M_{e^+e^-e^+e^-}$ distribution for eight-body events with normalized MC.	99
7.13. Mass- χ^2 illustration.	100
7.14. $m_{\gamma\gamma}$ and $m_{ee\gamma}$ with normalized MC.	101
7.15. The MC distribution of the minimum track separation at DC1 (normal- ization)	104
7.16. Data vs. MC distribution of the minimum track separation at DC1 (normalization).	105
8.1. The distribution of $x_1 + x_2$	110
8.2. The distribution of $x_1 + x_2$ without radiative corrections in the MC.	110
8.3. The fit value of α_{K^*} from the log likelihood for the 10 MC samples the size of data.	112
8.4. The distribution of the fit value from the log likelihood minus the ex- pected value of -0.36.	112
8.5. The log likelihood as a function of α_{K^*} for data with radiative correction in the MC.	113
8.6. The log likelihood as a function of $\alpha_{K^*}^{\text{eff}}$ for data without radiative cor- rection in the MC.	113
8.7. The log likelihood as a function of the DIP form factor parameter α_{DIP} (with $\beta_{\text{DIP}} = 0.0$) for data.	115
8.8. The log likelihood as a function of the DIP form factor parameter $\alpha_{\text{DIP}}^{\text{eff}}$ (with $\beta_{\text{DIP}} = 0.0$) for data.	115
8.9. Systematic checks for α_{K^*}	116
8.10. The fit of α_{K^*} for the 7 MC samples the size of data that contain PHOTOS.	117
8.11. The fit of α_{K^*} for the 7 MC samples the size of data that contain PHOTOS.	118
8.12. The fit of α_{K^*} for the 10 samples using χ^2	118
8.13. The Poisson χ^2 as a function of α_{K^*} for data for data with PHOTOS radiative corrections in the MC.	120

8.14. The fit value of α_{K^*} from the log likelihood for the 7 MC samples the size of data that contain PHOTOS.	121
8.15. The distribution of $x_1 + x_2$ with our measured value of $\alpha_{K^*}^{\text{eff}}$	124
8.16. The distribution of $x_1 + x_2$ with our measured value of α_{K^*}	124
9.1. $B(K_L \rightarrow e^+e^-e^+e^-)$ vs. $\alpha_{K^*}^{\text{eff}}$	127
9.2. $B(K_L \rightarrow e^+e^-e^+e^-)$ vs. α_{K^*}	127
9.3. “Two-part” study.	129
9.4. Spread of the distribution of the “two-part” study.	129
9.5. “Two-part” study using PHOTOS.	130
9.6. Spread of the distribution of the “two-part” study using PHOTOS.	130
10.1. The RMS from the generated and reconstructed difference in ϕ	135
10.2. The angle ϕ for all generated events.	137
10.3. Fit for β_{CP} and γ_{CP} in bins of M_{ee} (in MeV) in MC at the generation level.	138
10.4. ϕ for generated events with the M_{ee} cut of 8 MeV.	139
10.5. The angular distribution (folded) for the data, without acceptance cor- rection and the acceptance as a function of the angle.	140
10.6. The angular distribution (unfolded) for the data, without acceptance correction and the acceptance as a function of the angle.	141
10.7. The folded and unfolded angular distributions for the acceptance cor- rected data.	142
10.8. Systematic checks on β_{CP} and γ_{CP}	144
11.1. $B(K_L \rightarrow e^+e^-e^+e^-)$ vs. year.	149
11.2. Measurements of $\alpha_{K^*}^{\text{eff}}$ and α_{K^*}	150
11.3. The form factor as a function of x for different results of α_{K^*}	151
B.1. The fit value of α_{K^*} for the 10 samples using χ^2	156
B.2. The distribution of the fit value minus the expected value of -0.36 using χ^2	156

B.3. The Poisson χ^2 as a function of α_{K^*} for data for data with radiative correction in the MC.	157
B.4. The Poisson χ^2 as a function of $\alpha_{K^*}^{\text{eff}}$ for data for data without radiative correction in the MC.	157
C.1. The Poisson χ^2 as a function of the DIP form factor parameter α_{DIP} (with $\beta_{\text{DIP}} = 0.0$) for data.	159
C.2. The Poisson χ^2 as a function of the DIP form factor parameter $\alpha_{\text{DIP}}^{\text{eff}}$ (with $\beta = 0.0$) for data.	159
C.3. The Poisson χ^2 as a function of the DIP form factor parameter β_{DIP} (with $\alpha_{\text{DIP}} = 1.20$) for data.	161

Chapter 1

Introduction

1.1 A Little Bit of History

The world of particle physics contains three discrete symmetries of Nature: charge conjugation (C), space inversion or parity (P) and time reversal (T). One of the most important principles of quantum field theory is the conservation of CPT, or the CPT theorem [2]. In other words, in Nature all interactions are invariant under the combined operation of C, P and T (in no particular order). It used to be thought that all interactions under the operation of CP were also invariant, but this belief changed after the neutral K-meson (kaon) was shown to violate CP symmetry.

The kaon, along with the π -meson (pion), was discovered in cosmic rays in 1947 [3], and many consider their discoveries as the birth of particle physics. In 1957, Wu *et al.* discovered parity violation in weak decays in the famous ^{60}Co experiment [4], verifying the β -decay predictions of Lee and Yang [5]. Then in 1964, the discovery of CP-violation in neutral kaon decays redefined the nature of particle physics. Christenson, Cronin, Fitch and Turley [6] discovered that the long-lived neutral kaon (K_L), which commonly decays to the CP conserving state of three pions, could also decay to two pions and violate CP symmetry with a very small, yet non-zero, probability. This discovery would forever make the kaon one of the most interesting and unique particles observed in Nature.

1.2 Overview of the Neutral Kaon System

The neutral kaon system is described in great detail elsewhere [7, 8, 9, 10], so we present a brief overview here.

There are two neutral kaons, K^0 and \bar{K}^0 , and they are strange mesons. Their valence quark content is

$$\begin{aligned} K^0 &= d\bar{s}, \quad (S = -1), \\ \bar{K}^0 &= \bar{d}s, \quad (S = +1) \end{aligned} \tag{1.1}$$

where S is the strangeness eigenstate value.

K^0 and \bar{K}^0 are not eigenstates of CP . However, when they are operated on by CP we find that they are CP conjugates of each other:

$$\begin{aligned} CP |K^0\rangle &= |\bar{K}^0\rangle, \\ CP |\bar{K}^0\rangle &= |K^0\rangle. \end{aligned} \tag{1.2}$$

We can then define the eigenstates of CP , K_1 and K_2 , as

$$\begin{aligned} |K_1\rangle &= \frac{1}{\sqrt{2}} (|K^0\rangle + |\bar{K}^0\rangle), \\ |K_2\rangle &= \frac{1}{\sqrt{2}} (|K^0\rangle - |\bar{K}^0\rangle), \end{aligned} \tag{1.3}$$

so that

$$\begin{aligned} CP |K_1\rangle &= +|K_1\rangle, \quad (CP = +1, \text{even}) \\ CP |K_2\rangle &= -|K_2\rangle \quad (CP = -1, \text{odd}). \end{aligned} \tag{1.4}$$

Prior to 1964, the CP -odd state K_2 used to be identified as K_L and the CP -even state K_1 used to be identified as K_S .

As previously mentioned, the first observation of CP violation was evident in K_L decays to two pions, a CP -even state. This can be explained if we characterize the K_L as mostly the CP -odd state K_2 with a small admixture of the CP -even state K_1 . Then the short-lived neutral kaon, K_S , is expected to become mostly the CP -even state K_1 with a small admixture of the CP -odd state K_2 . In particular,

$$\begin{aligned} |K_L\rangle &= \frac{1}{\sqrt{1+|\epsilon|^2}} (|K_2\rangle + \epsilon |K_1\rangle) \\ &= \frac{1}{\sqrt{2(1+|\epsilon|^2)}} [(1+\epsilon)|K^0\rangle - (1-\epsilon)|\bar{K}^0\rangle], \end{aligned} \tag{1.5}$$

$$\begin{aligned}
|K_S > &= \frac{1}{\sqrt{1+|\epsilon|^2}} (|K_1 > + \epsilon |K_2 >) \\
&= \frac{1}{\sqrt{2(1+|\epsilon|^2)}} [(1+\epsilon) |K^0 > + (1-\epsilon) |\bar{K}^0 >],
\end{aligned}$$

where ϵ parametrizes the amount of CP asymmetry, or mixing of CP states. CP violation from this mixing of states is referred to as “indirect CP violation”. Therefore, ϵ is a measure of the amount of indirect CP violation and is of the order $\sim 10^{-3}$.

Efforts have been made to measure the amount of “direct CP violation” in Nature. For example, if the $|K_2 >$ state in K_L were to directly decay to a CP-even state this would indicate direct CP violation; this could also occur in the $|K_S >$ if the the $|K_1 >$ state were to directly decay to a CP-odd state. The amount of direct CP violation is parametrized by ϵ'/ϵ . It can be shown that

$$\frac{\Gamma(K_L \rightarrow \pi^+ \pi^-) / \Gamma(K_S \rightarrow \pi^+ \pi^-)}{\Gamma(K_L \rightarrow \pi^0 \pi^0) / \Gamma(K_S \rightarrow \pi^0 \pi^0)} = \frac{|\eta_{+-}|^2}{|\eta_{00}|^2} \approx 1 + 6Re(\epsilon'/\epsilon)$$

where Γ is the decay rate for the corresponding double pion decay and η is the ratio of the CP violating to CP conserving decay amplitudes in the corresponding decay mode. There has been a series of experiments designed to measure this double ratio precisely in order to extract ϵ'/ϵ . The current world average is $(2.1 \pm 0.5) \times 10^{-3}$ [10].

1.3 An Introduction to the $K_L \rightarrow \gamma^{(*)} \gamma^{(*)}$ Family of Decays

The family of $K_L \rightarrow \gamma^{(*)} \gamma^{(*)}$ decays may be the most interesting among all the radiative decays of the long-lived neutral kaon ¹. The rare decays $K_L \rightarrow \gamma\gamma$, $K_L \rightarrow e^+ e^- \gamma$, $K_L \rightarrow \mu^+ \mu^- \gamma$, $K_L \rightarrow e^+ e^- \mu^+ \mu^-$, $K_L \rightarrow e^+ e^- e^+ e^-$, and $K_L \rightarrow \mu^+ \mu^- \mu^+ \mu^-$ share an underlying two photon (real or virtual) vertex, $K_L \rightarrow \gamma^{(*)} \gamma^{(*)}$. For example, the rare decay $K_L \rightarrow e^+ e^- e^+ e^-$ proceeds via a two virtual photon intermediate state, $K_L \rightarrow \gamma^* \gamma^*$, with internal photon conversions to two $e^+ e^-$ pairs (see figure 1.1), whereas the related decay $K_L \rightarrow e^+ e^- \gamma$ arises from one internal conversion, $K_L \rightarrow \gamma^* \gamma$. The study of this family of rare decays is interesting in its own right. In addition, it is needed to extract interesting physics parameters that contribute to other rare K_L decays.

¹The * represents a virtual (off mass-shell) photon.

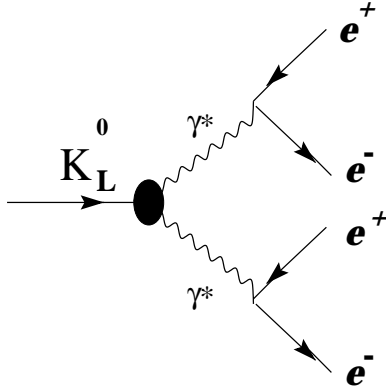


Figure 1.1: Diagram of $K_L \rightarrow \gamma^* \gamma^* \rightarrow e^+ e^- e^+ e^-$.

The $K_L \rightarrow \gamma^{(*)} \gamma^{(*)}$ transition involves *long-distance* and *short-distance* processes. Electroweak interactions of quark and gluon fields in the Standard Model contribute to short-distance physics and are directly calculable (see figure 1.2(a)). Long-distance processes involve low energy non-perturbative strong-interactions with hadronic effects (see figure 1.2(b)). These processes are difficult to calculate and are poorly understood. We need to understand long-distance effects to be able to further examine the physics of the short-distance processes.

An experimental measurement of the $K_L \gamma^* \gamma^*$ form factor is essential to understand long distance contributions to other rare K_L decays, in particular $K_L \rightarrow \mu^+ \mu^-$ [11, 12, 13, 14, 15]. The $K_L \rightarrow \mu^+ \mu^-$ branching ratio can be written as

$$B(K_L \rightarrow \mu^+ \mu^-) = |ReA|^2 + |ImA|^2, \quad (1.6)$$

where A is the decay amplitude for $K_L \rightarrow \mu^+ \mu^-$. The absorptive term, $|ImA|^2$, represents long-distance contributions with real photons (unitarity limit). The dispersive term, $|ReA|^2$, includes both short-distance and long-distance contributions. The short-distance process is sensitive to the CKM matrix element V_{td} and the long-distance process includes the $K_L \gamma^* \gamma^*$ vertex. Figures 1.3 and 1.4 illustrate the short-distance and long-distance contributions to $K_L \rightarrow \mu^+ \mu^-$. There are several models that parametrize the $K_L \gamma^* \gamma^*$ form factor and are discussed in section 1.6. This form factor has never been experimentally measured. Therefore, experimental input is essential to determine this form factor in order to extract V_{td} . So far, the alternative has been to use the

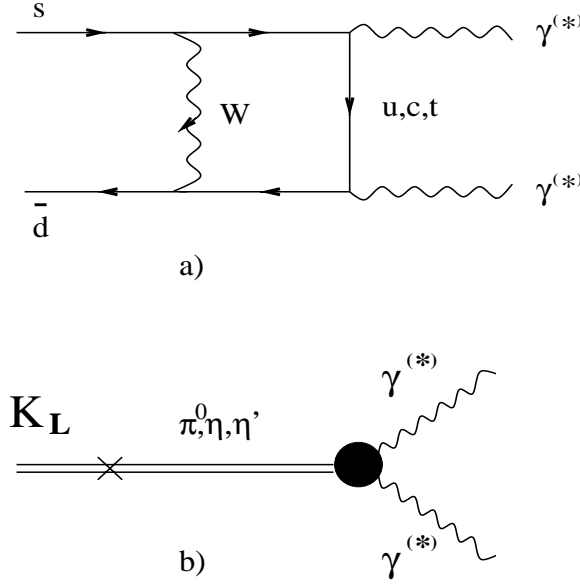


Figure 1.2: The Feynman diagrams for $K_L \rightarrow \gamma^{(*)}\gamma^{(*)}$. (a) Short-distance contribution. (b) Long-distance pole contribution.

$K_L \rightarrow \gamma\gamma^*$ modes, such as $K_L \rightarrow e^+e^-\gamma$ and $K_L \rightarrow \mu^+\mu^-\gamma$ which occur at higher rates than four-lepton final state modes, to measure the corresponding form factor. In this thesis, we do not attempt to extract V_{td} with the $K_L\gamma^*\gamma^*$ form factor measurement using $K_L \rightarrow e^+e^-e^+e^-$. Another related decay mode which may have a higher sensitivity to the $K_L\gamma^*\gamma^*$ form factor and thus to V_{td} is $K_L \rightarrow e^+e^-\mu^+\mu^-$ [16, 17, 18, 19]. Unfortunately, $K_L \rightarrow e^+e^-\mu^+\mu^-$ is highly suppressed, with a branching ratio of $\sim 10^{-9}$. Additionally, the branching ratio for the decay mode $K^+ \rightarrow \pi^+\nu\bar{\nu}$ is very sensitive to V_{td} , however it is of the order $\sim 10^{-10}$ [20, 21, 22]. With the construction of future high-precision kaon experiments perhaps we will one day measure V_{td} .

In this thesis, we study the decay mode $K_L \rightarrow e^+e^-e^+e^-$ and measure the $K_L\gamma^*\gamma^*$ form factor for the first time. In addition, we measure its branching fraction and search for CP violation in the $K_L\gamma^*\gamma^*$ transition. Discovering CP violation in $K_L \rightarrow e^+e^-e^+e^-$ would be interesting since it would be a first in a purely leptonic decay mode. The results presented in this thesis are independently published elsewhere [23].

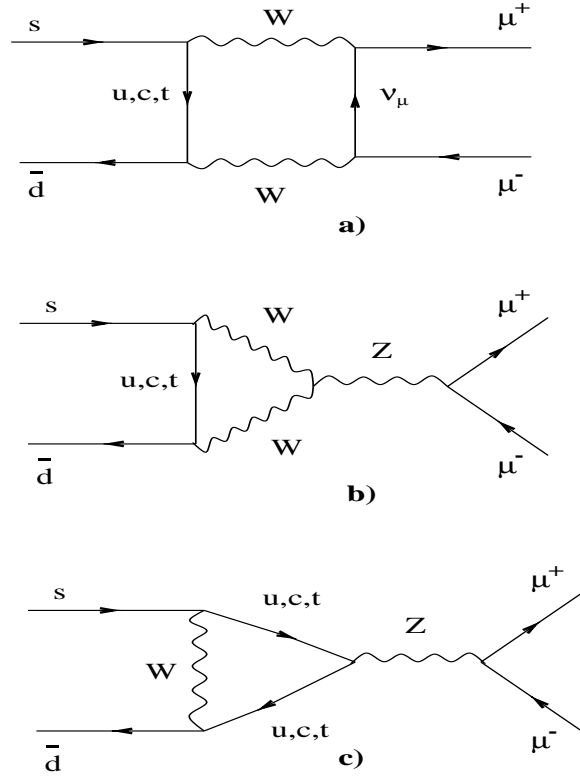


Figure 1.3: Short-Distance Feynman diagrams of $K_L \rightarrow \mu^+ \mu^-$. (a) Leading order box diagram. (b) and (c) Penguin diagrams.

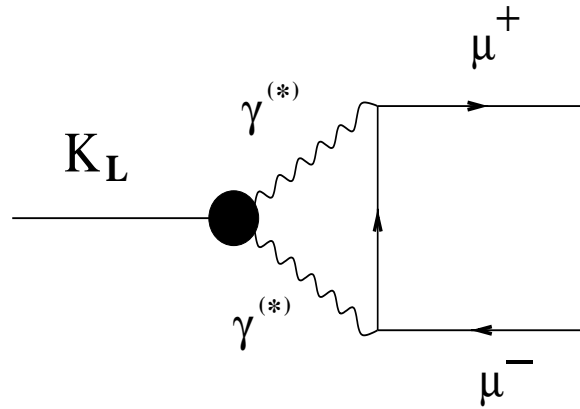


Figure 1.4: Long-Distance Feynman diagram of $K_L \rightarrow \mu^+ \mu^-$.

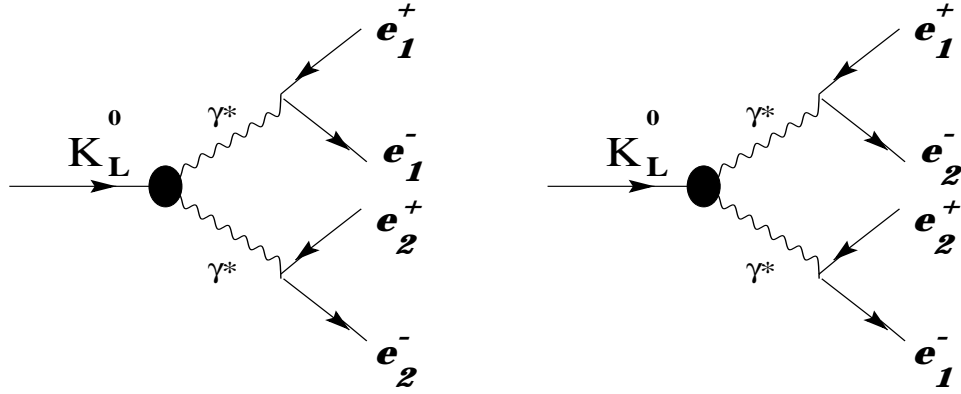


Figure 1.5: The Feynman diagrams for $K_L \rightarrow e^+e^-e^+e^-$.

1.4 Branching Ratio of $K_L \rightarrow e^+e^-e^+e^-$

1.4.1 QED Calculation

In $K_L \rightarrow e^+e^-e^+e^-$ there are two pairs of identical particles in the final state. There are two Feynman diagrams for this decay (shown in figure 1.5) plus the interference between the two since we have particles of the same species. The QED calculation of the decay rate has been carried out by Miyazaki and Takasugi neglecting CP violation (which is a small effect), radiative corrections and the existence of a form factor [24]. Therefore, in this approximation K_L is the odd CP eigenstate ($CP = -1$) K_2 . The five independent variables chosen to parametrize the matrix element are:

$$x_1^2 = (p_1^+ + p_1^-)^2, \quad (1.7)$$

$$x_2^2 = (p_2^+ + p_2^-)^2, \quad (1.8)$$

$$y_1^2 = |\vec{p}_1^+ - \vec{p}_1^-|^2 / (E_1^+ + E_1^-)^2, \quad (1.9)$$

$$y_2^2 = |\vec{p}_2^+ - \vec{p}_2^-|^2 / (E_2^+ + E_2^-)^2, \quad (1.10)$$

$$\cos(\phi) = (\vec{p}_1^+ \times \vec{p}_1^-) \cdot (\vec{p}_2^+ \times \vec{p}_2^-) / |\vec{p}_1^+ \times \vec{p}_1^-| \cdot |\vec{p}_2^+ \times \vec{p}_2^-|, \quad (1.11)$$

where $p_{1,2}^\pm$ and $E_{1,2}^\pm$ are the four momenta and the energies of the two e^\pm , respectively. The labels 1,2 correspond to the two intermediate virtual photons in either of the diagrams in figure 1.5. In addition, $x_{1,2}$ are the invariant masses of the e^+e^- pairs (or

of the virtual photons), $y_{1,2}$ are measures of the energy partition and ϕ is the angle between the planes of the two e^+e^- pairs.

The matrix element for the first diagram is

$$\mathcal{M}_1 = \frac{2f}{M} \epsilon_{\mu\nu\rho\sigma} \frac{(p_1^+ + p_1^-)^\nu (p_2^+ + p_2^-)^\sigma}{(p_1^+ + p_1^-)^2 (p_2^+ + p_2^-)^2} \bar{u}(p_1^-) \gamma^\mu v(p_1^+) \bar{u}(p_2^-) \gamma^\rho v(p_2^+) \quad (1.12)$$

where f is the momentum dependent form factor, M is the kaon invariant mass, $\epsilon_{\mu\nu\rho\sigma}$ is the antisymmetric tensor, u and v are four-component column-spinors and \bar{u} and \bar{v} are four-component row-spinors that represent the momentum-space wave functions of the final state particles and the γ 's are the Dirac matrices. A similar expression can be written for the matrix element for the cross diagram.

The ratio of decay rates, ρ , is written as

$$\begin{aligned} \rho = \Gamma(K_2 \rightarrow \gamma\gamma) / \Gamma(K_2 \rightarrow e^+e^-e^+e^-) &= \int |\mathcal{M}|^2 dx_1 dx_2 dy_1 dy_2 d\phi \\ &= \int |\mathcal{M}_1 + \mathcal{M}_2|^2 dx_1 dx_2 dy_1 dy_2 d\phi \\ &= \int (|\mathcal{M}_1|^2 + |\mathcal{M}_2|^2 + \mathcal{M}_1 \mathcal{M}_2^* + \mathcal{M}_1^* \mathcal{M}_2) dx_1 dx_2 dy_1 dy_2 d\phi \\ &= \Gamma_1 + \Gamma_2 + \Gamma_{12}, \end{aligned} \quad (1.13)$$

where Γ is the total decay rate and \mathcal{M} is the total matrix element for $K_2 \rightarrow e^+e^-e^+e^-$. The contributions of the diagrams, including interference, are labeled by 1 and 2. Since the two diagrams are symmetric, we have $\Gamma_1 = \Gamma_2$ with

$$\begin{aligned} \Gamma_1 / \Gamma(K_2 \rightarrow \gamma\gamma) &= \frac{1}{2\pi} \left(\frac{\alpha}{4\pi} \right)^2 \int_{2m}^{M-2m} dx_1 \int_{2m}^{M-x_1} dx_2 \int_{-\eta_1}^{\eta_1} dy_1 \int_{-\eta_2}^{\eta_2} dy_2 \int_0^{2\pi} d\phi \\ &\quad \left| \frac{f(x_1^2, x_2^2)}{f(0,0)} \right| \left[1 - \frac{2(x_1^2 + x_2^2)}{M^2} + \frac{(x_1^2 - x_2^2)^2}{M^4} \right]^{3/2} \\ &\quad \left\{ \left[\frac{1}{x_1 x_2} + \left(\frac{y_1^2}{x_1} + \frac{4m^2}{x_1^3} \right) \left(\frac{y_2^2}{x_2} + \frac{4m^2}{x_2^3} \right) \right] \sin^2 \phi \right. \\ &\quad \left. + \left[\frac{y_1^2 + y_2^2}{x_1 x_2} + \frac{4m^2(x_1^2 + x_2^2)}{x_1^3 x_2^3} \right] \cos^2 \phi \right\}, \end{aligned} \quad (1.14)$$

where m is the electron invariant mass and $\eta_{1,2} = [1 - (2m/x_{1,2})^2]^{1/2}$. The interference term, Γ_{12} , is long and complicated and can be found in [24]. If the interference term is

neglected ρ reduces to the model of Kroll and Wada [25] where the process is regarded as nearly independent double internal photon conversions.

The QED prediction of Miyazaki and Takasugi [24], including the interference term, gives

$$\frac{\Gamma(K_2 \rightarrow e^+e^-e^+e^-)}{\Gamma(K_2 \rightarrow \gamma\gamma)} = 6.22 \times 10^{-5}. \quad (1.15)$$

This calculation neglects CP violation, radiative corrections and the existence of a form factor, which are not large effects.

1.4.2 Other Predictions

The QED calculation of Miyazaki and Takasugi described above will also be referred to as the Phase Space model since the decay rate is determined only by the phase space and a momentum dependent form factor is neglected. However, since $K_L \rightarrow e^+e^-e^+e^-$ is dominated by long distance interactions which characterize the physics at the $K_L\gamma^*\gamma^*$ vertex, the Phase Space model alone is not enough to describe how kaons decay to two lepton pairs. In addition to the form factor being neglected in this model, CP violation is also ignored since it is a small effect.

The model of Uy [26, 27] is an extension of the Phase Space model and considers both the long-lived and short-lived kaon decays $K_L \rightarrow \gamma^*\gamma^*$ and $K_S \rightarrow \gamma^*\gamma^*$. In this case, CP violation due to mixing is included and both CP-violating and CP-conserving form factors are determined for $K_L \rightarrow \gamma^*\gamma^*$ and $K_S \rightarrow \gamma^*\gamma^*$. Measurements of $\frac{d\Gamma_{K_L}}{d\phi}$ and $\frac{d\Gamma_{K_S}}{d\phi}$, the angular decay distributions of K_L and K_S decaying to two lepton pairs (where ϕ is the angle between the planes of the two lepton pairs), can be used to determine these form factors. However, these calculations are performed only for the decay to lepton pairs of different species, $K_L \rightarrow e^+e^-\mu^+\mu^-$. The calculations involving $K_L \rightarrow e^+e^-e^+e^-$ and $K_L \rightarrow \mu^+\mu^-\mu^+\mu^-$ are difficult due to the exchange pairing of the leptons. Hopefully, these calculations will be carried out in the near future.

In addition to the Phase Space model, the $K_L \rightarrow e^+e^-e^+e^-$ decay rate has been calculated using the Vector Meson Dominance model (VMD) of electromagnetic couplings by Quigg and Jackson [28]. In this model it is assumed that there are no direct

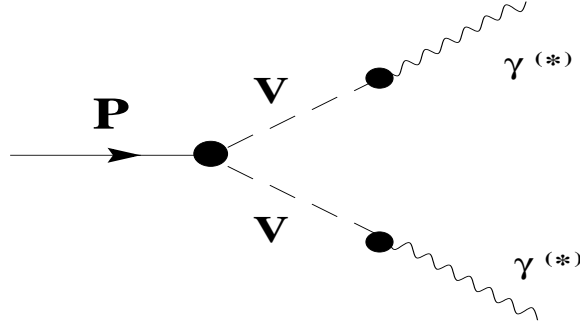


Figure 1.6: The Vector Meson Dominance Model (VMD) diagram for a pseudoscalar meson (P) decaying to $\gamma^*\gamma^*$ (or $\gamma\gamma$) via intermediate vector mesons.

$P\gamma^{(*)}\gamma^{(*)}$ or $PV\gamma^{(*)}$ couplings². Instead, all photon couplings come from intermediate vector mesons, as in figure 1.6. The form factor in the VMD model for the $P \rightarrow \gamma^*\gamma^*$ transitions (as in $K_L \rightarrow \gamma^*\gamma^* \rightarrow e^+e^-e^+e^-$) is proportional to

$$\frac{1}{(m_1^2 + q_1^2)(m_2^2 + q_2^2)} \quad (1.16)$$

where $q_{1,2}$ are the virtual photon invariant masses ($M_{e^+e^-}$ in this case) and $m_{1,2}$ are the vector meson invariant masses. In [28] the ω resonance invariant mass is used for $m_{1,2}$ to obtain

$$\frac{, (K_2 \rightarrow e^+e^-e^+e^-)}{, (K_2 \rightarrow \gamma\gamma)} = 6.3 \times 10^{-5}. \quad (1.17)$$

Just as in the Phase Space model, CP violation and radiative corrections have been neglected. In addition, VMD neglects the interference term. For comparison, the Phase Space model prediction without the interference term is [24]

$$\frac{, (K_2 \rightarrow e^+e^-e^+e^-)}{, (K_2 \rightarrow \gamma\gamma)} = 6.26 \times 10^{-5}, \quad (1.18)$$

which is not very different from the VMD model prediction.

Long-distance contributions, or non-perturbative effects among mesons, dominate the decay $K_L \rightarrow e^+e^-e^+e^-$. However, as discussed in section 1.3, these effects are

²Here, P is a pseudoscalar meson (such as the kaon) and V is a vector meson (such as the ρ meson).

not currently calculable. Fortunately, there are other phenomenological models that attempt to study long-distance effects, such as chiral perturbation theory (χPT). This theory uses an effective lagrangian that obeys chiral symmetry, an approximate symmetry of the QCD lagrangian. The general method is to work to an order p^n in the (low) energy expansion (or extension) of the basic lagrangian (order p^2). The order corresponds to the number of derivatives and external fields that occur in the operators in the lagrangian. For example, the expansion of the basic lagrangian of order p^2 , \mathcal{L}_2 , may include a lagrangian with all contributions of order p^4 , \mathcal{L}_4 , to obtain the effective lagrangian, \mathcal{L}_{eff} . Recently, Zhang and Goity have made advances in calculating the decay rate of $K_L \rightarrow e^+e^-e^+e^-$ using chiral perturbation theory [29]. These predictions include all contributions to order p^6 in χPT and are:

$$\begin{aligned} \frac{\Gamma(K_2 \rightarrow e^+e^-e^+e^-)}{\Gamma(K_2 \rightarrow \gamma\gamma)} &= 6.26 \times 10^{-5} \text{ (no form factor)} \\ \frac{\Gamma(K_2 \rightarrow e^+e^-e^+e^-)}{\Gamma(K_2 \rightarrow \gamma\gamma)} &= 6.50 \times 10^{-5} \text{ (with form factor, scenario 1)} \\ \frac{\Gamma(K_2 \rightarrow e^+e^-e^+e^-)}{\Gamma(K_2 \rightarrow \gamma\gamma)} &= 6.48 \times 10^{-5} \text{ (with form factor, scenario 2)}. \end{aligned} \tag{1.19}$$

The two scenarios result from different coefficients in the form factors which were obtained by fitting the data in [30, 31, 32]. Again, CP violation and radiative corrections have been neglected but the interference term is included.

A summary of the current predictions for the ratio of decay rates $\frac{\Gamma(K_L \rightarrow e^+e^-e^+e^-)}{\Gamma(K_L \rightarrow \gamma\gamma)}$ is displayed in table 1.1. For convenience, the predictions for the branching ratio or fraction $B(K_L \rightarrow e^+e^-e^+e^-) = \frac{\Gamma(K_L \rightarrow e^+e^-e^+e^-)}{\Gamma_{\text{total}}(K_L \rightarrow \text{anything})}$ are summarized in table 1.2, using the current measurement of the $B(K_L \rightarrow \gamma\gamma)$ [10] which is the source of the uncertainties in this table.

We see that the differences between Phase Space, VMD and χPT without any form factor are small. Currently, the branching ratio of $K_L \rightarrow e^+e^-e^+e^-$ is measured to $\pm 0.8 \times 10^{-8}$ [10]. To test if Nature prefers one of these models, a more precise measurement of the branching ratio is necessary. For example, in order to distinguish between Phase Space and χPT with a form factor, we need a branching ratio measurement that is at least five times more sensitive than the current world average.

Table 1.1: Predictions for the ratio of decay rates $\frac{\Gamma(K_L \rightarrow e^+e^-e^+e^-)}{\Gamma(K_L \rightarrow \gamma\gamma)}$. All models neglect CP violation and radiative effects. The Phase Space model also neglects the form factor. The VMD model ignores the interference term.

QED (Phase Space) [24]	VMD [28]	χ PT [29]
6.22×10^{-5} (no FF)	6.3×10^{-5} (no interf.)	6.26×10^{-5} (no FF) 6.50×10^{-5} (with FF) 6.48×10^{-5} (with FF)

Table 1.2: Predictions for $B(K_L \rightarrow e^+e^-e^+e^-) = \frac{\Gamma(K_L \rightarrow e^+e^-e^+e^-)}{\Gamma_{\text{total}}(K_L \rightarrow \text{anything})}$. Each element in this table has an uncertainty of 2.6% due to the uncertainty in the current measurement of the $B(K_L \rightarrow \gamma\gamma)$ [10]. All models neglect CP violation and radiative effects. The Phase Space model also neglects the form factor. The VMD model ignores the interference term.

QED (Phase Space) [24]	VMD [28]	χ PT [29]
3.64×10^{-8} (no FF)	3.7×10^{-8} (no interf.)	3.67×10^{-8} (no FF) 3.81×10^{-8} (with FF) 3.80×10^{-8} (with FF)

Currently, all models for $K_L \rightarrow e^+e^-e^+e^-$ neglect radiative effects. Radiative effects introduce complications in any process that has charged particles in the final state. This is particularly true for $K_L \rightarrow e^+e^-e^+e^-$, in which all four final state particles can radiate photons, which could have a significant effect on the tree-level process. However, an exact QED calculation of the radiative corrections does not exist for this decay mode. For the purposes of our measurement, we implement approximate corrections as described later in chapter 5.

1.4.3 Previous Measurements

The first direct observation of $K_L \rightarrow e^+e^-e^+e^-$ was in the CERN experiment NA31 [33, 34] with two candidate events. The branching ratio was measured to be $(4 \pm 3) \times 10^{-8}$. The same experiment later found 6 more events giving a total of 8 events with a branching ratio of $(10.4 \pm 3.7_{\text{stat}} \pm 1.1_{\text{sys}}) \times 10^{-8}$ [33, 34].

The Brookhaven experiment B845 also observed 6 events and measured the branching ratio to be $(3.07 \pm 1.25_{stat} \pm 0.26_{syst}) \times 10^{-8}$ [35]. The KEK experiment has also observed 18 events ($M_{e^+e^-} > 470 \text{ MeV}/c^2$) with a branching ratio of $(6 \pm 2_{stat} \pm 1_{syst}) \times 10^{-8}$ and 6 events ($M_{e^+e^-} > 480 \text{ MeV}/c^2$) with a branching ratio of $(7 \pm 3_{stat} \pm 2_{syst}) \times 10^{-8}$ [36, 37].

The previous most significant measurement of $K_L \rightarrow e^+e^-e^+e^-$ came from the KTeV predecessor experiment E799-I with 27 events observed [38, 19]. The branching ratio was measured to be $(3.96 \pm 0.78 \pm 0.32) \times 10^{-8}$. In this thesis, we present an improved measurement of the $K_L \rightarrow e^+e^-e^+e^-$ branching ratio.

The PDG world average of these results is [10]

$$\frac{\Gamma(K_L \rightarrow e^+e^-e^+e^-)}{\Gamma_{\text{total}}(K_L \rightarrow \text{anything})} = (4.1 \pm 0.8) \times 10^{-8}. \quad (1.20)$$

1.5 CP Studies with $K_L \rightarrow e^+e^-e^+e^-$

1.5.1 How to Study CP Symmetry in $K_L \rightarrow e^+e^-e^+e^-$

Historically, the decay $\pi^0 \rightarrow e^+e^-e^+e^-$ was used to find the intrinsic parity of the neutral pion. Over 40 years ago, in 1959, Plano *et al.* experimentally determined the π^0 to have negative parity [39, 40]; this, in turn, means that the π^0 is a pseudoscalar meson. It is the relative polarization of the photons in the decay $\pi^0 \rightarrow \gamma\gamma$ that elucidate the pion parity. In the double Dalitz decay of the π^0 each of the photons internally convert to an e^+e^- pair, and the angle between the planes that the e^+e^- pairs form allows one to show that the π^0 is a pseudoscalar meson. A similar test can be conducted for the neutral kaon.

We search for CP violation in $K_L \rightarrow e^+e^-e^+e^-$ by studying ϕ , the angle between the planes of the two e^+e^- pairs. The Kroll-Wada formula gives [25]

$$\frac{d\Gamma(K_{1,2} \rightarrow e^+e^-e^+e^-)}{d\phi} \propto (1 + B \cos(2\phi)), \quad (1.21)$$

where $K_1(K_2)$ is the even(odd) eigenstate of CP and the constant B is +0.20 for K_1 and -0.20 for K_2 .

Introduction of CP violation in mixing results in complications since K_L is not a pure CP eigenstate but a mixture of the two CP eigenstates, K_1 and K_2 , $K_L = (K_2 + \epsilon K_1)/\sqrt{1 + |\epsilon|^2}$. More generally,

$$\frac{d, (K_L \rightarrow e^+ e^- e^+ e^-)}{d\phi} \propto (1 + \beta_{\text{CP}} \cos(2\phi) + \gamma_{\text{CP}} \sin(2\phi)) \quad (1.22)$$

The parameters β_{CP} and γ_{CP} are defined below. The $\sin(2\phi)$ term results from the interference between the CP-odd and CP-even final states.

Assuming CP-violation only due to mixing ϵ , we have ($A_{1,2}$ are the decay amplitudes of $K_{1,2} \rightarrow e^+ e^- e^+ e^-$)

$$\begin{aligned} \frac{d, (K_L \rightarrow e^+ e^- e^+ e^-)}{d\phi} &\propto |\epsilon A_1 + A_2|^2 \\ &= |\epsilon A_1|^2 + |A_2|^2 + 2\text{Re}(\epsilon A_1 A_2^*) \\ &= |\epsilon A_1|^2 + |A_2|^2 + 2\text{Re}(\epsilon r) |A_2|^2 \end{aligned} \quad (1.23)$$

where we define $r = A_1/A_2$, the ratio of the two decay amplitudes and is estimated to be of order unity³ [19]. We assume that the interference term is proportional to $\sin(2\phi)$, as was done for the π^0 decay in [40], $\frac{d\Gamma(K_L \rightarrow e^+ e^- e^+ e^-)}{d\phi}^{\text{Inter}} = 2\text{Re}(\epsilon r) |A_2|^2 \propto 2\text{Re}(\epsilon r) \sin(2\phi)$.

Substituting the Kroll-Wada formula for $|A_{1,2}|^2$ we obtain

$$\begin{aligned} &\frac{d, (K_L \rightarrow e^+ e^- e^+ e^-)}{d\phi} \\ &= |\epsilon|^2 a_1 [1 + b \cos(2\phi)] + a_2 [1 - b \cos(2\phi)] + c [2\text{Re}(\epsilon r) \sin(2\phi)] \\ &= (|\epsilon|^2 a_1 + a_2) \left\{ 1 - \left[\frac{1 - |\epsilon|^2 a_1/a_2}{1 + |\epsilon|^2 a_1/a_2} \right] b \cos(2\phi) + \frac{c}{a_2} \left[\frac{2\text{Re}(\epsilon r)}{(1 + |\epsilon|^2 a_1/a_2)} \sin(2\phi) \right] \right\} \end{aligned} \quad (1.24)$$

where $a_1/a_2 \approx r^2$ (which is approximately unity), $b \equiv |B| = 0.20$ (as in equation 1.21) and $\frac{c}{a_2} \equiv C$ is an unknown constant that depends on the extent and nature of CP violation. There are no theoretical predictions for C.

Finally we have

$$\frac{d, (K_L \rightarrow e^+ e^- e^+ e^-)}{d\phi} \propto \left[1 - \frac{1 - |\epsilon r|^2}{1 + |\epsilon r|^2} B \cos(2\phi) + \frac{2\text{Re}(\epsilon r)}{1 + |\epsilon r|^2} C \sin(2\phi) \right] \quad (1.25)$$

³In reality, the ratio r is a function of phase space.

with

$$\beta_{\text{CP}} = -\frac{1 - |\epsilon r|^2}{1 + |\epsilon r|^2} B \approx B \quad , \quad \gamma_{\text{CP}} = \frac{2\text{Re}(\epsilon r)}{1 + |\epsilon r|^2} C \approx 2\text{Re}(\epsilon r)C, \quad (1.26)$$

which gives us equation 1.22. The cosine term in equation 1.25 above is similar to the Kroll-Wada formula in 1.21. The sine term in equation 1.25 is proportional to the strength of CP violation, as can be seen in 1.26. We determine the values of β_{CP} and γ_{CP} from the distribution of the angle ϕ in the $K_L \rightarrow e^+e^-e^+e^-$ events.

1.5.2 Previous Measurements

The CERN experiment NA31 [33, 34] performed the first CP test in $K_L \rightarrow e^+e^-e^+e^-$. They used a likelihood test and found their data favoring the CP-odd state ($CP = -1$). The test statistic using a likelihood ratio was

$$\frac{L(CP = -1)}{L(CP = +1)} = \prod_{i=1}^N \frac{1 - \alpha_i \cos(2\phi_i)}{1 + \alpha_i \cos(2\phi_i)} \quad (1.27)$$

where N is the total number of observed events, ϕ is the angle between the planes of the two e^+e^- pairs and α is given by [25]

$$\alpha = \frac{y_1^2 + y_2^2 - 1 - y_1^2 y_2^2 + \frac{4m^2}{x_1^2}(1 - y_2^2) + \frac{4m^2}{x_2^2}(1 - y_1^2) - \frac{(4m^2)^2}{x_1^2 x_2^2}}{1 + y_1^2 y_2^2 + y_1^2 + y_2^2 + \frac{4m^2}{x_1^2}(1 + y_2^2) + \frac{4m^2}{x_2^2}(1 + y_1^2) + \frac{(4m^2)^2}{x_1^2 x_2^2}} \quad (1.28)$$

where $x_{1,2}$, $y_{1,2}$ and m are defined in section 1.4.1 above.

The most recent measurement from the KTeV predecessor experiment E799-I [38, 19] fit the ϕ distribution to equation 1.21 to measure β_{CP} only. A CP study, as described above, was also conducted with these events and observed that the data somewhat favored the $CP = -1$ hypothesis. The parameter in front of the $\cos(2\phi)$ term in the Kroll-Wada formula 1.21 was measured for the first time to be $\beta_{\text{CP}} = -0.22 \pm 0.30$, in agreement with the theoretical expectation of 0.20 (which neglects CP violation, radiative corrections and the existence of a form factor) [25]. Using equation 1.26, $|\epsilon r|^2$ was measured to be $-0.036_{-0.39}^{+2.46}$, consistent with zero. Also, assuming only direct CP violation, this equation becomes

$$\beta = -\frac{1 - |\epsilon'_{\gamma^* \gamma^*}|^2}{1 + |\epsilon'_{\gamma^* \gamma^*}|^2} B \quad (1.29)$$

where $\epsilon'_{\gamma^*\gamma^*}$ is the ratio between the CP violating and the CP conserving amplitudes of $K_L \rightarrow e^+e^-e^+e^-$. An upper limit of $|\epsilon'_{\gamma^*\gamma^*}| < 2.2$ was set at the 90% confidence level.

In this thesis, we present an improved measurement of the CP parameter β_{CP} . We also place a limit on the CP parameter γ_{CP} (see equations 1.22 and 1.26) for the first time.

1.6 Form Factor Models

The $K_L \rightarrow e^+e^-e^+e^-$ form factor reveals the internal structure of the long lived neutral kaon and information about the $K_L \rightarrow \gamma^*\gamma^*$ vertex. In this thesis, we measure the $K_L\gamma^*\gamma^*$ form factor for the first time. We present measurements of the form factor parameters α_{Taylor} , α_{K^*} and α_{DIP} (described below) using the form factor sensitive M_{ee} distribution.

The form factor can be parametrized very simply using the linear form (as a first term in the Taylor series):

$$f(x) = 1 + \alpha_{Taylor} \cdot x, \quad (1.30)$$

where $x = M_{ee}^2/M_K^2$. In $K_L \rightarrow e^+e^-e^+e^-$, since there are two internal pair productions of e^+e^- pairs we use the following factorized expression for the form factor:

$$F(x_1, x_2) = f(x_1) \cdot f(x_2), \quad (1.31)$$

where $f(x)$ is given by equation 1.30 and $x_1 = M_{ee1}^2/M_K^2$ and $x_2 = M_{ee2}^2/M_K^2$ (x_1 and x_2 are, on average, $\ll 1$). Finally we have for the $K_L \rightarrow \gamma^*\gamma^*$ form factor

$$f(x_1, x_2) \approx 1 + \alpha_{Taylor}(x_1 + x_2). \quad (1.32)$$

The parametrization of a related decay, $K_L \rightarrow e^+e^-\gamma$, which probes the $K_L \rightarrow \gamma\gamma^*$ form factor can also be used for the $K_L \rightarrow \gamma^*\gamma^*$ form factor. This form factor has been parametrized by Bergström, Massó, and Singer (BMS) and is an extension of the VMD model [1, 13, 14]. The BMS model includes standard VMD long-distance pole contributions as shown in figure 1.2(b) in addition to contributions from a $K^*K\gamma$

coupling with $K^* \rightarrow \rho, \omega, \phi$ transitions as shown in figure 1.7. The BMS model form factor expression is:

$$f(x) = \frac{1}{1 - x(m_K^2/m_\rho^2)} + \frac{C\alpha_{K^*}}{1 - x(m_K^2/m_{K^*}^2)} \left[\frac{4}{3} - \frac{1}{1 - x(m_K^2/m_\rho^2)} - \frac{1}{9(1 - x(m_K^2/m_\omega^2))} - \frac{2}{9(1 - x(m_K^2/m_\phi^2))} \right] \quad (1.33)$$

where M_K , M_ρ , M_{K^*} , M_ω and M_ϕ are the invariant masses of the corresponding mesons. The parameter α_{K^*} describes the relative strength of an intermediate pseudoscalar decay amplitude and a vector meson decay amplitude. The first term in this form factor corresponds to a pseudoscalar-pseudoscalar transition $K_L \rightarrow \pi, \eta, \eta' \rightarrow \gamma\gamma^*$. The second term corresponds to a vector-vector transition with $K_L \rightarrow K^*\gamma$ and $K^* \rightarrow \rho, \omega, \phi \rightarrow \gamma^*$. The constant C is determined using various coupling constants [32, 41, 10]:

$$\begin{aligned} G_{NL} &= 1.1 \times 10^{-5}/m_p^2 \\ f_{K^*K\gamma}^2 &= \frac{96\pi, (K^* \rightarrow K^0\gamma)m_{K^*}^3}{(m_{K^*}^2 - m_K^2)^3} \\ f_\rho^2 &= \frac{4\pi\alpha_{EM}^2 m_\rho}{3, (\rho \rightarrow e^+e^-)} \\ f_{K^*} &= \frac{m_{K^*}}{m_\rho} f_\rho \\ f_{K\gamma\gamma}^2 &= \frac{64\pi, (K_L \rightarrow \gamma\gamma)}{m_K^3} \\ C &= \sqrt{8\pi\alpha_{EM}} G_{NL} f_{K^*K\gamma} \frac{m_\rho^2}{f_{K^*} f_\rho^2 f_{K\gamma\gamma}} = 2.3 \end{aligned} \quad (1.34)$$

where G_{NL} is the coupling strength of the $K^* \rightarrow \rho, \omega, \phi$ transition (and is approximately equal to the Fermi constant), $f_{K^*K\gamma}$ is the coupling of the $K^* \rightarrow K^0\gamma$ transition and $f_{K\gamma\gamma}$ is the coupling of the $K_L \rightarrow \gamma\gamma$ transition. In addition, f_ρ and f_{K^*} are the coupling constants of the respective mesons, m_p is the proton invariant mass and α_{EM} is the fine structure constant.

Finally, substituting the values of the coupling constants and meson invariant masses we have the simplified expression [32, 10]:

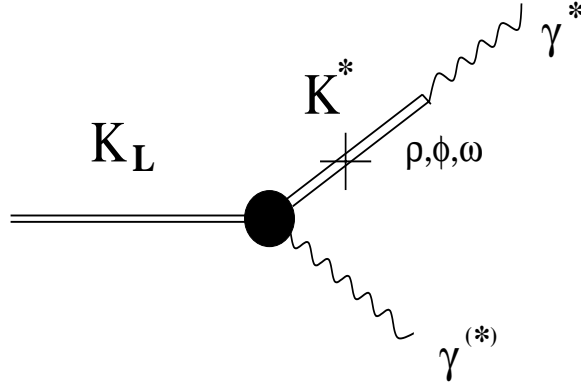


Figure 1.7: Long-distance pole diagram with a vector-vector transition. The diagram shows a $K^* K \gamma$ coupling with a $K^* \rightarrow \rho, \omega, \phi$ transition.

$$f(x) = \frac{1}{1 - 0.418x} + \frac{2.3\alpha_{K^*}}{1 - 0.308x} \left[\frac{4}{3} - \frac{1}{1 - 0.418x} - \frac{1}{9(1 - 0.405x)} - \frac{2}{9(1 - 0.238x)} \right]. \quad (1.35)$$

Again, we use a factorized expression for the $K_L \rightarrow \gamma^* \gamma^*$ form factor as in equation 1.31. The BMS model predicts $|\alpha_{K^*}| = 0.2 - 0.3$. Figure 1.8 shows the form factor as a function of x for different values of α_{K^*} . It is interesting to note that α_{K^*} equal to zero does not correspond to a pointlike form factor ($f(x) = 1$). Instead, $\alpha_{K^*} = 0$ reduces the form factor expression to one similar to the VMD model (see equation 1.16). In addition, since our data exists only for small x , we use a first order Taylor expansion to find that $\alpha_{K^*} \simeq 0.3$ approximates a pointlike form factor. One can easily determine the approximate relation $\alpha_{Taylor} \approx 0.42 - 1.2\alpha_{K^*}$. The parameter α_{K^*} has been recently measured to be $-0.36 \pm 0.06_{stat} \pm 0.02_{syst}$ [42] for $K_L \rightarrow e^+ e^- \gamma$. The PDG world average for α_{K^*} is currently -0.33 ± 0.05 , for $K_L \rightarrow e^+ e^- \gamma$. Other recent measurements of α_{K^*} come from the decays $K_L \rightarrow e^+ e^- \gamma \gamma$, $0.01 \pm 0.12_{stat} \pm 0.03_{syst}$ [43], and $K_L \rightarrow \mu^+ \mu^- \gamma$, $-0.163^{+0.026}_{-0.027}$ [41].

There also exists the form factor parametrization of D'Ambrosio, Isidori and Portolés (DIP) [15] which is relatively model independent. The form factor expression from this

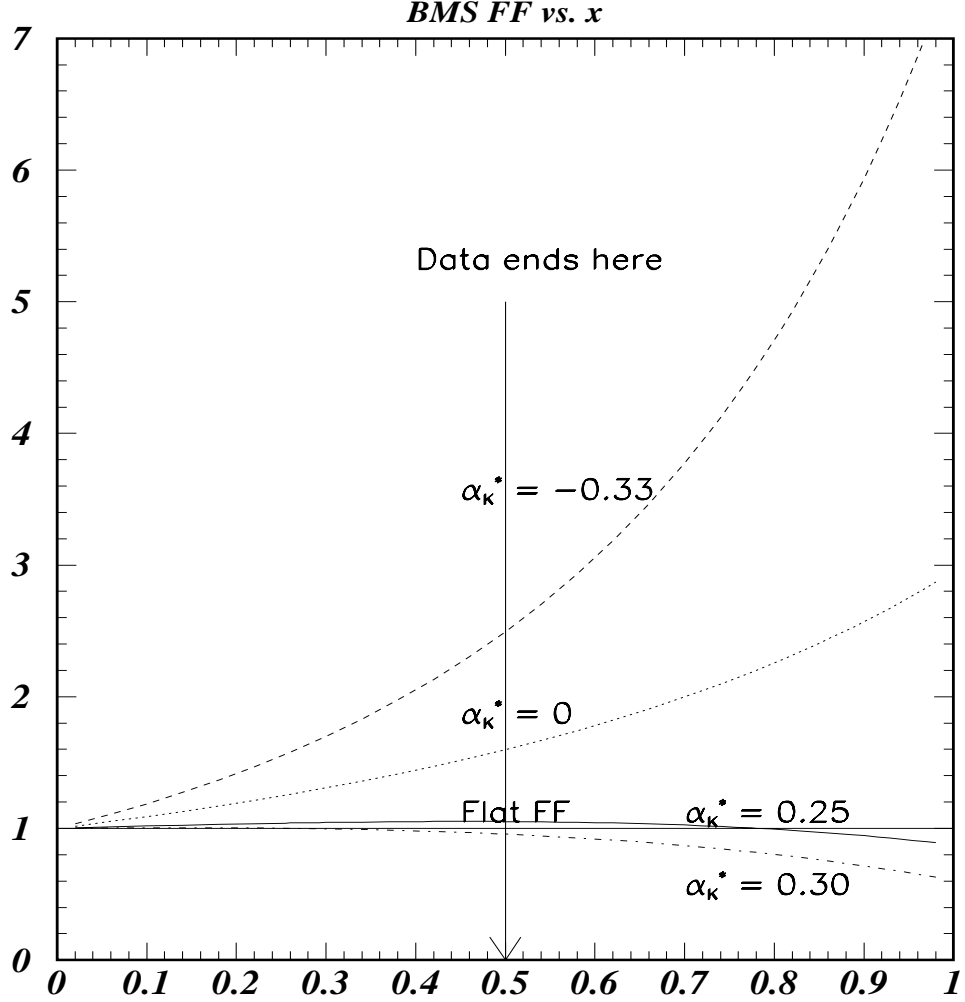


Figure 1.8: The form factor as a function of x for different values of α_{K^*} . Note that α_{K^*} equal to zero is not a pointlike form factor ($f(x) = 1$). Also note that $\alpha_{K^*} \simeq 0.3$ approximates a pointlike form factor, by a first order Taylor expansion, in the region where our data exists. Also, $\alpha_{K^*} \simeq 0.25$ is found empirically to approximate a pointlike form factor. (Pointlike form factor is the straight line.)

model is:

$$\begin{aligned}
 f(q_1^2, q_2^2) &= 1 + \alpha_{DIP} \left[\frac{q_1^2}{q_1^2 - m_\rho^2} + \frac{q_2^2}{q_2^2 - m_\rho^2} \right] + \beta_{DIP} \frac{q_1^2 q_2^2}{(q_1^2 - m_\rho^2)(q_2^2 - m_\rho^2)} \\
 &= 1 + \alpha_{DIP} \left[\frac{x_1}{x_1 - 2.4} + \frac{x_2}{x_2 - 2.4} \right] + \beta_{DIP} \frac{x_1 x_2}{(x_1 - 2.4)(x_2 - 2.4)}. \quad (1.36)
 \end{aligned}$$

where $q = M_{ee}$, m_ρ is the ρ invariant mass [10] and α_{DIP} , β_{DIP} are arbitrary real parameters. Using a factorization model [15], the expectations for α_{DIP} and β_{DIP} are -1.22 and 1.43, respectively, for a ρ form factor. In $K_L \rightarrow e^+ e^- e^+ e^-$, only the first order term (α_{DIP}) is relevant. Due to the dominance of low M_{ee} , this decay mode is not as sensitive to the second order term (β_{DIP}) as would be the decay $K_L \rightarrow e^+ e^- \mu^+ \mu^-$. Neglecting the second order term we get the relation $\alpha_{DIP} = -1 + 2.8 \alpha_{K^*}$, where α_{K^*} is the BMS parameter described above, by Taylor expansion of equation 1.36. In addition, $\alpha_{Taylor} \approx -\alpha_{DIP}/2.4$. Also note that when $\alpha_{DIP} = 0$ (and $\beta_{DIP} = 0$), the DIP parametrization reduces to a flat or pointlike form factor. For reference, α_{DIP} obtained from $K_L \rightarrow \mu^+ \mu^- \gamma$ is -1.55 ± 0.09 [41], the first measurement of this parameter.

1.7 Thesis Overview

We have discussed the importance of studying the decay mode $K_L \rightarrow e^+ e^- e^+ e^-$. This thesis contains several measurements using one of the rarest decay channels of the long-lived neutral kaon. We study the $K_L \rightarrow e^+ e^- e^+ e^-$ and measure its decay rate more precisely than ever before. We also place limits on CP violation in this decay and do this by fitting ϕ distribution to equation 1.22 to extract the CP parameters β_{CP} and γ_{CP} . This thesis contains the first limit on the parameter γ_{CP} . In addition, we measure the $K_L \gamma^* \gamma^*$ form factor for the first time. We measure the parameters of various form factor models (α_{K^*} , α_{DIP} and α_{Taylor}) using the M_{ee} distribution, the distribution that is most sensitive to the form factor.

In chapter 2, we describe the experimental setup, the neutral kaon beam and the specifics of the detector elements. We then continue by describing the event selection and reconstruction in chapters 3 and 4. In chapter 5, the details of the Monte Carlo simulation of the detector are described. In chapters 6 and 7, the candidate signal and

normalization mode event selections are described. The form factor analysis specifics are in chapter 8. The details of the branching ratio analysis are in chapter 9. The CP analysis using the angular distribution is in chapter 10. Finally we conclude with a summary and short discussion of all the results in chapter 11.

Chapter 2

The KTeV Experiment

The KTeV (Kaons at the Tevatron) detector dealt with two kinds of fixed-target kaon experiments. One type of experiment was a high precision experiment designed to search for direct CP violation by measuring the ratio of parameters $\frac{\epsilon'}{\epsilon}$ (E832). Here ϵ' is the parameter for direct CP violation and ϵ is the parameter for indirect CP violation (or CP violation from K^0 and \bar{K}^0 mixing). The other kind of kaon experiment dealt with high-sensitivity rare kaon decays (E799-II). This thesis is based on data collected from the latter experiment.

The KTeV experiment ran in the NM (Neutrino Muon) beamline at Fermilab. A schematic of the fixed-target area at Fermilab is shown in figure 2.1 [44], where one can see the location of the KTeV detector hall.

The E799-II data were collected during two periods in 1997. The first period began in January and ended in March and is referred to as the “winter” run in this thesis. The second period began in August and ended in September and is referred to as the “summer” run in this thesis.

In this chapter, I describe the beamline and detector during E799-II conditions of KTeV running. Additional information can be found in [41, 43, 44, 45, 46, 47, 48, 49].

2.1 The KTeV Beam

The E799-II experiment required two pure, high intensity beams of neutral kaons. These beams were produced by a primary proton beam striking a BeO target. This section describes the details of the beam production.

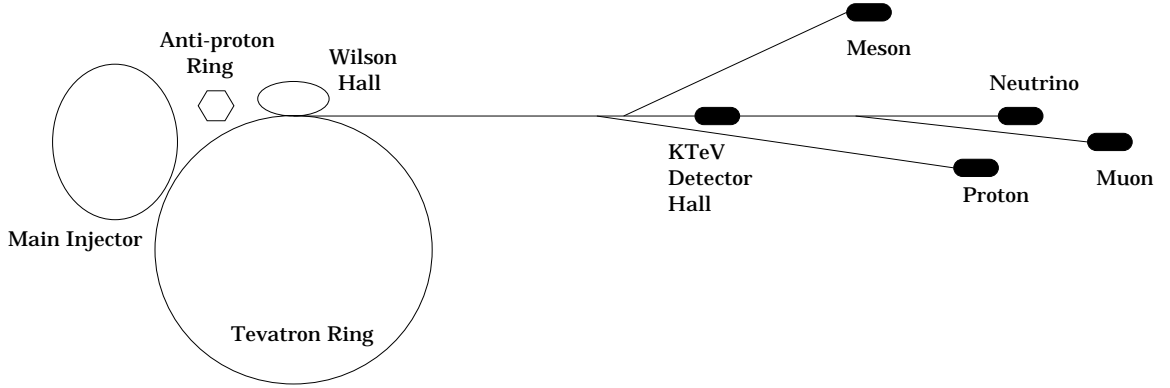


Figure 2.1: Fermilab fixed-target area schematic. The KTeV experiment ran in the NM (Neutrino Muon) beamline.

2.1.1 Primary Proton Beam

The Fermilab Tevatron provided 800 GeV/c protons to the fixed-target areas. During each one minute cycle, there was a “spill” period of 20 seconds throughout which the protons arrived followed by 40 seconds of no protons. Within each spill, there was a 53 MHz radio frequency (RF) structure due to the accelerator. The protons arrived in 1-2 ns wide “buckets” every 19 ns.

This primary beam of protons was incident on a BeO target. The center of the target defined the origin of the KTeV coordinate system. The direction along the beam (or “north”) is defined as the positive Z-axis, with the X-axis horizontal and transverse to the beam (+X is “west”) and the Y-axis is the vertical. The target was 30 cm long (or 1.1 interaction lengths) and the cross-section of the target was $3.0 \text{ mm} \times 3.0 \text{ mm}$. The primary proton beam was nearly horizontal; the targeting angle was chosen to be 4.8 mrad in the vertical plane (aimed downward) to reduce the neutron flux (which peaks at 0 mrad) and to maintain a high neutral kaon flux. The size of the beam at the target was typically $250 \mu\text{m}$ in the horizontal and vertical. During the “winter” running conditions the target received about 5×10^{12} protons per spill and about 3.5×10^{12} protons per spill during “summer” running conditions. The target was located in the NM2 beamline enclosure (a.k.a. KTeV Target Hall) and is shown in figure 2.2.

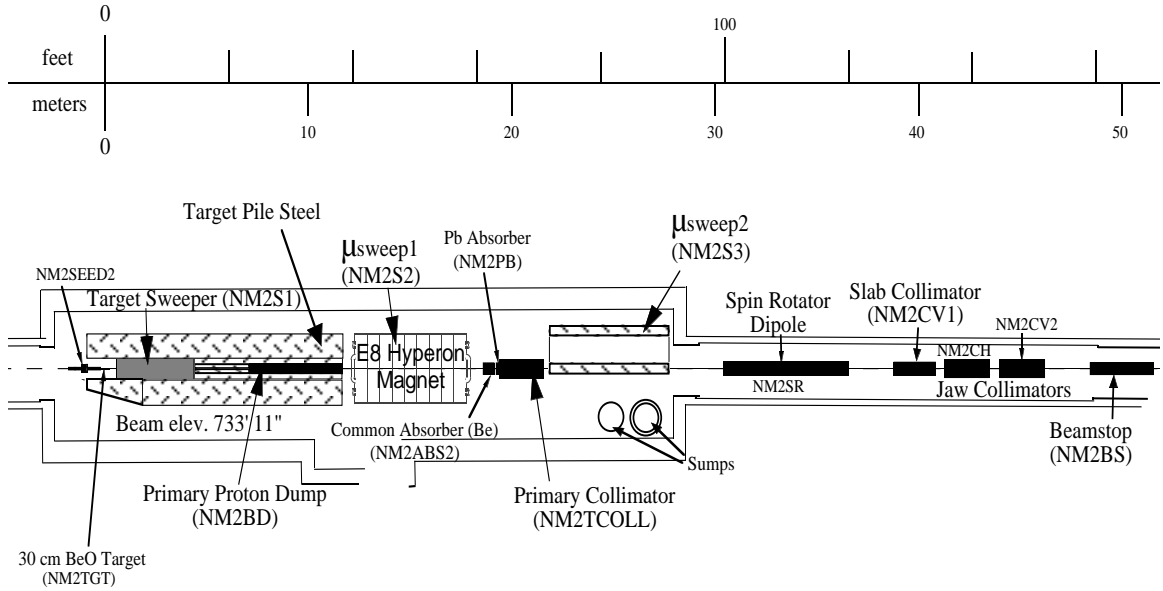


Figure 2.2: Schematic plan view of the KTeV beam elements in the KTeV Target Hall (NM2 enclosure).

2.1.2 Secondary K_L Beams

Two neutral K_L beams were used in E799-II [50]. The two beams were necessary when running under E832 conditions in order to precisely measure direct CP violation in the ratio of parameters $\frac{\epsilon'}{\epsilon}$ [51, 48]. Having two beams was not vital to the measurements of rare K_L decays.

The production of the two beams began when the primary proton beam struck the BeO target. A series of magnets swept away unwanted charged particles, while a series of collimators aligned the beams into position. These elements are all shown in figure 2.2. Only 2 meters after the proton beam struck the target, the first magnet, referred to as the “target sweeper”, swept away charged particles and deflected them downward into a water-cooled copper beam dump. At a distance of $Z = 14$ meters, another magnet called “ μ -sweep1” swept charged particles (such as muons) away from the beam. This was followed by a lead absorber, at $Z = 18.5$ meters, whose primary function was to remove photons since they would convert into e^+e^- pairs which were

swept away by other magnets further downstream.

The two beams were first defined by the “primary collimator” at $Z = 20$ meters which was made of steel and brass. Its two square holes, whose centers were separated by 1.6 mrad, shaped the two beams. At $Z = 22$ meters another magnet, called “ μ -sweep2”, swept any remaining charged particles, such as scattered muons and particles that may have been produced by interactions in material upstream. The “spin rotator dipole” magnet, located at $Z = 30$ meters, was used to change the polarization of neutral hyperons in the beam (Ξ^0 , Λ^0) for rare hyperon decay analyses in KTeV [47]. This magnet had no effect on the neutral kaons since they are spinless. The “slab collimator”, located at $Z = 40$ meters in between the two beams, is made of stainless steel and prevented particles from crossing over to the neighboring beam. This collimator was removed during the “summer” data taking period. This was followed by the “jaw collimators” which were used for further shaping of the beams. During calibration data taking periods the iron “beamstop” was put in at $Z = 50$ meters, which provided beams of muons.

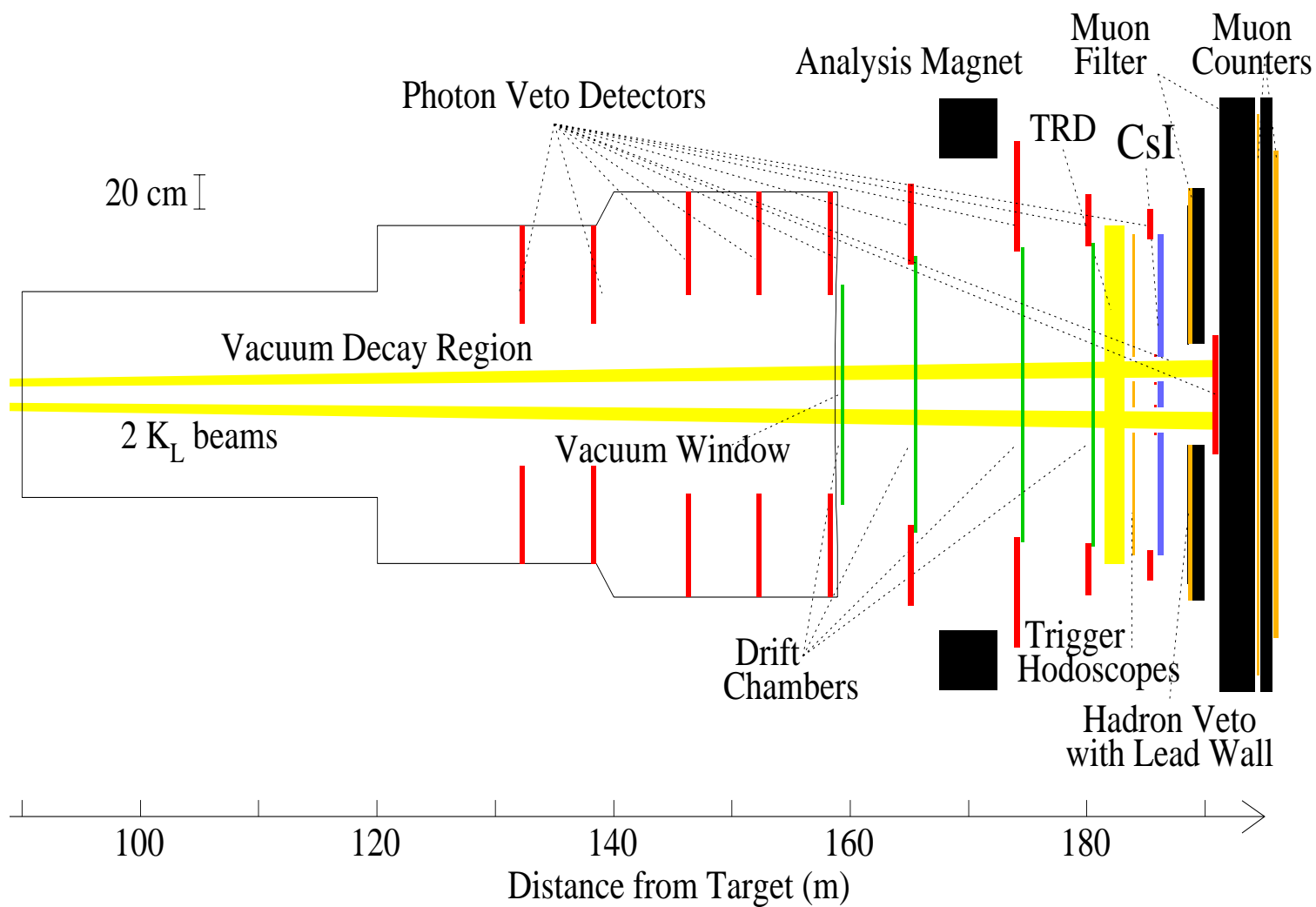
Further upstream in the NM3 enclosure, at $Z = 85$ meters the “defining collimator”, composed of tungsten, provided the beams with their final dimensions. During “winter” data taking conditions the two beams were $(4.4 \times 4.4) \text{ cm}^2$ and during the “summer” they were $(5.2 \times 5.2) \text{ cm}^2$. The “final sweeper” magnet was located at $Z = 90$ meters and removed any lingering charged particles in the neutral beam from upstream interactions and decays.

This brings us to the beginning of the KTeV decay region. The two beams, by this point, were predominantly composed of neutrons and K_L . The ratio of neutrons to kaons was approximately 3 : 1 and the total neutral hadron rate was 25 – 50 MHz. The neutral beams were also composed of very small levels of K_S , Λ and Ξ particles.

2.2 The KTeV Detector

This section describes the details of the KTeV detector elements during E799-II running conditions. Figure 2.3 shows a schematic plan (or top) view of the entire detector. The

Figure 2.3: Schematic plan view of the KTeV E799-II detector.



principal elements are labeled and their distance from the target (Z) in meters is labeled.

2.2.1 Decay Volume

The K_L decay region began at $Z = 93$ meters and ended at $Z = 159$ meters. The decay region was held under vacuum at a pressure of 1×10^{-6} torr ¹. The decay tank was made of cylindrical steel pipes of increasing size, ranging from 15 cm to 1.8 meters in diameter. The end of the decay volume was marked by a circular vacuum window (radius $r = 0.9$ meters) composed of kevlar and laminated with mylar. The vacuum window was 0.0015 radiation lengths in the Z -direction.

The vacuum window was followed by a helium bag secured by a mylar window. This was followed by a 10 cm air gap, in which a safety shutter was lowered during times the detector needed to be accessed.

Located in the vacuum decay region, there was a set of five photon veto detectors called “Ring Counters” (RC) [52]. The RC’s provided hermetic detection of particles escaping the detector (in particular, photons). These detectors had an overall round shape with an inner square aperture, which allowed the neutral K_L beams to pass through without interacting with any material (see figure 2.4). The counters were made of 24 lead-scintillator layers which were 16 radiation lengths in Z . The first 16 layers were each 0.5 of a radiation length and the final eight layers were 1.0 radiation length each. They were also azimuthally divided into 16 modules. Each module was connected to fiber optic light guides, whose scintillation light was fed to photomultiplier tubes (PMT). These signals were digitized and discriminated and sent to the trigger system. The RC positions and dimensions are shown in table 2.1.

2.2.2 Spectrometer

The spectrometer was used to measure the trajectory and the momentum (and thus the charge) of the charged particles. It was also used to find the vertex of the decay particles.

¹The vacuum region began at $Z = 50$ meters.

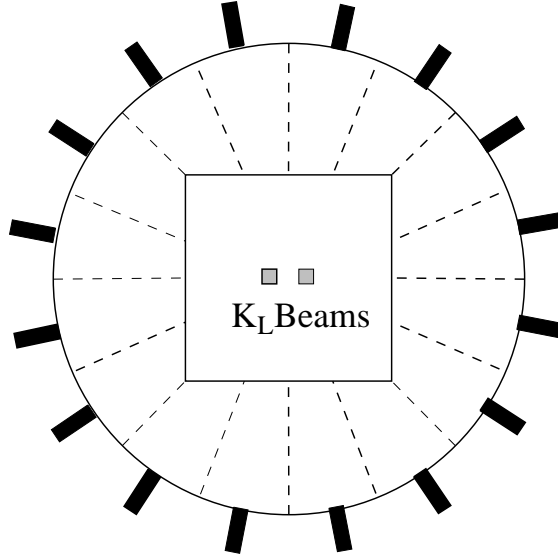


Figure 2.4: Cross-sectional view of a Ring Counter. The RC positions and dimensions are shown in table 2.1.

Table 2.1: Positions and Dimensions of the Ring Counters.

Ring Counter	Z position(m)	Outer radius (m)	X(m) \times Y(m)
RC6	132.6	1.00	0.84×0.84
RC7	138.6	1.00	0.84×0.84
RC8	146.6	1.44	1.18×1.18
RC9	152.6	1.44	1.18×1.18
RC10	158.6	1.44	1.18×1.18

Drift Chambers and Magnet

The spectrometer consisted of four drift chambers (DC), a magnet and plastic bags filled with helium. The DC frames were used in previous experiments [53, 54, 55]. Figure 2.5 [43] shows the setup of the spectrometer elements. The DC's downstream (DC3 and DC4) were larger than the ones upstream (DC1 and DC2) and their cross-sections ranged from $1.3\text{m} \times 1.3\text{m}$ to $1.9\text{m} \times 1.9\text{m}$. This allowed a higher acceptance of tracks with large bending angles. The magnet was a dipole magnet with a transverse momentum kick of around 200 MeV/c in the +X direction and was located between DC2 and DC3. The magnetic field was 2000 Gauss in the vertical direction so that tracks

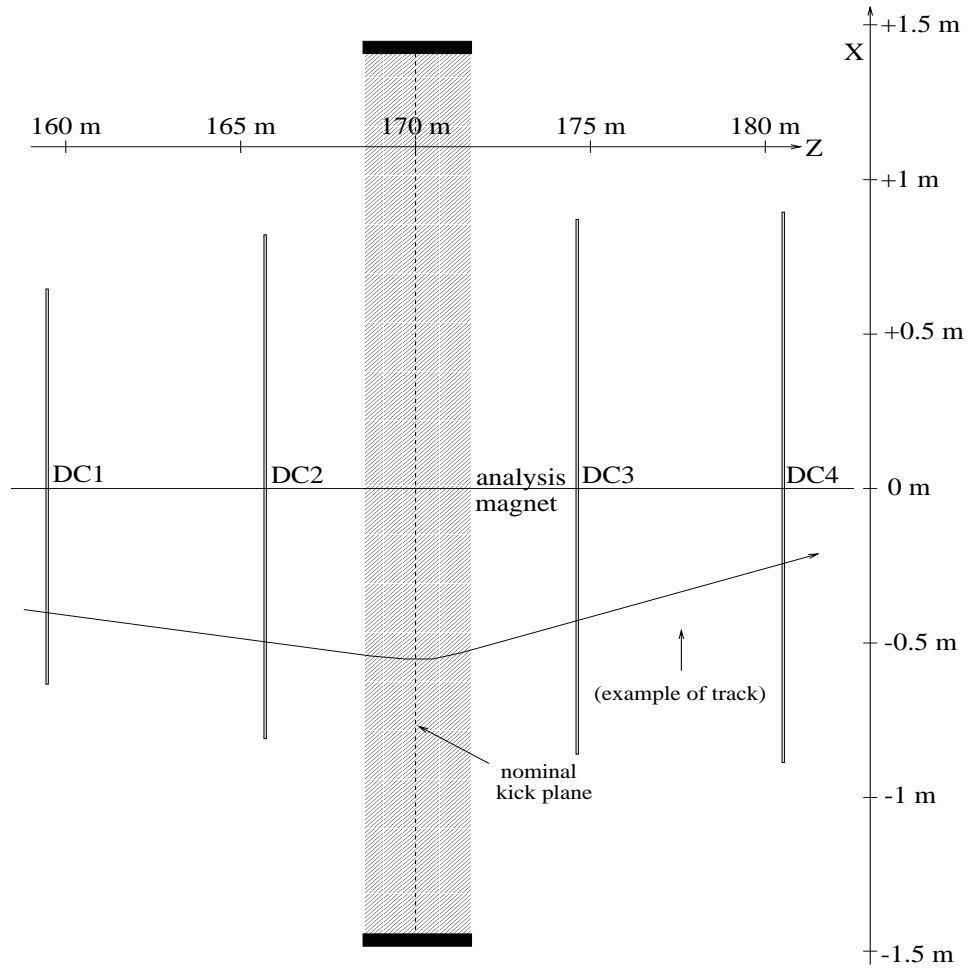


Figure 2.5: The plan view of the spectrometer elements.

Table 2.2: Positions and Dimensions of the Spectrometer elements.

Spec. Element	Z position(m)	X (m) \times Y (m)
DC1	159.4	1.30×1.30
DC2	165.6	1.64×1.44
Magnet	170.0	2.90×2.00
DC3	174.6	1.74×1.64
DC4	180.5	1.90×1.90

bend in the X-direction. The polarity of the magnetic field was periodically flipped to reduce possible systematics. The helium bags were located in between the chambers to reduce multiple scattering of particles, photon conversions and beam interactions. The positions and dimensions of the spectrometer elements are shown in table 2.2.

The DC's were designed to capture position information of the tracks in both the X and Y directions. Each chamber consisted of two plane pairs. The two upstream planes were made of wires parallel to the Y-axis (X, X') and the two downstream planes were made of wires parallel to the X-axis (Y, Y'). The four planes were defined by the sense (or anode) wires which were 1-mil gold-plated tungsten. The field shaping (or cathode) wires were made of 4-mil gold-plated aluminum and formed a hexagon around the sense wires (a drift cell). The sense wires within a plane were separated by 12.7 mm, which also defined the size of the cell. Adjacent sense planes were offset by 6.35mm to reduce the ambiguity of the measurement of the particle position. There were also two planes of window guard wires located at the upstream and downstream ends of each chamber. These wires were made of 4-mil gold-plated aluminum. The configuration of the planes and wires within a DC is shown in figure 2.6.

Each DC was filled with 49.75% argon and 49.75% ethane by volume, with 0.5% isopropyl alcohol during the winter run and 1.0% alcohol during the summer run. The alcohol was added to help prevent chamber aging. When a charged particle traveled through a chamber, ion pairs were deposited into the argon-ethane mixture. The freed electrons drifted to the sense wires and the ions drifted to the field wires. The drift speed was roughly constant at $50\mu\text{m}/\text{nsec}$, with average drift times of less than 200 ns. The voltage on the field and window wires were 2450V-2600V with respect to the sense

wires.

Using electronics mounted to the DC's, the sense wire signals were amplified and discriminated. The signals were then digitized using time-to-digital converters (TDC) and were sent to the triggering system. The TDC times were precise to about 0.5 ns. The drift times were converted to drift distances which resulted in obtaining the positions of the tracks. These time to distance conversion maps were calibrated throughout the running period. The sum of two drift distances (SOD) of adjacent sense wires were calculated for a pair of hits (or signal) for one track. The SOD should be equal to the offset of 6.35 mm. The SOD distributions reveal that the position resolution from the DC's is around $100\mu\text{m}$.

The momentum resolution of the spectrometer was measured [45] to be

$$\frac{\sigma(p)}{p} = 0.38\% + 0.016\% \times p \quad (2.1)$$

where p is the momentum of a track measured in GeV/c. The constant term is due to multiple scattering. The linear term reflects that the resolution deteriorates for higher track momenta due to the finite position resolution of the spectrometer.

Spectrometer Anti

The spectrometer anti (SA) [56, 57] consisted of three photon veto counters, much like the RC's described in section 2.2.1. SA2, SA3 and SA4 were located slightly upstream of DC2, DC3 and DC4, respectively. They were rectangular counters and were composed of 32 layers of a lead-scintillator sandwich. Each layer was 0.5 radiation lengths resulting in a total of 16 radiation lengths. There were a total of 28 modules, each connected to fiber optic light guides, whose scintillation light was fed to PMT's. These signals were digitized and discriminated and sent to the trigger system. The SA positions and dimensions are shown in table 2.3 and a sketch of an SA is shown in figure 2.7.

2.2.3 Calorimeter

The electromagnetic calorimeter was used to precisely measure the energies of e^\pm 's and γ 's. The positions of particles interacting with the calorimeter were also recorded and

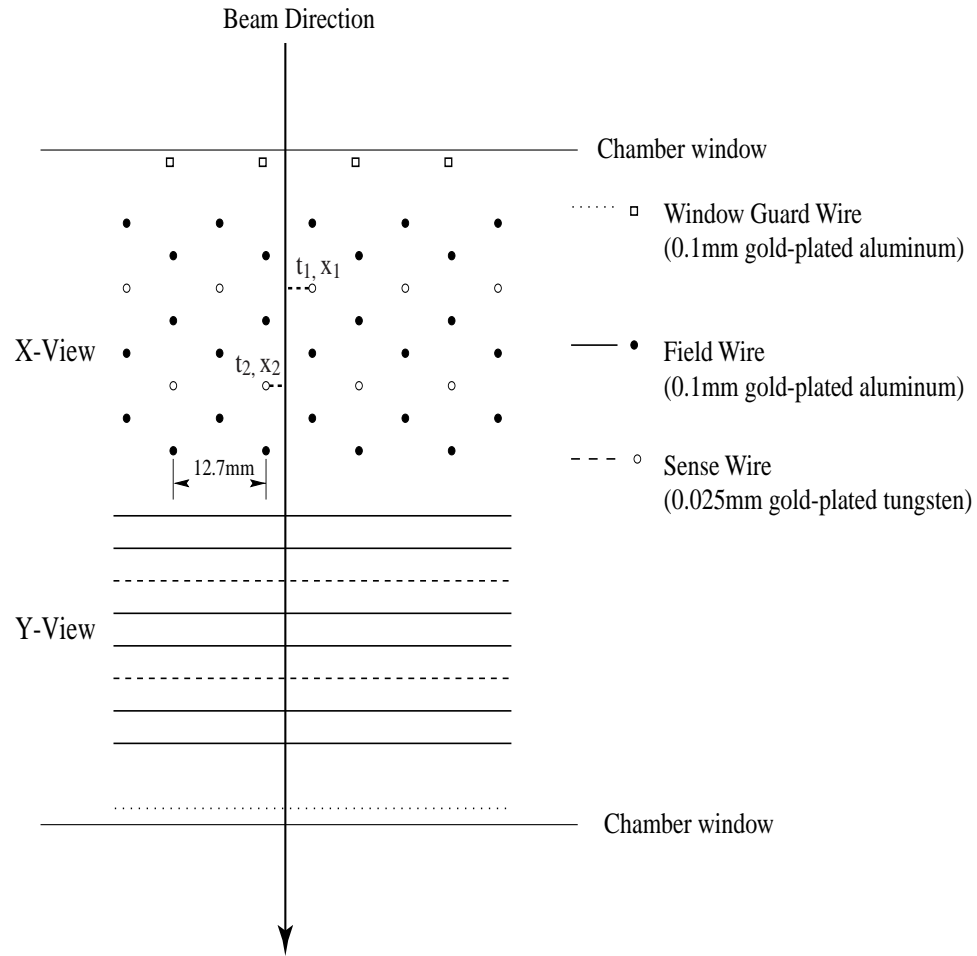


Figure 2.6: The configuration of the planes and wires within a DC. The beam direction is shown by the long arrow. The planes are defined by the sense wires, with the field wire forming a hexagon around the sense wires.

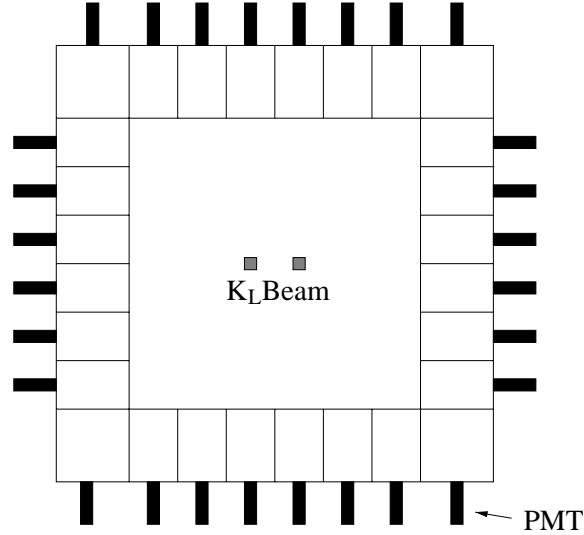


Figure 2.7: Cross-sectional view of a Spectrometer Anti. The SA positions and dimensions are shown in table 2.3.

Table 2.3: Positions and Dimensions of the Spectrometer Anti.

SA	Z position(m)	Outer X(m) \times Y(m)	Inner X(m) \times Y(m)
SA2	165.1	2.50×2.50	1.54×1.37
SA3	174.0	3.00×2.40	1.69×1.60
SA4	180.0	2.37×2.37	1.75×1.75

for charged particles could be combined with the DC information of tracks.

Crystal Array

The calorimeter was composed of an array of 3100 pure cesium iodide (CsI) crystals [58]. It was located at $Z = 186.0$ meters and had total dimensions of $1.9\text{m} \times 1.9\text{m} \times 0.5\text{m}$. There were two 15cm^2 holes to allow the beams to pass through with no interactions. A schematic of the calorimeter is shown in figure 2.8. There were 2232 small crystals of dimensions $2.5\text{cm} \times 2.5\text{cm} \times 50\text{cm}$ and were located in the inner portion of the array. There were 868 large crystals of dimensions $5.0\text{cm} \times 5.0\text{cm} \times 50\text{cm}$ and were located in the outer portion of the array. The dimension in Z of the crystals corresponds to 27 radiation lengths, chosen to completely capture the electromagnetic showers of the

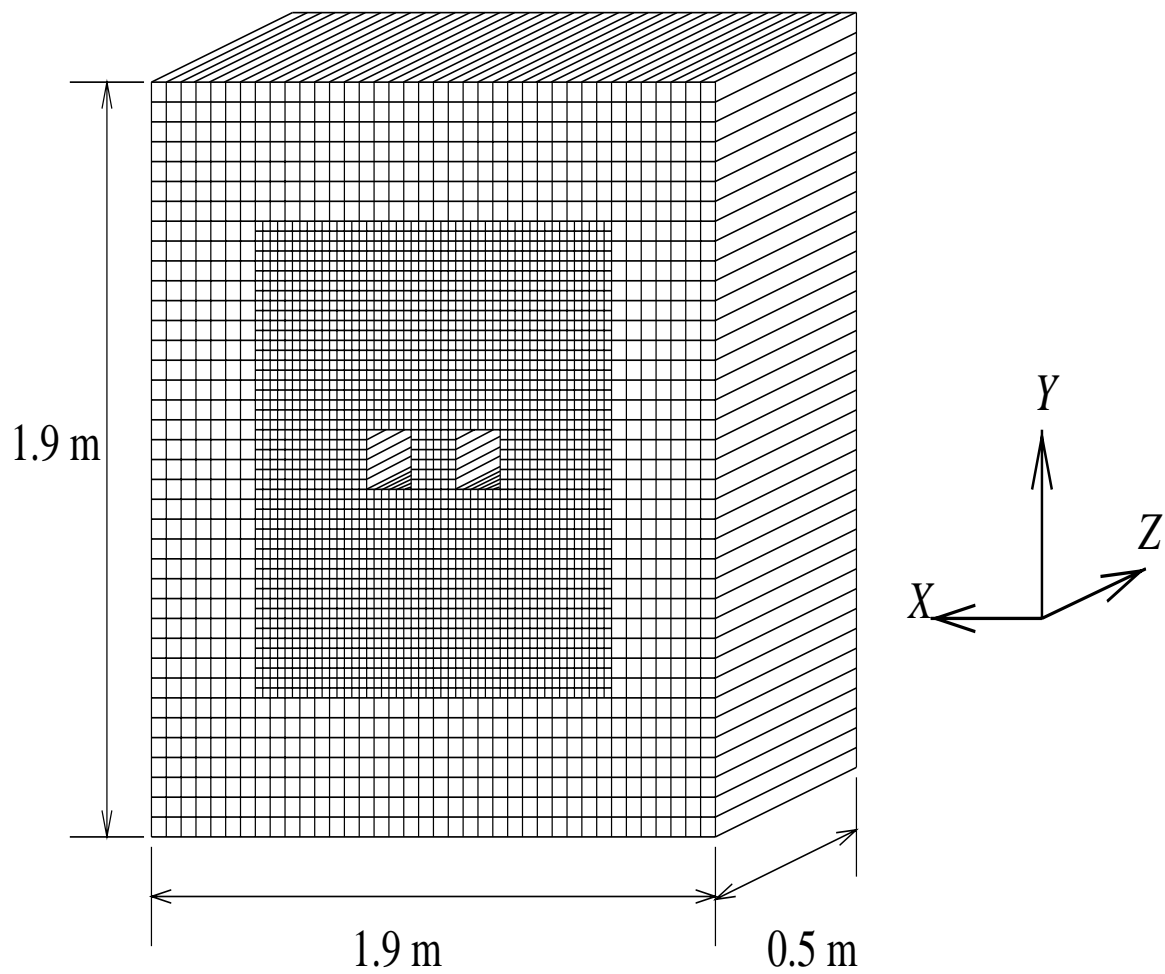


Figure 2.8: Schematic of the CsI calorimeter.

e^\pm 's and γ 's. This length also corresponds to 1.4 nuclear interaction lengths, thus making some hadrons (such as π^\pm) minimum ionizing particles (MIP). Each crystal was wrapped in $13\mu\text{m}$ of aluminized mylar (upstream) and black mylar (downstream) such that the light output was uniform along the Z direction and to isolate the crystals from each other.

The entire CsI array was in a light tight, temperature controlled blockhouse. In addition, the humidity in the blockhouse was monitored and kept to a low level ($< 4\%$) to minimize the absorption of moisture in the air of the CsI crystals.

The position resolution of the small crystals was 1 mm and in the large crystals was 1.8 mm. The photon energy resolution was

$$\frac{\sigma(E)}{E} = 0.45\% + \frac{2\%}{\sqrt{E}}, \quad (2.2)$$

where E is measured in GeV. The constant term is a result from mainly shower fluctuations. The $1/\sqrt{E}$ dependence results from photon statistics in scintillation light. The CsI calorimeter yielded a very high electron/pion rejection of 500/1.

Readout System

Each crystal was connected to its own PMT, which was fed the scintillation light signals. An optical link between the crystal and PMT faces was created by the use of a transparent RTV rubber cookie. The PMT's were operated at -1200V with a gain of 5000. Each PMT also was connected to its own digital PMT base (DPMT). The dynode output of a PMT was sent to the triggering system, while the anode output was sent to the DPMT.

The main functions of the DPMT circuit boards were to digitize and store the PMT signals. The DPMT's contained custom made chips [59] that converted charge to energy (QIE) by integrating the current output to the PMT's. The QIE chips were analog-digital hybrids and were synchronized to the RF of the Tevatron. This resulted in no deadtime of the readout system. The voltage output of the QIE was sent to a Flash Analog to Digital Converter (FADC) which digitized the signal. This digitized signal was sent to another custom made chip called the Driver-Buffer-Clock (DBC).

The DBC synchronized the signals it received. In the end the signals were sent to the trigger system through a “pipeline”. The pipeline was a custom buffer system that sparsified the incoming signals and was set specially for each physics trigger.

CsI Anti and Collar Anti

Another veto counter was located upstream of the calorimeter. The cesium iodide anti (CIA) was rectangular and was composed of 16 radiation lengths of lead and scintillator layers, just like the SA’s (see figure 2.7).

A set of veto counters surrounded the beam holes at the upstream edge of the CsI. They were in the shape of rectangular collars and are referred to as the collar anti (CA) [60]. A schematic of the CA is shown in figure 2.9. The CA was composed of a three layer tungsten-scintillator sandwich. Each layer of tungsten was 2.9 radiation lengths. The counter on each beam hole had four modules (top, bottom, left, right) connected to PMT’s. The PMT signals were digitized and discriminated and sent to the trigger system. The CA was used to veto events with electromagnetic particles hitting the CsI close to the edges of the beam holes. Such events were rejected to ensure that the CsI energies were well measured.

The positions and dimensions of the CIA and the CA are shown in table 2.4.

Table 2.4: Positions and Dimensions of the CIA and CA.

Counter	Z position(m)	Outer X(m) \times Y(m)	Inner X(m) \times Y(m)
CIA	185.2	2.20×2.20	1.84×1.84
CA	185.9	0.18×0.18	0.15×0.15

2.2.4 TRD’s

The transition radiation detectors (TRD) could also be used for particle identification, specifically to enhance the pion-electron discrimination. The TRD’s were not used in this analysis since the pion-electron discrimination of the calorimeter was superior. Detailed descriptions can be found in [44, 43].

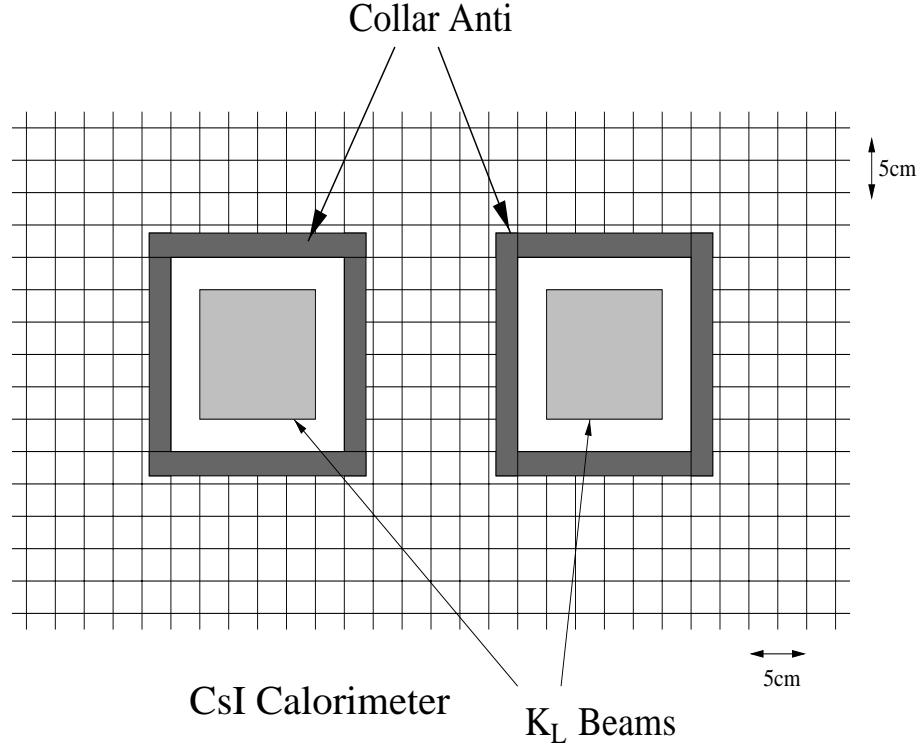


Figure 2.9: Schematic of the Collar Anti.

2.2.5 Trigger Hodoscopes

The trigger hodoscopes were designed to count the charged particles at the trigger level. The hodoscopes were two planes of 1 cm thick scintillator. The upstream hodoscope was called the V bank and the downstream one was called the V' bank. They were both located upstream of the CsI; the V bank was located at $Z = 183.90$ meters and V' at $Z = 183.95$ meters. They were each arranged in an array of paddles in the vertical direction, 16 paddles above and 16 paddles below the beam. The total cross-sectional area was $1.9\text{m} \times 1.9\text{m}$ with two 14cm^2 beamhole to minimize beam interactions. The paddles were of five different widths (9.92 cm, 11.82 cm, 13.74 cm, 15.63 cm, 17.76 cm) to reduce inefficiencies due to cracks. To avoid double counting by one charged particle, there were no overlaps between the paddles in each bank. Figure 2.10 shows a schematic of the trigger hodoscopes.

There were PMT's mounted on the top and bottom of each paddle through light

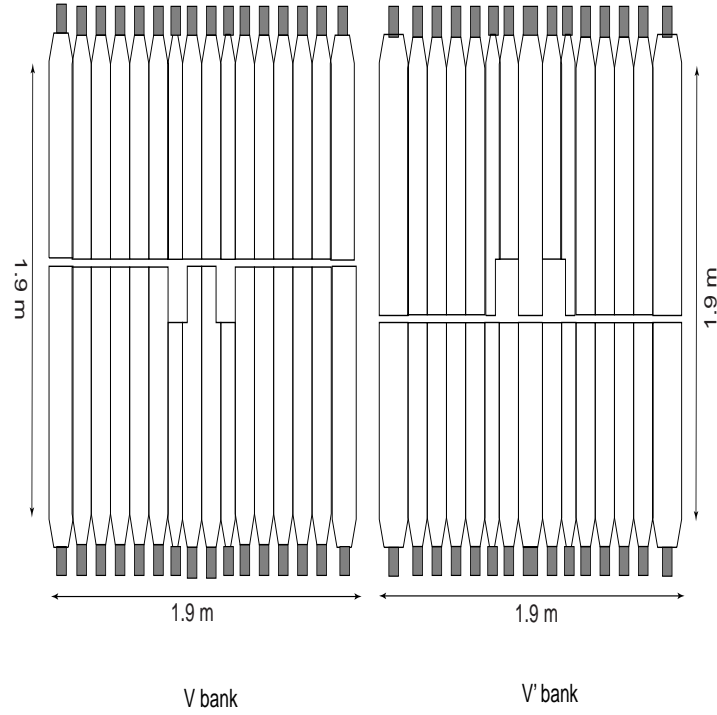


Figure 2.10: Schematic of the trigger hodoscopes. They were located about 2 meters upstream of the CsI. The V bank was located slightly upstream of the V' bank.

guides. The analog signals were summed and discriminated and sent to the trigger system. Every charged trigger required hits in the trigger hodoscopes.

2.2.6 Lead Wall and the Hadron Anti

A 15 cm thick lead wall (or 0.9 radiation lengths) was located at $Z = 188.5$ meters, downstream of the CsI. The total cross-section of the lead was $2.43\text{m} \times 2.43\text{m}$. There was also a hole in the center of the wall $60\text{cm} \times 30\text{cm}$ to allow the beams to pass through without interacting. The lead wall was placed there to absorb traces of electromagnetic showers leaking from the CsI. It also produced hadronic showers of hadrons (such as π^\pm) that did not shower in the CsI.

Immediately following the lead wall was the hadron anti (HA) at $Z = 189.0$ meters [61]. The HA was placed there to detect the hadronic showers from the lead wall. It was composed of 28 scintillator paddles, 14 above and 14 below the beam. The total cross-section of the HA was $2.24\text{m} \times 2.24\text{m}$. There was also a hole in the center of the

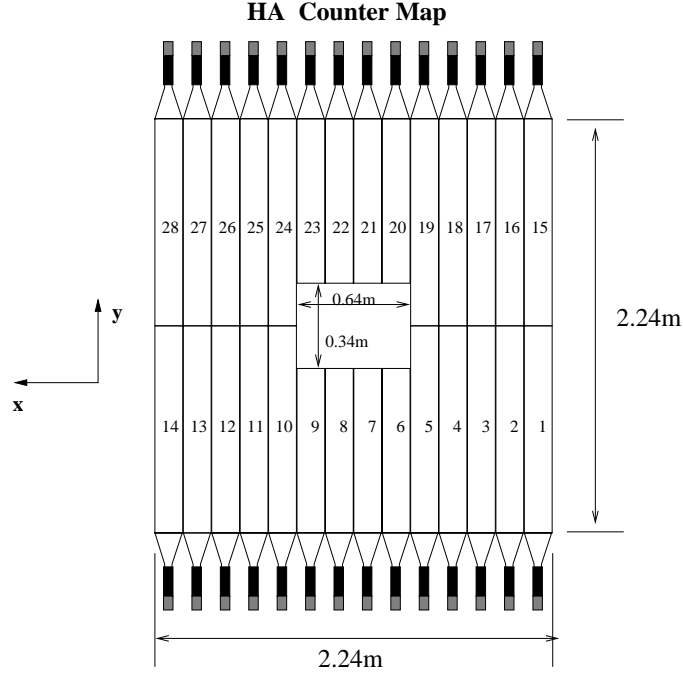


Figure 2.11: Schematic of the Hadron Anti.

HA $64\text{cm} \times 34\text{cm}$ to allow the beams to pass through without interacting. Each paddle was connected to a PMT, whose analog signals were summed, discriminated and set to the trigger system. Hadronic activity could be rejected by triggering on the HA. A schematic of the HA is shown in figure 2.11.

2.2.7 Muon System

A steel wall 3 meters long, located at $Z = 191.7$ meters, was used to stop nearly all particles except muons. The cross-sectional area of the wall was $4.3\text{m} \times 3.4\text{m}$. Following this steel wall was the MU2 counter located at $Z = 194.8$. This counter was made of 56 scintillator paddles, whose dimensions can be seen in the bottom of figure 2.12. This counter was designed to be large since it was located so downstream and was needed to capture muons that scattered in the steel. Following MU2, at $Z = 195.3$ meters, was another wall of steel 1 meter long with a cross-sectional area of $3.5\text{m} \times 3.6\text{m}$. The MU3 counters were located at $Z = 196.4$ meters. These consisted of 40 paddles of scintillator

each and are shown in figure 2.12 top. One of the MU3 counters were oriented in the X-direction and the other in the Y-direction.

Individual muon paddles had dimensions of $15\text{cm} \times 150\text{cm}$. Two of these paddles formed an entire paddle, overlapping by 1 cm reducing the inefficiency of the muons traversing the gap between them.

Each paddle was connected to a PMT, whose analog signals were summed, discriminated and set to the trigger system. These counters were used to trigger events with muons. In this analysis, only MU2 was used to veto events with muons. The muon system is described in great detail in [41].

2.2.8 Accidental Counter

In order to accurately simulate the activity in the detector, it was necessary to collect events that reflected “accidental” activity. Accidental activity is activity from beam particle interactions uncorrelated to detector activity. It is important to understand accidentals since they can corrupt the signature of a particular kaon decay.

The “90°” accidental counter was placed near the target. This counter was composed of 3 scintillator paddles placed 90° with respect to the beam direction (or Z direction), 1.8 meters away from the target. These telescope-like counters viewed the target through a small hole, $\frac{1}{4}\text{in} \times \frac{1}{4}\text{in}$, in the target pile (see figure 2.2). Each block of scintillator was $\frac{3}{4}\text{in} \times \frac{3}{4}\text{in} \times \frac{7}{16}\text{in}$ and were separated by 1.5 in. Their signals were sent to the trigger system and when all three counters fired in coincidence the accidental trigger was satisfied, thus causing a snapshot of the detector to be written to tape.

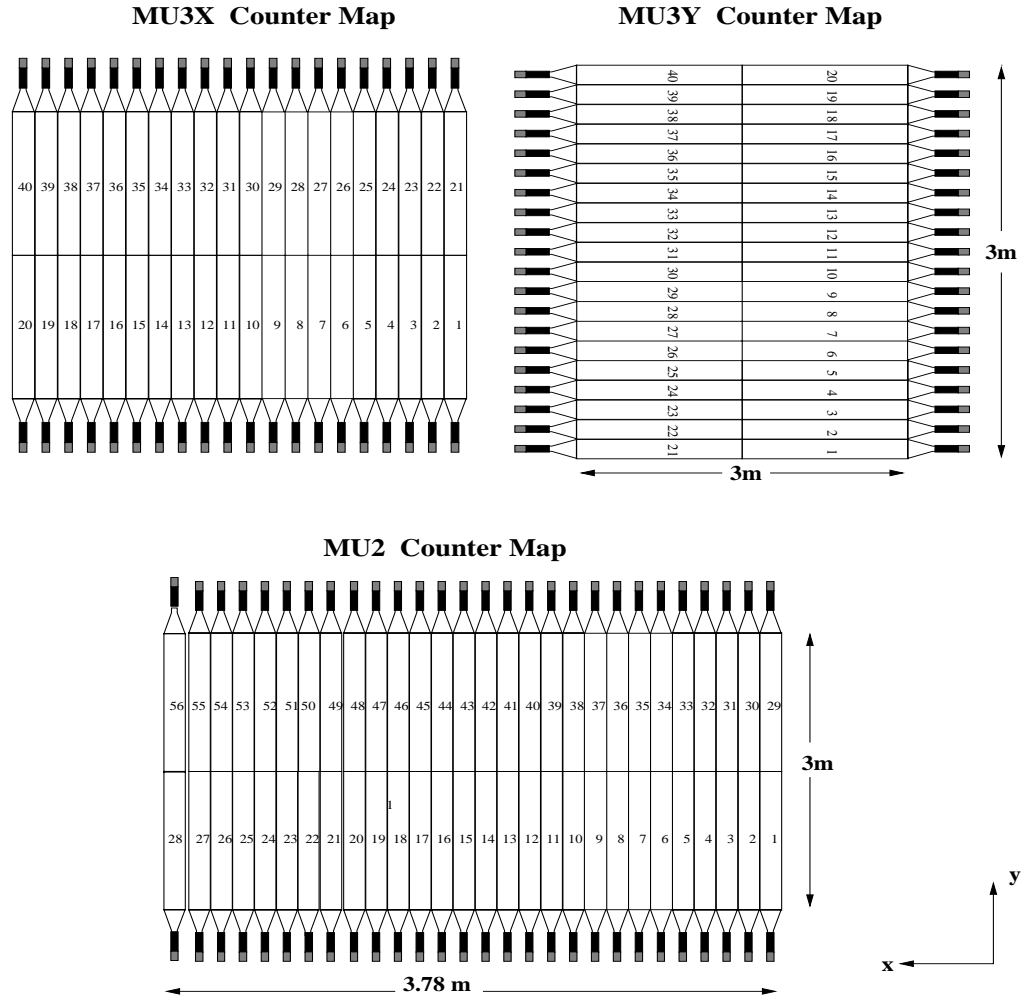


Figure 2.12: Schematic of the Muon System counters.

Chapter 3

Event Selection

In KTeV, there were two stages to the event selection process. The first stage occurred while the data was being collected (online) and the second after the data was collected (offline). The trigger system defined the online selection process, after which the data was reduced offline into physics analysis subsets.

3.1 Trigger

Due to the high rate of kaon decays in KTeV ($\sim 1\text{MHz}$), the trigger system was designed to quickly decide to accept the events of interest while rejecting the events of no interest, which were the majority. The trigger was composed of three levels and they are briefly described below. A detailed description of the E799-II trigger is in [46].

3.1.1 Level 1

The first level of triggering used hardware logic. As described in chapter 2, signals from phototubes from the RC/SA/CIA photon vetoes, the trigger hodoscopes V and V' , the HA and muon counters and the sum of the total energy from the CsI were all sent to the triggering system. These were the fastest signals the detector had available since they were processed within one RF bucket (see section 2.1.1). There was another set of signals used in the level 1 trigger called the Drift Chamber OR (DCOR) [62]. The sources of these signals were the X and Y plane pairs of DC1 and DC2. These signals were not as fast as the others and were processed within 4-5 buckets.

These signals were synchronized to the RF of the Tevatron to within 2 ns and the trigger decisions were made using a logical combination of these signals. Effectively, the level 1 trigger had no deadtime.

3.1.2 Level 2

The level 2 trigger was also a hardware trigger and was a slower trigger than level 1. The types of decisions the level 2 trigger made were more time consuming and ranged from 800 ns - 2.5 μ s. There was no level 1 triggering during level 2. For events which passed the level 2 trigger there was a deadtime of 15 μ s to allow data to be sent to the next level of the triggering system.

There were six systems that were used to decide if an event would pass the level 2 trigger. The functions of these systems were:

- Hit counting in the DC's.
- In-time pair finding in the DC's.
- Finding tracks in Y-direction in the DC's.
- Cluster counting in the CsI.
- Electron tagging in the TRD's.
- Stiff track trigger for hyperon decays.

Only the first four systems above were used in the events selection for this analysis and are described below.

Hit Counting

Electronics modules integrated with the DC's were used to count the number of hits in the X and Y views in DC1-DC4. The information of a hit being in-time with the bucket that triggered level 1 was not available through these modules. The hit counting information had a processing time of 800 ns.

In-time Pair Finding

The TDC's described in chapter 2 were used to measure if a hit in the DC's were in-time. Electronics modules were used to reject out-of-time hits. Pairs of in-time hits were used to calculate a SOD (the sum of two drift distances; again see chapter 2) and

the means of the SOD's were used to decide when events passed the level 2 trigger. The in-time pair finding had a processing time of 800 ns.

Hardware Cluster Counting

A shower of energy was deposited in the CsI calorimeter for electromagnetic particles and was defined as a “cluster” if the energy was > 1 GeV. The hardware cluster counter (HCC) [63, 64] counted in-time clusters with the discriminated PMT signals from the 3100 CsI crystals. The HCC recorded which CsI channels were “on”. The HCC consumed the longest processing time of the level 2 trigger of 2μ s.

Y-track Finding

The Y-track finder (YTF) [65] used the DC hit information from the hit counting and in-time pair finding modules described above and searched for hit patterns in the Y-direction. The hit and position information of the Y-views in the upper and lower parts of the DC's were sent to the triggering system for processing.

3.1.3 4TRACK Trigger

The data for this thesis were collected in trigger called the 4-track trigger, designed for decays with a four charged particle final state. The level 1 and level 2 elements of this trigger were as follows:

LEVEL 1:

- 3V-TIGHT: ≥ 3 hits in V and ≥ 3 hits in V' .
- 2DC12-MED: 3 out of 4 DC12 planes with ≥ 2 hits, 1 plane with ≥ 1 hit.
- ET-THR1: E_{TOTAL} of CsI ≥ 11 GeV.
- $\overline{MU2}$: Veto events with ≥ 1 hit (15 mV, 0.2 MIP) in MU2.
- \overline{PHV} : Veto events with ≥ 500 MeV in PHV or events with ≥ 400 MeV in the SA.

- \overline{CA} : Veto events with ≥ 14 GeV in the CA.

LEVEL 2:

- 34-HCY: require ≥ 3 hits in DC1Y, ≥ 3 hits in DC2Y and ≥ 4 hits in DC3Y, ≥ 4 hits in DC4Y.
- HCC-GE2: require ≥ 2 HCC clusters.
- YTF-UDO: require a good track in the upper half and good track in the lower half or one good central track.
- 3HC2X: require ≥ 3 in-time hits in DC2X.

3.1.4 Level 3

The next level of triggering, level 3, was a software trigger. The level 3 trigger is also referred to as the “filter code”. The output of the level 2 trigger was interfaced with the data acquisition system (DAQ) [66, 45, 47, 44] composed of four SGI challenges. The level 3 software performed quick offline reconstruction of events, which were subsequently written to 10 GB Digital Linear Tapes (DLT). Software tags were created for different criteria which had a basis on predetermined physics analyses. The details of the level 3 filtering code can be found in [67].

The level 3 filter code requirements to tag an event as a four-track event were ¹:

- Find at least three tracks in the DC X view and at least three tracks in the Y view. No sharing of hits between two tracks.
- Find at least one vertex candidate.
- Require the reconstructed vertex Z position to be between 90.0 and 158.0 meters.

3.2 Data Reduction

At the end of the winter and summer running periods, 850 DLT’s worth of raw rare decay data was collected. The winter runs ranged from run number 8028-8910 and

¹See chapter 4 for the details of event reconstruction.

the summer runs from 10463-10970 ². Since the 850 tapes contained all the data for all analyses, there were two basic steps taken to reduce the data: the “split” and the “crunch”.

3.2.1 E799 Split

The E799 “split” refers to a sorting of the data into smaller subsets based on different physics interests. There was a total of 19 different output streams based on trigger type and level 3 tags and written to tape. Some of the output streams were based on data collected for calibration purposes and also accidental activity data used in the detector simulation (see chapter 5).

The trigger used in this analysis, the 4TRACK trigger, were split and copied to a total of 82 DLT’s, 38 DLT’s of winter data and 44 DLT’s of summer data.

3.2.2 4TRACK Crunch

The 82 DLT’s containing the 4TRACK data was still unwieldy and was further reduced. This time the tapes were “crunched” to a sample that met more requirements specific to this analysis. The crunch code was similar to the filter code, yet included more sophisticated track, cluster and vertex finding methods. For this analysis, the crunch code requirements were:

- Verify that the level 3 4TRACK tag was set.
- Find DC tracks and allowed a single Y-track to share two X-tracks.
- Find at least one vertex candidate.
- At least three tracks must match with a CsI cluster.
- Find at least three electrons, defined as the ratio of the calorimeter energy (E) to the track momentum (p) to be $0.9 < E/p < 99.0$.

²In this analysis, runs less than run 8245 were not used due to a swapped HCC cable. This accounts for less than 1% of the winter data.

The details of the 4TRACK crunch are in [68]. At the end of the crunch the data was reduced to two DLT's used in this analysis, one tape for the winter data and one for the summer. Therefore, the data was reduced to an easily manageable level for analysis.

Chapter 4

Event Reconstruction

In this analysis, the final state is composed of four charged particles. This chapter describes the algorithms for reconstruction of charged particles. Reconstruction included finding tracks using drift chamber (DC) information, which were used to measure the trajectories and momenta of the charged particles. Reconstruction also included finding CsI clusters to measure energies of electromagnetic particles and matching them to tracks to find the decay charged vertex. This chapter also describes the calibration of the DC and CsI detectors. Calibrations of other detector systems are discussed in [45, 41].

4.1 Track Finding

4.1.1 Hit Pairing

The first step in finding tracks was to look for signals (or hits) in the drift chambers from the TDC's (see chapter 2). Only hits that were in-time, or within a window of 115 ns to 350 ns, were used in the track finding algorithm. In the event when a wire had more than one hit, only the earliest hit was used. The TDC signals recorded the drift times, which were converted to drift distances using a conversion table (or XT maps) described in section 4.1.3 on DC calibration.

When a charged particle traveled through the DC's, it resulted in hits in the adjacent sense wires surrounding the particle's trajectory. In other words, pairs of hits were produced in two sense wires of complementary pairs of sense planes (such as $X - X'$ or $Y - Y'$) when a charged particle traversed a DC. These hit pairs were the foundation of track reconstruction.

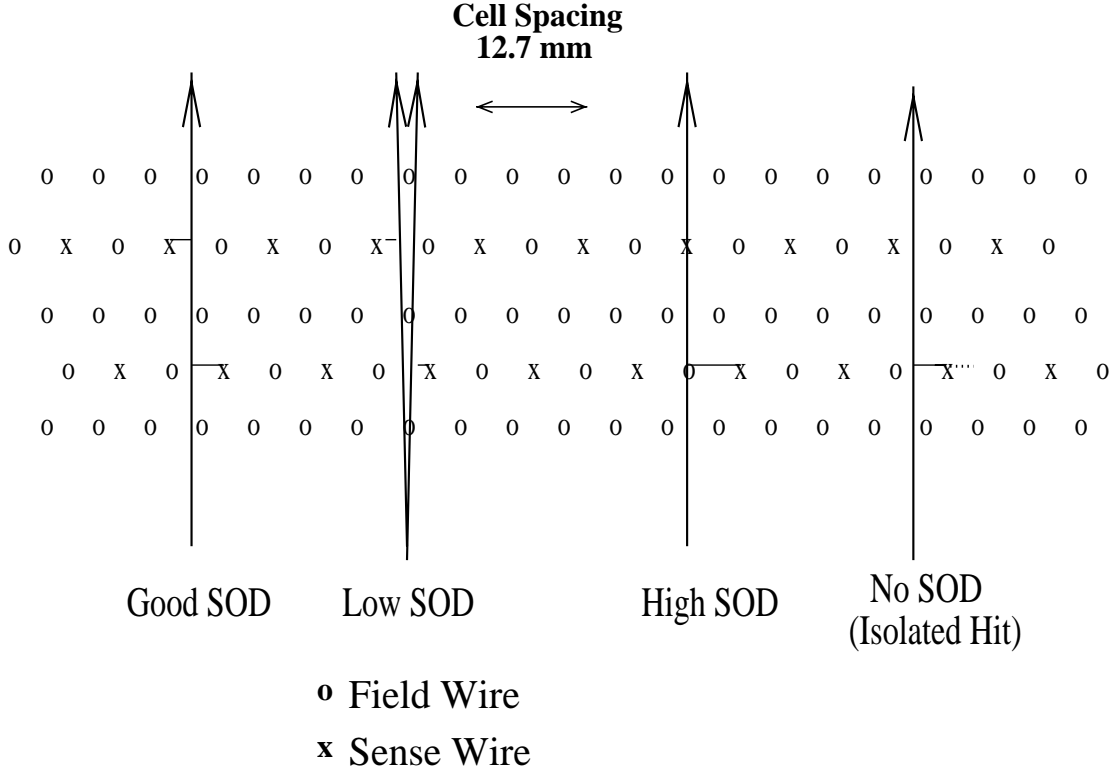


Figure 4.1: Illustration of different SOD categories. The vertical lines indicate part of the track trajectory (only one DC view is shown). The horizontal lines represent measured drift distances. The dotted horizontal line indicates that the track could have passed on either side of the sense wire for an isolated hit.

The drift distance from one sense wire was added to the drift distance of its corresponding hit pair from the adjacent wire to form the sum-of-distances (SOD). A SOD should ideally equal half the cell size or 6.35 mm. A hit pair accepted for track reconstruction was required to have a SOD that was different from half a cell size by less than $\pm 1\text{mm}$. (In DC3X and DC4X the difference was required to be within $\pm 1.5\text{mm}$ due to possible large angles of tracks deflected by the analysis magnet.) An illustration of a “good” SOD is shown in figure 4.1. A histogram of a typical SOD distribution is shown in figure 4.2 [43].

In addition, a “low” SOD was produced if two separate tracks were so close that they traveled through the same half cell. A low SOD was produced as a result of kaon decays with very small opening angles. Another possibility was that low SOD’s were

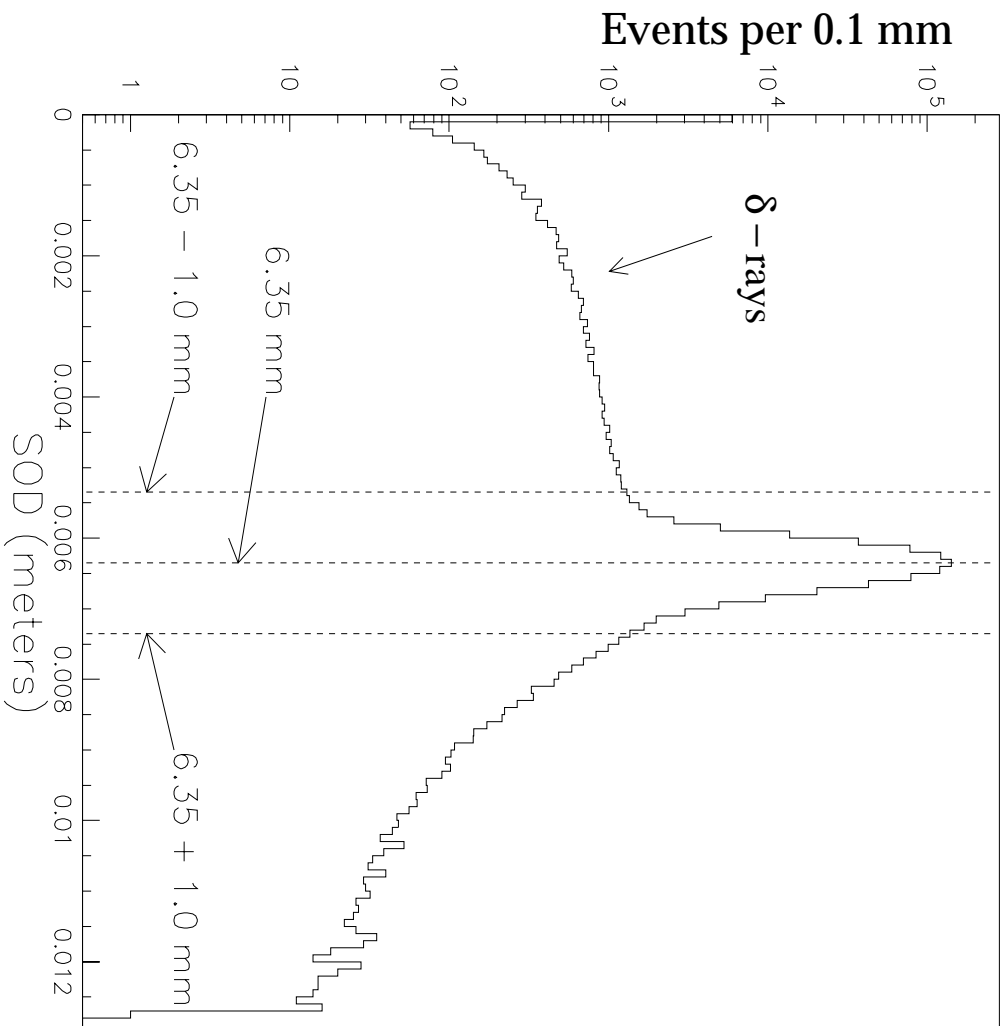


Figure 4.2: Typical SOD distribution in DC Y view. This distribution was constructed using $K_L \rightarrow \pi^0 \pi^0$ decays with one $\pi^0 \rightarrow e^+ e^- \gamma$. The spike at zero is due to isolated hits. The low side tail is mainly due to δ rays.

due to δ rays, high energy charged particles passing through material which ejected electrons sideways that traveled rapidly towards a sense wire. An illustration of a low SOD is also shown in figure 4.1.

A “high” SOD was produced if a track passed very close to a wire in one of the complementary sense planes. What made an SOD high was due to discrete ionization and inefficiencies in detecting electrons. An illustration of a high SOD is shown in figure 4.1.

One final possibility is that there was a missing hit in the complementary sense plane, referred to as an isolated hit. This was a result of inefficiencies in the wires, such as a defective wire due to contamination or a kink. The direction information of the track is missing in an isolated hit but could still be used in the overall track candidate decision making algorithm. An illustration of an isolated hit is also shown in figure 4.1, where the dotted line indicates that the track could have passed on either side of the sense wire.

4.1.2 X and Y Tracks

After pairing hits, the Y track candidate search began. It was simpler to search for Y tracks before X tracks since there was no magnet bending of the tracks in the Y direction.

To find a Y track, pairs of hits in DC1Y and DC4Y were located and defined a straight line. Then pairs of hits were identified in DC2Y and DC3Y that laid within 5 mm of the line. For each track, up to two low SOD hits or one isolated single hit and one low SOD hit were allowed, while all other hits were required to be good SOD pairs. Once a set of four pairs was found along a straight line, a least-squares fit to a straight line was performed and a fit χ^2 was calculated. To be considered a Y track candidate, the fit χ^2 was required to be less than $(2\text{mm})^2$. This was repeated for all combinations of DC1Y and DC4Y pairs. At this point, a minimum of two Y track candidates were required to accept the event.

Next, it was necessary to determine if the Y track candidates could coexist. Y tracks were not allowed to coexist if they shared any hits, with one exception. Tracks were

allowed to share hits and coexist if the tracks shared a hit in one sense plane of a sense plane pair, but not in the complementary plane, and for each track the hit was part of a good SOD pair. This prevented the rejection of events with tracks that passed through adjacent cells and the SOD's for both pairs happened to be "good". In addition, up to four low SOD hits or two isolated single hits plus one low SOD pair were allowed in the total number of track candidates. At least two coexisting Y tracks were required to accept the event.

The next step was to find the X tracks. In this view, the tracks were made up of two segments due to the magnet bend. The upstream X track segments were searched for first. Each pair of hits in DC1X and in DC2X defined a line for a possible upstream track segment. The angle between this line and the Z axis was required to be less than 100 mrad. Up to two low SOD hits or one isolated hit were allowed when finding an upstream track segment, otherwise all other hits were required to be good SOD pairs. Similarly, pairs of hits in DC3X and DC4X defined possible downstream track segments. The angle between the downstream line and the Z axis was required to be less than 150 mrad. In this case, at most one low SOD hit or one isolated single hit was allowed. For each upstream and downstream combination of X segments, the distance between the two segments, projected to the plane of the magnet bend at $Z = 170.0$ meters, was required to be within 6 mm to qualify as an X track candidate. In addition, just as for the Y track candidates, up to two low SOD hits or one isolated single hit and one low SOD hit were allowed to qualify as an X track candidate. At this point, a minimum of two X track candidates were required to accept the event.

It was again necessary to determine if the track candidates could coexist, this time in the X view. The X track candidates had the same requirements for coexisting as did the Y tracks. At least two coexisting X tracks were required to accept the event.

In order to match X track candidates with Y track candidates more information was necessary, at this point. This information is obtained from the CsI cluster positions.

4.1.3 Drift Chamber Calibration

A brief description of the DC calibration is presented here. Additional information of the DC calibration process is discussed in [69].

Time-to-Distance Calibration

The first step to calibrating the time-to-distance conversion was to calibrate the relative timing between wires. Variations in cable length and in channel or module differences of the TDC's created TDC timing offsets between wires. The TDC's ran with a trigger-provided common stop. The number of TDC counts for each wire that corresponded to zero drift distance was defined as the T0. A sharp edge in a TDC distribution for a wire also marked the T0 for that wire. Using plentiful $K_L \rightarrow \pi^\pm e^\mp \nu_e$ (K_{e3}) decay tracks, each TDC distribution edge for each wire was compared to the others to obtain the timing offsets.

Once all the T0 offsets were obtained, time-to-distance (XT) maps for each chamber were calculated. It was assumed that the illumination of tracks (distribution of hit times) across each cell was uniform. A result of this assumption was that the XT maps were independent of the hit location within a chamber and therefore were calculated for each chamber. The online XT maps were generated using special muon data and were stored in the database. The offline XT maps were generated using K_{e3} decays. The conversion from a TDC count t to a drift distance $X(t)$ was

$$X(t) = d_{\text{cell}} \times \frac{\sum_{t'=t_0}^t N(t')}{\sum_{t'=t_0}^{t_m} N(t')}, \quad (4.1)$$

where $N(t')$ is the number of hits at TDC count t' , t_0 is the earliest TDC hit (largest number of TDC counts due to common stop) and t_m is the latest TDC hit (smallest number of TDC counts). The sum is in bins of 0.5 ns, which is the TDC least count.

Drift Chamber Alignment

There were three steps in aligning all of the drift chambers. First, the DC's were internally aligned with respect to each other. This left out an overall “corkscrew”

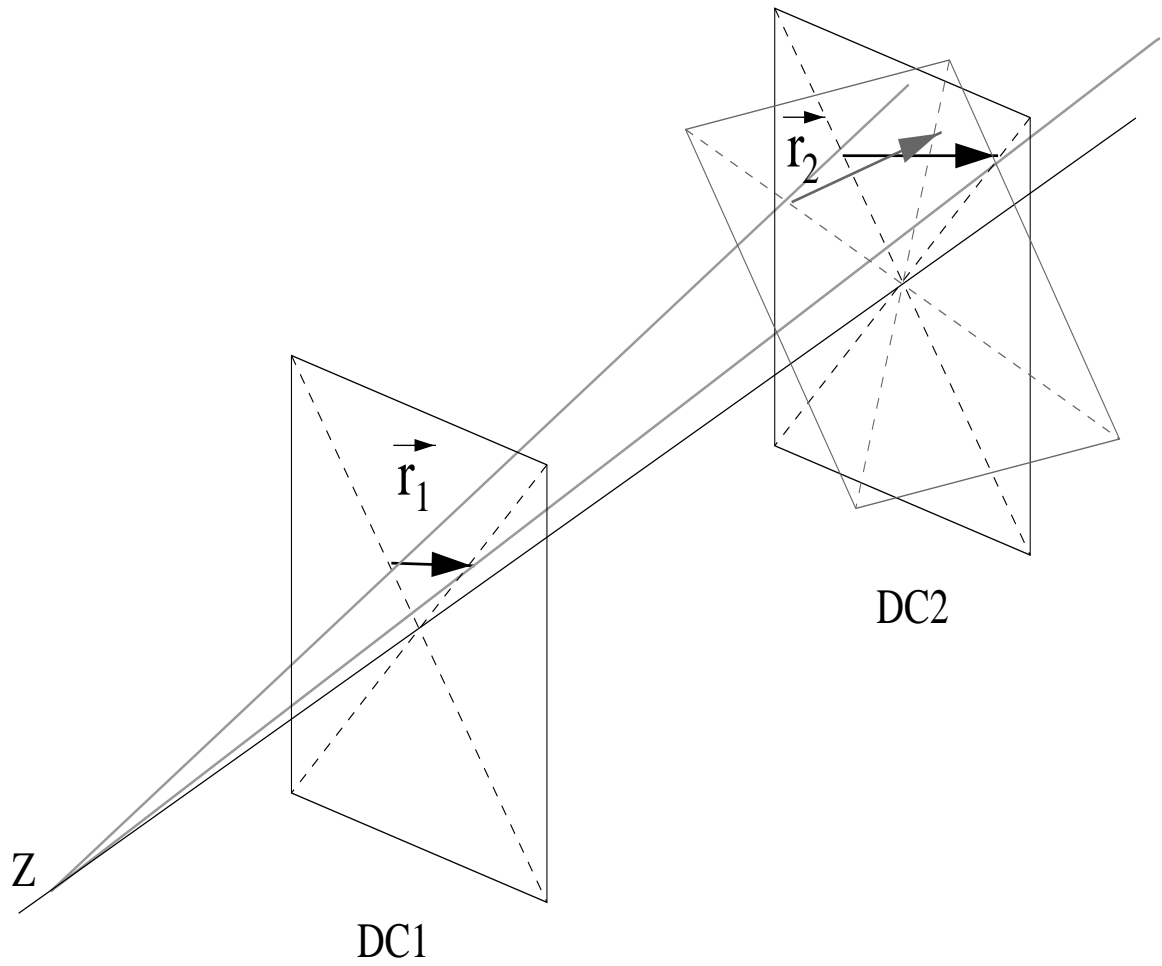


Figure 4.3: Illustration of a corkscrew rotation between DC1 and DC2.

rotation that needed to be removed. Finally, the DC's were aligned globally to other fixed elements of the detector.

The data used to internally align the DC's were special muon data with the analysis magnet turned off. Therefore, this data contained straight charged muon tracks. The technique was to assume two of the DC's were fixed and find the locations of the others. For example, a straight muon track was reconstructed using hits only from DC1 and DC4. The differences in the X and Y locations of this reconstructed line and the actual hits in DC2 and DC3 indicated the amount of alignment needed. The offsets in X and Y and rotations in the X-Y plane of the two DC's relative to the others were obtained.

This method of internally aligning the DC's resulted in a residual corkscrew rotation between the two DC assumed to be fixed in the scenario above. This is a rotation of the entire DC system. Again, K_{e3} decays were used to remove this rotation. Since the two tracks in these decays originated from a single vertex, they defined a plane. Therefore, a rotation would indicate an apparent separation of the tracks at the vertex. If a corkscrew rotation existed, then a rotation between DC1 and DC2 would appear as shown in figure 4.3. If we define $\vec{\mathbf{r}}_1$ to be the vector connecting the hits between the two tracks in DC1 and $\vec{\mathbf{r}}_2$ to be the vector connecting the hits between the two tracks in DC2, then if a corkscrew angle existed between DC1 and DC2

$$\vec{\mathbf{r}}_1 \times \vec{\mathbf{r}}_2 = |\vec{\mathbf{r}}_1||\vec{\mathbf{r}}_2| \sin \phi. \quad (4.2)$$

Of course, if a corkscrew angle did not exist between DC1 and DC2 then $\vec{\mathbf{r}}_1 \times \vec{\mathbf{r}}_2 = 0$. Plotting $\vec{\mathbf{r}}_1 \times \vec{\mathbf{r}}_2$ vs. $|\vec{\mathbf{r}}_1||\vec{\mathbf{r}}_2|$ for the K_{e3} events, the rotation angle ϕ was obtained. Since, this angle was uniform along Z, the angle as a function of Z yielded the correction factors for the other 2 DC's.

Finally, after the internal and corkscrew corrections were applied, the DC system was aligned to fixed external elements such as the target and the calorimeter. Reconstructed $K_L \rightarrow \pi^+ \pi^-$ decay were used to obtain these corrections. The total kaon momentum vector for these decays were projected to the target at $Z = 0$ meters to find the reconstructed X and Y projected locations at the target. Then, electron tracks from K_{e3} decays were used in a similar procedure as in the internal alignment of the DC's.

The electron track was projected to the face of the CsI. The difference in the track position (X and Y) at the CSI and the cluster energy center position (X and Y) were obtained as a function of the position in the CsI array. This yielded the offsets and rotations of the DC system with respect to the CsI. Finally the reconstruct target and CsI positions were used to correct the position of the DC's by iteratively making the corrections until the surveyed target and CsI positions were reconstructed.

4.2 Cluster Finding

4.2.1 Hardware and Software Clusters

In the clustering algorithm, there were two passes of clustering, a “hardware” pass using the HCC and a “software” threshold pass.

CsI crystals with the HCC bit set was one of the criteria for a hardware cluster. The cluster finding algorithm also searched for the local maximum in crystal energies by comparing crystal energies to neighboring crystal energies. The highest energy crystal of all its neighbors was defined as the cluster “seed”. The total energy of the cluster included energies from the crystals surrounding the seed with energy greater than the HCC threshold. If the seed was one of the small crystals, then the maximum cluster size was a 7×7 array of small crystals. If the seed was a large crystal, then the maximum cluster size was a 3×3 array of large crystals. If the seed was near a small/large crystal boundary, the cluster size was a 3×3 array of “large” crystals, where four small crystals could be grouped together as one “large”.

Software clusters were clusters whose seed crystal did not have the HCC bit on and had an energy greater than 100 MeV. The total cluster energy was required to be greater than 250 MeV.

The cluster positions were calculated using the ratios of seed block energy to neighboring block energies and then using a generated look-up table. The X positions were obtained from the sum of the column energies and the Y positions from the row energies. The cluster position resolutions were on the order of 1 mm.

Electromagnetic particles (e^\pm , γ) produced hardware clusters, whereas minimum

E/p Calibration for Runs 8282–8317

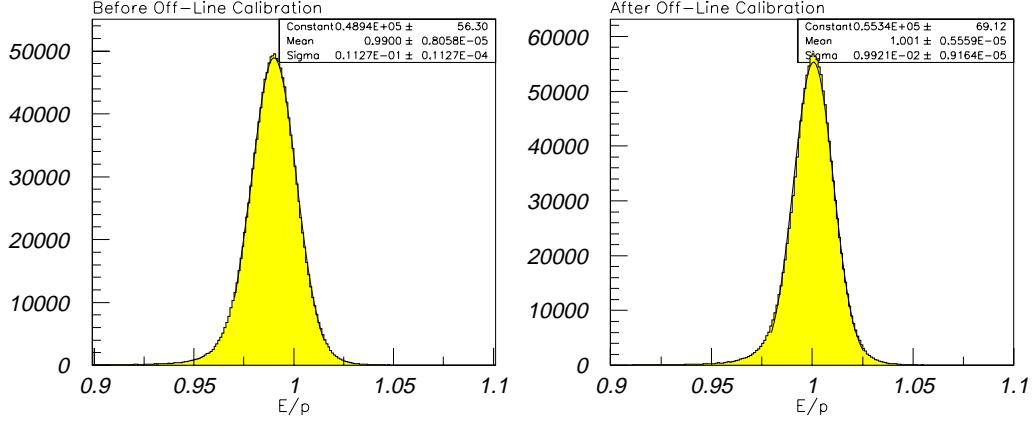


Figure 4.4: E/p distribution before and after the energy calibration. After the data was calibrated, the mean and the resolution were both greatly improved.

ionizing particles or MIP's (π^\pm, μ^\pm) mostly produced software clusters since their energies in the CsI were typically around 350 MeV.

4.2.2 Cluster Energy Calibration

The energy in each CsI crystal was measured using four digital PMT (DPMT) slices (or RF buckets), the first of which was the in-time slice. Roughly 95% of the energy in a cluster was contained in four slices. Correctly, determining the energy in each crystal required two different calibrations [70, 71].

First, the conversions between the DPMT counts and the PMT charge for each channel were needed to obtain the correct cluster energies. These conversions were calibrated using a laser light system that “scanned” the entire CsI array. A single laser source produced light pulses that were delivered to each crystal by means of optical fibers during calibration data taking periods. The responses of the DPMT's to the laser light source were measured and calibrated using many different size pulses.

Next, the charge to energy conversion was calibrated in each crystal using electrons from K_{e3} decays. The ratio of cluster energy to the measured track momentum, E/p,

of the electrons should average to unity, since electrons deposited most of their energy in the calorimeter. A departure from unity was due to miscalibrated crystals, so a set of calibration constants for the entire running period were generated to calibrate the crystal energies. The improvement in the energy measurement when using the energy calibration constants is illustrated in figure 4.4 [44].

4.2.3 Cluster Energy Corrections

After clusters were found, there were several corrections made to the energies [72, 73]. There were corrections made to the individual crystals (first five in list below) and corrections to the total energy (last item in list).

- *Overlap Correction:* This correction addressed the problem of having clusters that shared crystal energies. The energy in the overlapping crystal was divided between the clusters. The division was based on the total cluster energy and the position of the overlapping crystal within the cluster. GEANT [74] was used to estimate the corrections.
- *Neighbor Correction:* This correction was applied to high energy clusters that deposited a small fraction of their energy outside the 3×3 or 7×7 crystal array that defined the cluster. The energy of a neighboring cluster (non-overlapping) was adjusted, which may have otherwise measured a higher energy. This correction was also estimated using GEANT simulations.
- *Missing Block Correction:* This correction estimated the amount of unmeasured energy when a cluster was located near the edges of the CsI array. This was corrected by adding the amount of energy missing had there been more crystals at the edges. GEANT was used to estimate the amount of energy to add.
- *Sneaky Energy Correction:* This correction, similar to the *Missing Block Correction*, added energy to clusters near the beam hole edges. The *sneaky* energy is the component of the cluster energy that traversed the beam hole and deposited energy on the other side.

- *Threshold Correction:* This correction accounted for crystals part of a cluster whose energy was below the readout threshold. These corrections were estimated by data collected with no threshold and were a function of cluster energy and crystal position in the cluster.
- *Intra-Block Correction:* This correction addressed the non-uniform response across a crystal face. The energy correction depended on the position of the cluster on the seed crystal face (boundary vs. center). This effect was observed and corrections were estimated from data. This effect was not simulated in the Monte Carlo.

4.3 Decay Vertex Finding

In this analysis, there were four charged final decay particles. The decay vertex finding algorithm searched for four-track vertex candidates. At this stage in the event reconstruction process, at least two coexisting X tracks, at least two coexisting Y tracks and at least two HCC clusters were found. The next goal was to find the position of the decay vertex by matching X tracks to Y tracks to clusters.

The first step in finding a four-track vertex was to find all possible four-track intersections in the Y view, to within 2 mm. In this analysis, two X tracks were allowed to share a Y track, so a minimum of two intersecting Y tracks were allowed. The Z location of the intersection was required to be within the allowed decay region. For an event to be accepted, at least one Y intersection was required.

Next, all possible four X track (upstream segment) intersections were found to within 2 mm. The direction of the magnet bend determined the charge of each track and only two positive and two negative charged tracks were allowed. Again, the Z location of the intersection was required to be within the allowed decay region and at least one X intersection was required.

To match the newly-found X tracks to Y tracks, the CsI cluster information was needed. The projected locations of the X and Y track to the calorimeter face were matched to cluster locations. All possible X-Y track combinations were investigated and

the combination with the smallest track-cluster separation was considered the correct X-Y track match. In addition, the track-cluster separation was required to be less than 7 cm and tracks must point within the CsI array to ± 1.5 cm in both the X and Y directions. “Extra” clusters, or clusters with no track match, were candidates for photons. In this analysis, either all four tracks were required to have a cluster match or three tracks matched a cluster and only one of the tracks point to the beam hole at the face of the CsI.

For each four-track vertex candidate, various corrections were made to the tracks. The hit positions of the tracks were corrected for DC alignment and DC rotations about the Z axis. Fringe fields from the analysis magnet [75] also affected the hit positions in DC2 and DC3 and corrections were applied. After these corrections were applied, the X and Y views of each track were required to have at least one good-sod pair. The Z position of the four-track vertex was calculated as a weighted average of X-Y intersections, while the vertex X(Y) position was an average of the X(Y) positions of the tracks at the Z. Again, the vertex Z location was required to be within the allowed decay region. A χ^2 was calculated for the vertex position and one was calculated for the upstream and downstream offsets in X and Y at the center of the magnet. The figure of merit for the “best” vertex was a combination of these two χ^2 ’s and the number of good SOD’s found. In the end, the track-cluster information for all four tracks were obtained, such as the track trajectories and the momenta.

Chapter 5

Monte Carlo Simulation

The Monte Carlo (MC) simulation was an important tool in all KTeV analyses. The simulation consisted of kaon production and decay, particle tracing through the detector, simulation of the detector as well as the trigger and the level of accidental activity. Simulations of kaon decay samples were treated as similarly as possible to the data. The Monte Carlo was used to determine the acceptances, or reconstruction efficiencies, of different decay modes. It was also used to estimate the background level observed in a given decay mode. Comparisons were made between data and Monte Carlo to estimate the level of systematic error in a measurement.

5.1 Event Generation

5.1.1 Kaon Production

The production of a kaon was defined by the point on the target where it was produced, the momentum and direction of the kaon and the location in Z where the kaon decayed. Generated kaons in this analysis were produced with momentum ranging from 20-220 GeV/c and a Z position of the decay between 90-160 meters. The generated kaon momentum and K_L decay Z position are shown in figure 5.1. The location on the target where the kaon was generated was a function of the interaction depth of the target, the proton beam size and the targeting angle. The distribution of the kaon momentum and direction were generated from the Malensek parameterization [76]. The parameters were obtained from measurements of charged kaons, K^\pm , produced by 450 GeV protons striking a beryllium target. By valence and sea quark counting [54], we estimated the production probabilities, σ , for K^0 and \bar{K}^0 in terms of the production probabilities for

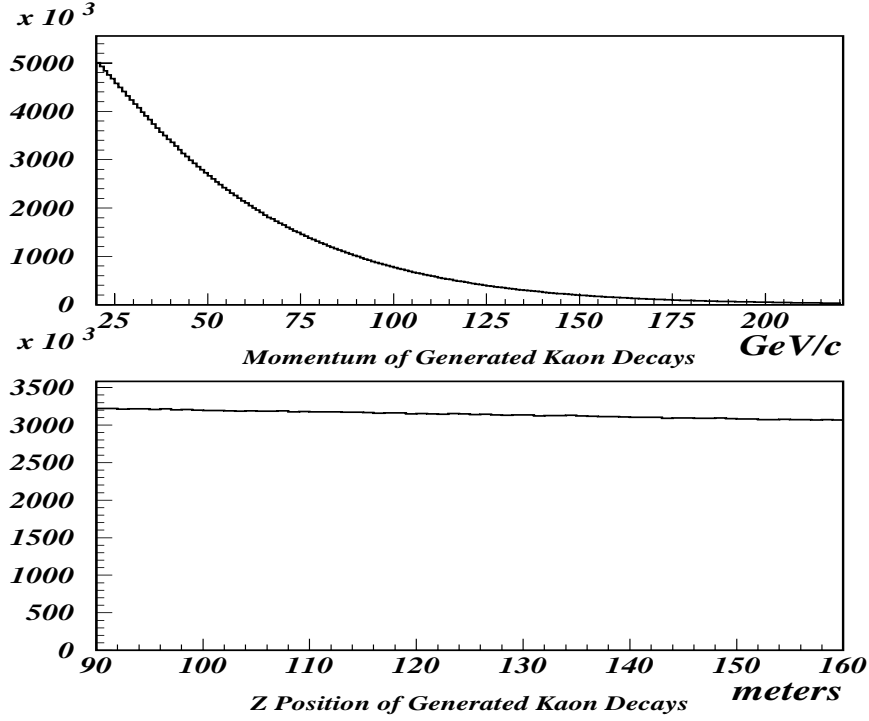


Figure 5.1: The Monte Carlo generated kaon momentum and decay Z position.

K^+ and K^- :

$$\begin{aligned}\sigma(K^0) &\sim \frac{\sigma(K^+) + \sigma(K^-)}{2} \\ \sigma(\bar{K}^0) &\sim \sigma(K^-)\end{aligned}\tag{5.1}$$

The momentum spectrum was further tuned to match the kaon momentum measured using $K_L \rightarrow \pi^+ \pi^-$ decays in KTeV. In the end, there was a relative mix of K^0 and \bar{K}^0 of 55% and 45%, respectively. A detailed discussion of kaon production in the KTeV MC is found in [45, 54].

5.1.2 Kaon Decay

Once the kaon was produced, the location of the kaon decay was selected. First, the kaon was propagated to the beginning of the decay region of $Z = 90$ meters. If the kaon path was traced going through one of the collimators then that kaon was rejected

and a new one was produced. After the Z position of the decay was determined, the preselected decay mode was generated.

5.2 Particle Tracing

The decay particles were boosted to the lab frame and traced along their direction of flight to each of the detectors. The particles traveled through the detector until they hit a photon veto or the calorimeter or they escaped the detector region. For photons and electrons, the tracing would stop if they hit a photon veto or the calorimeter. Particles were considered “lost” when they traveled outside the detector geometry. In this analysis, no generated signal particles were allowed to be lost.

Several particle interactions with detector material were included in the simulation. Charged particles between the vacuum region and the calorimeter could experience Coulomb multiple scattering according to Molière theory [77, 78]. Electrons were also allowed to emit bremsstrahlung photons according to the Bethe-Heitler cross-section [79]. Photons were also allowed to convert in the detector material. The conversion probability was $(1 - e^{-\frac{7}{9}(X/X_0)})$, where X/X_0 was the fraction of a radiation length the particle traveled through [46, 79, 80].

After all particle tracing, the detector element performance and digital response (digitization) were simulated using information saved during tracing. The behavior of charged particles in the magnetic field was also simulated.

5.3 Detector Simulation

5.3.1 Photon Vetos

The particle tracing was stopped when a photon or an electron was propagated to a photon veto (RC, SA, CIA). The response of a photon veto detector to electromagnetic particles was that they deposited all their energy in these detectors. The energies were smeared by a Gaussian distribution to simulate the detector resolution. The width of the distribution was determined by the photons in $K_L \rightarrow \pi^+\pi^-\pi^0$ data.

The response of the photon vetos to charged pions and muons was simulated as

MIP's. Again the energy deposited was smeared according to the energy resolutions from muon data [45].

5.3.2 Drift Chambers

The response of the planes of DC wires to charged particles was simulated. The drift distance to the closest wire to the charged particle was calculated just as in the data. The distance was smeared by a Gaussian to simulate the measured position resolution of the drift planes in data of $\sim 100\mu\text{m}$. These drift distances were converted to drift times using the calibration constants in the XT maps (see 4.1.3). The discrete ionization of the gas which modifies the drift distances was also simulated [41].

The DC inefficiencies were simulated by only recording the earliest hit within a time window of 235 ns. The inefficiencies were also simulated by randomly not recording hit information.

The details of the simulation of δ -ray production was also included and is discussed in [45, 47].

5.3.3 Calorimeter

The simulation of the CsI calorimeter consisted of the simulation of cluster energies and of the readout system [81, 45]. The generation of cluster energies was highly dependent on the type of particle that came in contact with the calorimeter. Photons, electrons and charged pions whose trajectories were propagated to the calorimeter were stopped there and their energy showers were simulated. Muons, on the other hand, deposited a MIP energy and were allowed to pass through the calorimeter. The energy deposition of a muon was restricted to a single crystal. The details of the muon energy simulation is described in [41].

The electron and photon shower simulations were conducted slightly differently than the pion shower simulation since the electron and photon showers were fully contained in the CsI [81, 45, 49, 41]. The electron/photon shower simulations were selected randomly from electromagnetic shower libraries generated by GEANT. Inputs to the

shower libraries were the transverse position of the shower mean ¹ and the energy. Before choosing a library, the energies were smeared by a Gaussian to match energy resolutions seen in the data. The showers were generated for six energy slices of 2, 4, 8, 16, 32 and 64 GeV. The energy was then divided into 13×13 small crystal square regions (a large crystal was treated as four small crystals). The shower information was also sliced into 25 equal regions in Z (depth) due to the observed non-uniform behavior of the CsI. The shower was also indexed by position bins of 50×50 across the face of a crystal to locate the shower center. The position bins were designed to best simulate the position resolution. There was also a “sneaky energy” library that added energy to particles traversing the beam holes.

A charge pion could deposit only a MIP of energy or it could shower. The charged pion shower library was also generated using GEANT [49]. The shower simulation for pions was similar to the one described above for electrons and photons with some differences. The energy was divided into 12 bins ranging from 2-64 GeV. The shower was also indexed by position bins of 10×10 across the face of a crystal to locate the shower center.

Finally, the total light deposited in each crystal was determined. The time structure of the PMT pulses and the digitization of the DPMT’s were simulated with smearing to match the photon statistics effects seen in data (see 2.2.3). The conversion to charge was determined using lookup tables obtained from data.

5.4 Accidental Activity

It was important to include accidental activity in the event generation since it was possible to lead to biases in event reconstruction. Accidental activity could corrupt tracks or increase cluster energy so it was necessary to include it in the Monte Carlo.

Accidental events from the accidental trigger (see 2.2.8) collected during data taking were overlaid on top of generated events after the generation and tracing stages. Accidental overlays were added before threshold and trigger evaluations. Accidental energy

¹The shower mean position was a function of energy and was slightly different for photons and electrons.

was added to a simulated event, accidental DC hit information was merged with that of the simulated event and the trigger information was also combined. Accidental overlays were a function of run number and also supplied a spill number to the generated event.

Accidental overlays also provided a method of determining the level of systematic uncertainty in a measurement due to accidental activity. Studying possible differences in the detector acceptances from MC samples generated with and without accidental overlays could yield in a source of systematic uncertainty.

5.5 Trigger Simulation

The Monte Carlo simulates the behavior of all the trigger elements. The pattern of trigger sources and lookup tables were identical to the ones during data taking conditions. The trigger definition file was the same as the one used online (see 3.1.3).

Most of the level 1 trigger elements were simulated simply as detector energy thresholds that included generated and accidental energies. The DCOR trigger sources were simulated using the DC hit information. The level 1 photon veto sources were evaluated immediately after particle tracing, rejecting events to reduce CPU time. The level 1 trigger was fully evaluated after all the detector simulations were complete.

The level 2 elements were simulated with the exact algorithms used during data taking. The level 3 software was exactly the same as the online software (see 3.1.4), as were the calibration constants.

5.6 Individual Decay Generators

To measure the $K_L \rightarrow e^+e^-e^+e^-$ branching ratio, the events were normalized to another kaon decay mode with a well measured branching ratio. This normalization decay mode should also have similar final state particles as the signal decay mode to minimize systematic biases. The decay mode used that fits this description is the decay mode $K_L \rightarrow \pi^0\pi_D^0\pi_D^0$ ². The decay generators of these two decay modes are described in this section.

²The π_D^0 refers to the Dalitz decay $\pi^0 \rightarrow e^+e^-\gamma$.

5.6.1 Monte Carlo Simulation of $K_L \rightarrow e^+e^-e^+e^-$

The $K_L \rightarrow e^+e^-e^+e^-$ decay was simulated using the matrix element of Miyazaki and Takasugi [24] as was described in 1.4.1. This model assumes a point-like structure of the K_L , however the decay generator was constructed to include any form factor parameterization, such as the ones described in 1.6.

Since an exact QED calculation of the radiative corrections to $K_L \rightarrow e^+e^-e^+e^-$ does not exist, approximate corrections were implemented. Until recently, the PHOTOS package [82] was the only simulation we had for radiative corrections for the signal mode. PHOTOS uses pure QED radiative corrections with a single photon in the leading-logarithmic approximation. There also exists a simulation package [83] in which the radiative corrections to $K_L \rightarrow e^+e^-e^+e^-$ were implemented numerically in our Monte Carlo. The corrections contained the radiative double Dalitz decay, $K_L \rightarrow e^+e^-e^+e^-\gamma$, which included radiative diagrams of the order α^3 , compared to the tree level process of order α^2 . There were also virtual corrections that could be implemented to the tree-level process but were not used in this analysis since not all virtual contributions existed in the simulation. These virtual corrections included higher order loop graphs that occur at order α^4 . Another known difference between the two simulations in the signal Monte Carlo was the value of the photon energy cutoff. The PHOTOS Monte Carlo is capable of a minimum cutoff of 1 MeV and this was the cutoff used. The minimum cutoff in the KTeV radiation simulation used for the four-electron final state was 4 keV. Effects of radiative corrections were studied using these two simulations, as well as with no implementation of the radiative corrections.

5.6.2 Monte Carlo Simulation of $K_L \rightarrow \pi^0\pi_D^0\pi_D^0$

The decay generator of $K_L \rightarrow \pi^0\pi_D^0\pi_D^0$ consisted of two parts. First, the decay $K_L \rightarrow \pi^0\pi^0\pi^0$ was generated and then the three π^0 's were allowed to decay, one $\pi^0 \rightarrow \gamma\gamma$ and two $\pi^0 \rightarrow e^+e^-\gamma$.

The decay $K_L \rightarrow \pi^0\pi^0\pi^0$ was simulated based on a pure phase space distribution, with no structure in the decay matrix element. The decay $\pi^0 \rightarrow \gamma\gamma$ was also simulated

assuming uniform phase space.

The π^0 Dalitz decay was simulated using the matrix element calculation of Kroll and Wada [25]. The simulation included a form factor of the form $1 + a \cdot x$, where the value of the parameter a used was the measured value of 0.032 in the PDG [10]. Radiative corrections to the Dalitz decay were also implemented based on the calculations of Mikaelian and Smith [84]. The bremsstrahlung correction included a cutoff of $m_{\gamma\gamma} > 1$ MeV/ c^2 . We again studied systematic effects of radiative corrections using simulations with and without radiative corrections.

Chapter 6

Signal Extraction

6.1 Event Signature and Backgrounds to $K_L \rightarrow e^+e^-e^+e^-$

The event signature of a $K_L \rightarrow e^+e^-e^+e^-$ event was a simple one. We searched for two positively charged tracks and two negatively charged tracks all originating from one vertex. Each track was required to have a cluster associated with it that deposited nearly all of its energy in the CsI, defining it as an electron or a positron.

There were other decay modes, however, that had a similar event signature and could have been mistaken as a signal event. There were two categories of background events to $K_L \rightarrow e^+e^-e^+e^-$ in this experiment. The first came from the decays $K_L \rightarrow e^+e^-\gamma$ and $K_L \rightarrow \gamma\gamma$, with the photon(s) converting in the material of the detector (e.g., the vacuum window, the air gap and upstream of DC1). The other possible source of background was the decay $K_L \rightarrow \pi e \nu \gamma$ (radiative K_{e3}) with an internal or external photon conversion. These backgrounds are discussed in detail in section 6.4.

6.2 Selecting Candidate $K_L \rightarrow e^+e^-e^+e^-$ Events

The winter analysis runs used ranged from run number 8245-8910 and the summer analysis runs from 10463-10970 (see figure 6.1).

The first set of selection criteria, or cuts, were for particle identification. We required four charged tracks that reconstructed a good vertex and two y track pairs were allowed to share hits (see discussion in 4.3). If one of the four tracks pointed down the beam hole at the CsI, the event was kept (there was no cluster associated with this track). These four tracks were required to be two electrons and two positrons. Therefore, the E/P , the ratio of the cluster energy to the track momentum, of each of the four tracks

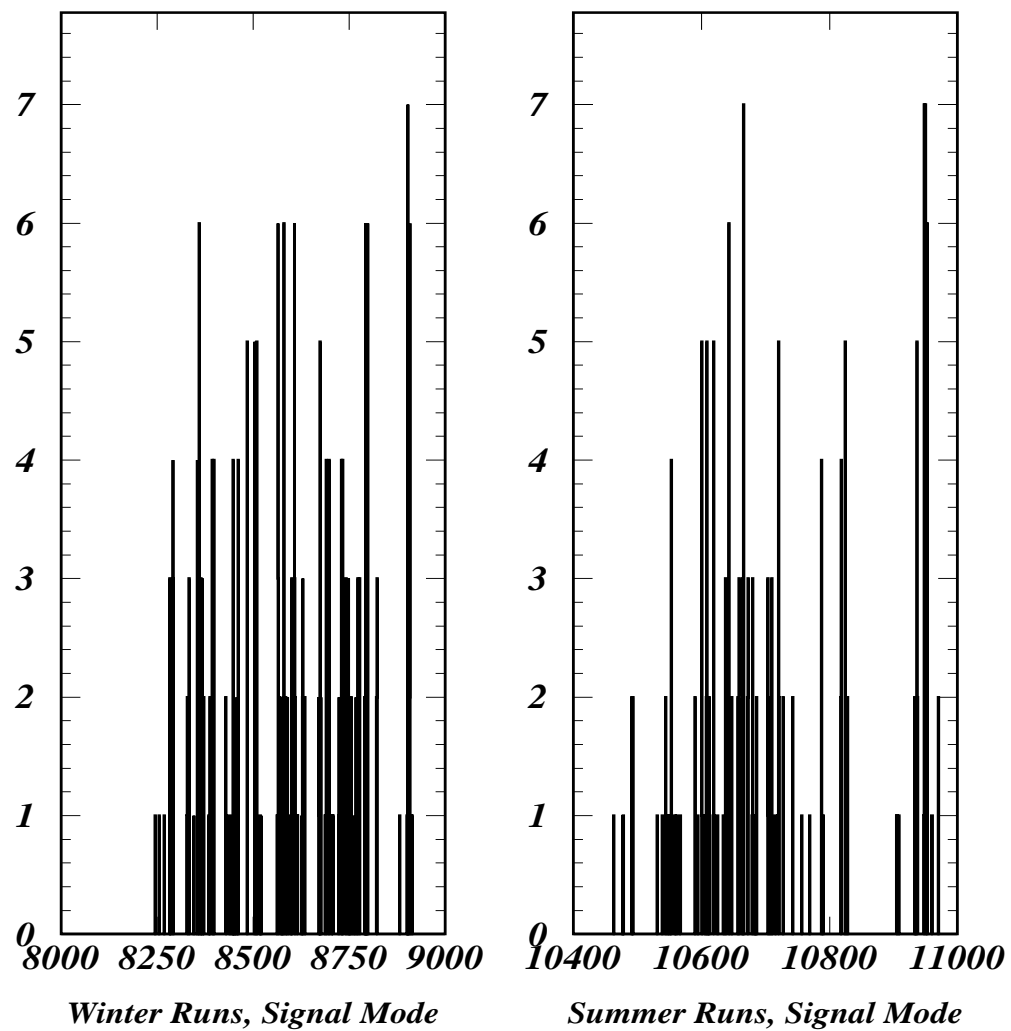


Figure 6.1: Events vs. Run Number for signal mode events for both winter and summer data taking conditions.

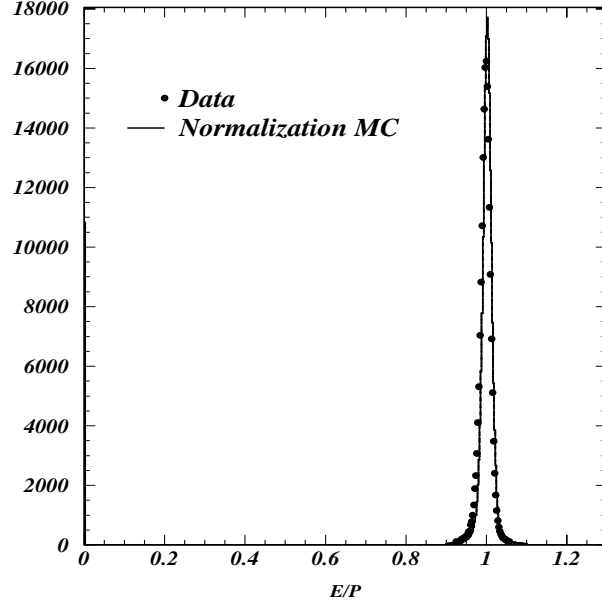


Figure 6.2: E/P distribution for normalization events compared to Monte Carlo. The spike at zero are the events with one track down the beam hole at the CsI.

was required to be within 0.9 and 1.1. The E/P distribution for normalization events (see chapter 7) compared to Monte Carlo is shown in figure 6.2, for a higher statistics comparison. Also, the sum of the charges of the four tracks was required to be zero.

The next set of cuts were made to ensure that the events fired the trigger; these are also referred to as trigger verification cuts. An energy cut of 2 GeV was made on all used clusters, including the ones that had a track pointing to it. The cluster energy distribution is shown in figure 6.3 for normalization events compared to Monte Carlo. Selection criteria on the maximum photon veto energy were also made. The maximum RC energy and the maximum SCIA energy was required to be less than 0.5 GeV. The maximum energy in the CA was required to be less than 5.0 GeV. The maximum photon veto energy distributions are shown in figure 6.4 for normalization events compared to Monte Carlo.

The next set of cuts were made to ensure the data quality and to reduce the level of background events. The Z position of the charged vertex was required to be within

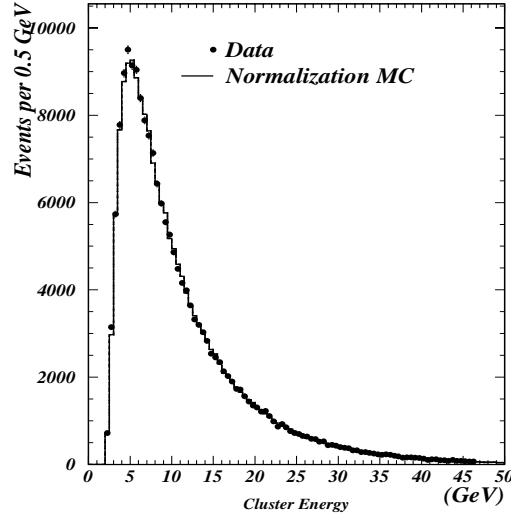


Figure 6.3: Cluster energy distribution for normalization events compared to Monte Carlo.

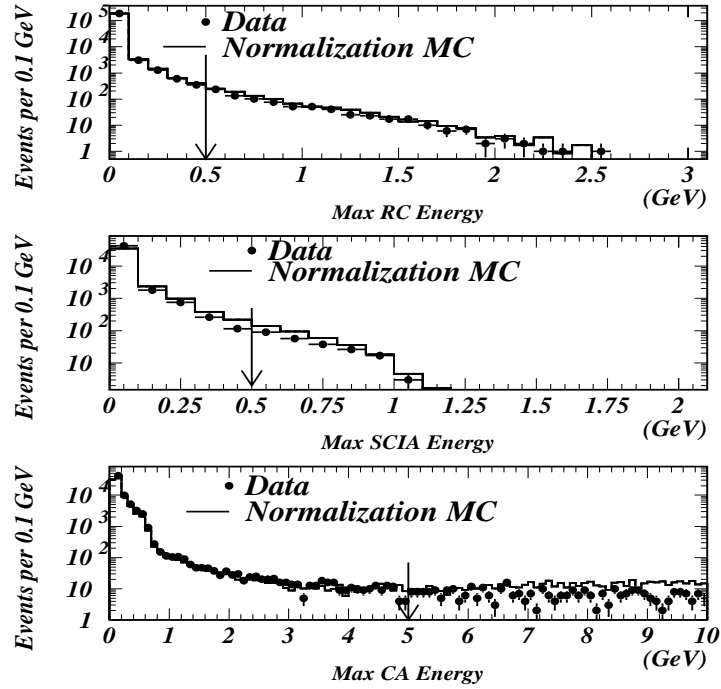


Figure 6.4: Maximum Photon Veto energy distributions for normalization events compared to Monte Carlo. The arrows indicate the position of the cut.

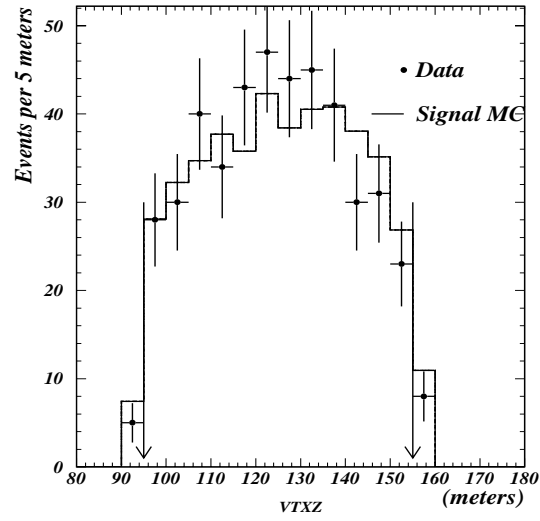


Figure 6.5: Vertex Z distribution for signal events compared to Monte Carlo. The arrows indicate the position of the cut.

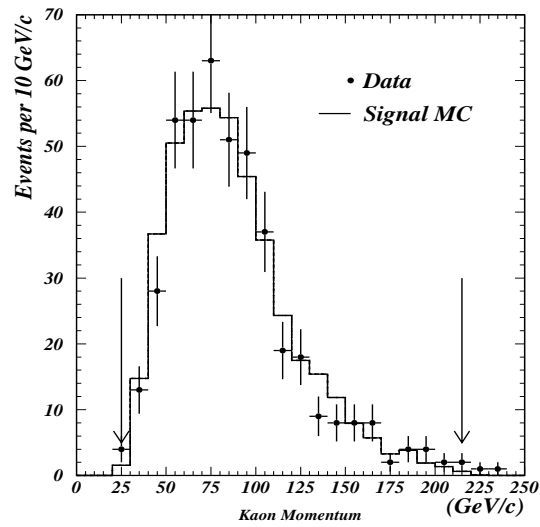


Figure 6.6: Kaon momentum distribution for signal events compared to Monte Carlo. The arrows indicate the position of the cut.

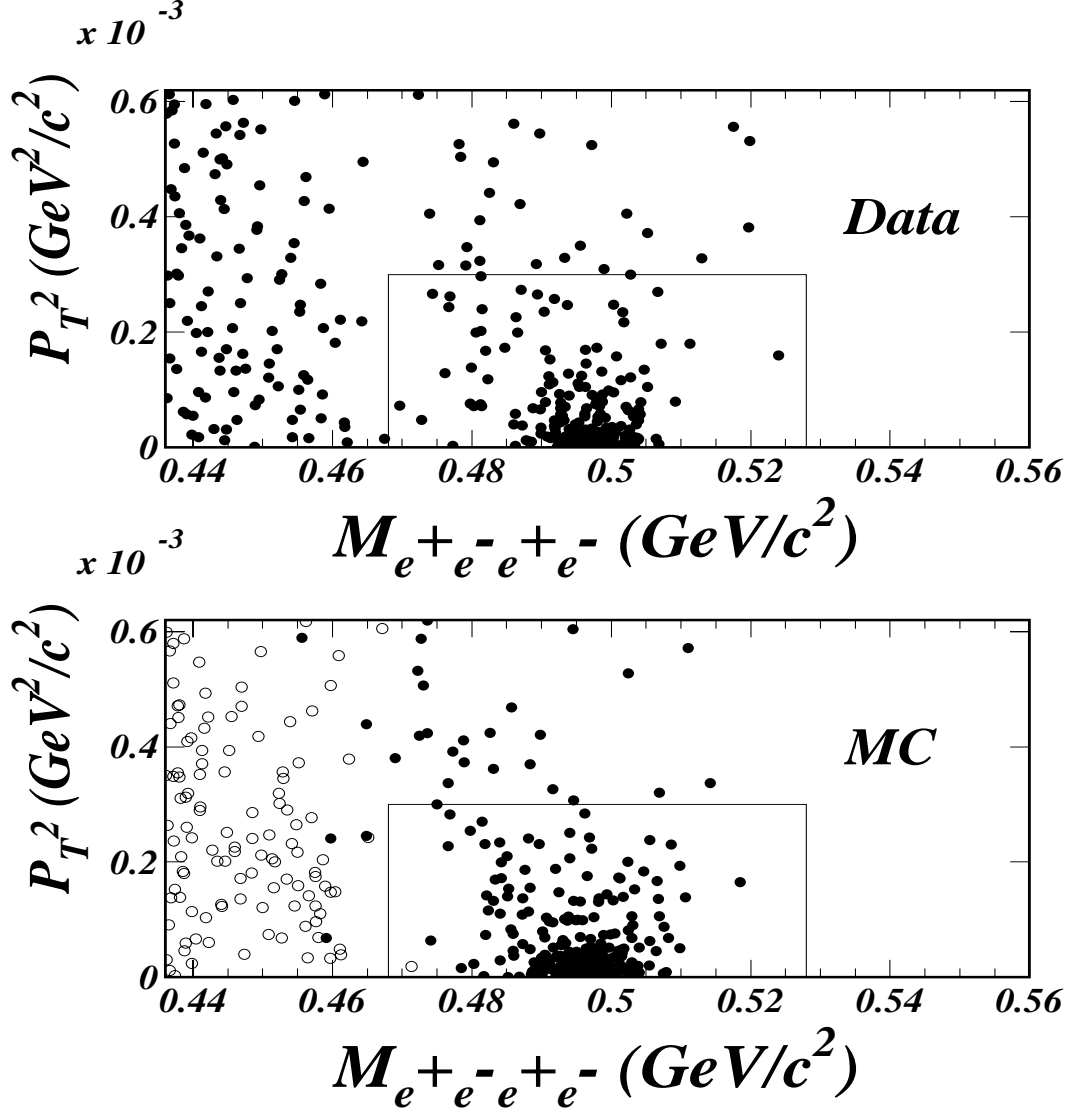


Figure 6.7: Top: The distribution of P_T^2 vs. $M_{e^+e^-e^+e^-}$ for candidate $K_L \rightarrow e^+e^-e^+e^-$ events. There are 441 events in the signal region defined by the box. Bottom: The distribution of P_T^2 vs. $M_{e^+e^-e^+e^-}$ for reconstructed Monte Carlo simulated events, scaled to the data statistics. The filled circles represent the signal Monte Carlo and the open circles represent the $K_L \rightarrow \pi e \nu e e$ Monte Carlo. The box defines the signal region with an efficiency of 90%.

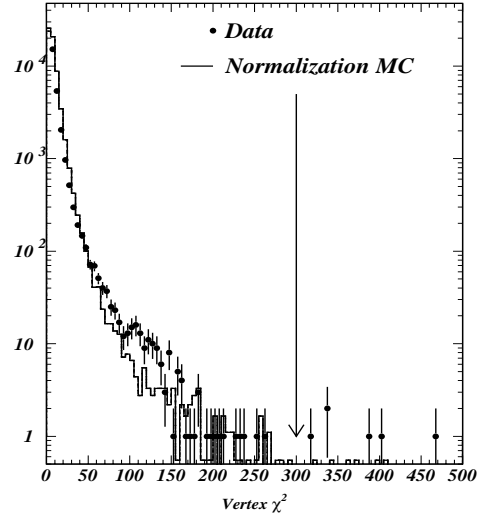


Figure 6.8: Vertex χ^2 distribution for normalization events compared to Monte Carlo. The arrow indicates the position of the cut. In this variable, the discrepancy between data and Monte Carlo is not understood but it is not significant (note the log scale!).

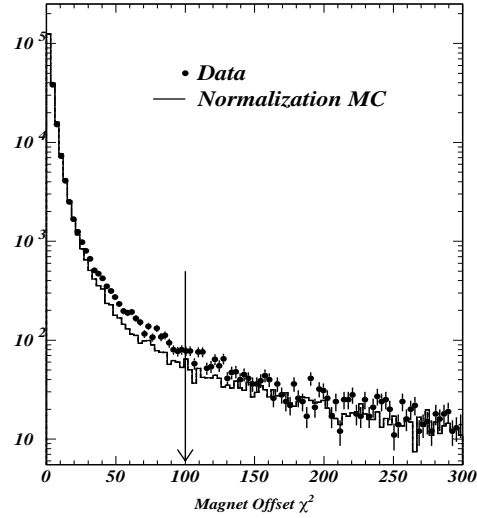


Figure 6.9: Magnet offset χ^2 distribution for normalization events compared to Monte Carlo. The arrow indicates the position of the cut. In this variable, the discrepancy between data and Monte Carlo is not understood but it is not significant (note the log scale!).

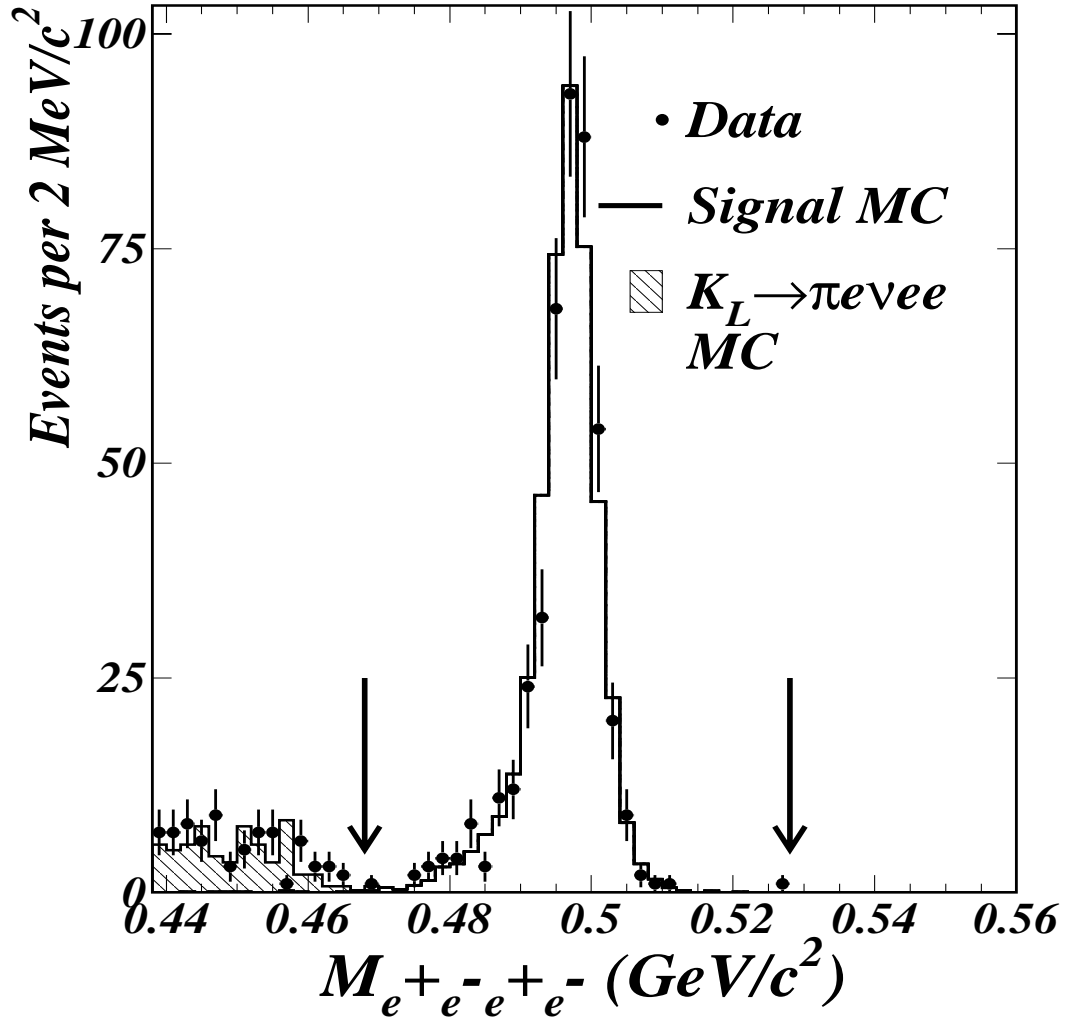


Figure 6.10: The $M_{e^+e^-e^+e^-}$ distribution after all cuts except the invariant mass cut. The dots represent the data and the histogram represents the Monte Carlo simulation. The arrows indicate an intentionally wide mass window chosen to retain the low-side radiative tail visible in the data and the Monte Carlo. The decay $K_L \rightarrow \pi e \nu ee$ is seen in the lower mass region.

KTeV Event Display

Run Number: 8333
 Spill Number: 34
 Event Number: 5087709
 Trigger Mask: d
 All Slices

Track and Cluster Info
 HCC cluster count: 4

ID	Xcsi	Ycsi	P or E
T 1:	-0.1702	0.2919	-7.11
C 3:	-0.1665	0.3003	7.32
T 2:	-0.0059	-0.1450	+24.74
C 4:	-0.0079	-0.1402	25.41
T 3:	0.4956	-0.2177	-8.17
C 2:	0.4966	-0.2188	8.29
T 4:	0.6170	0.2017	+6.82
C 1:	0.6215	0.2014	6.85

Vertex: 4 tracks

X	Y	Z
0.1070	-0.0287	137.668

 Chisq=59.87 Pt2v=0.000014

- - Cluster
- - Track
- - 10.00 GeV
- - 1.00 GeV
- - 0.10 GeV
- - 0.01 GeV

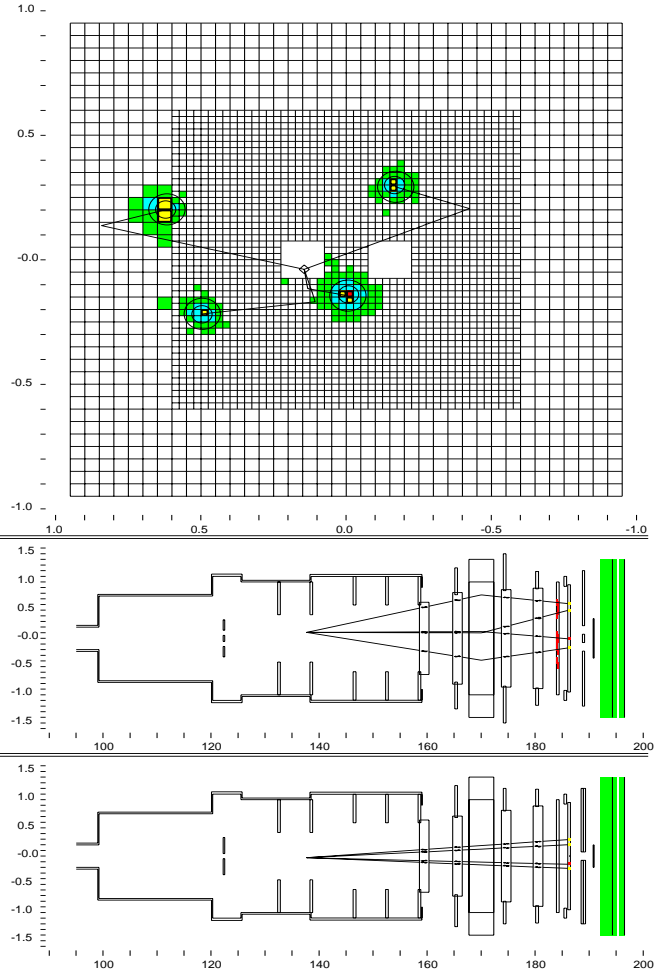


Figure 6.11: Event display of a $K_L \rightarrow e^+e^-e^+e^-$ data event. The top figure shows the face view of the CsI calorimeter. The bottom two figures show the X and Y views of the KTeV detector. The energy, momenta and positions of the clusters and tracks are printed in the top left corner. A typical $K_L \rightarrow e^+e^-e^+e^-$ event has four tracks pointing to four clusters with a good vertex. Note that the vertex position is inside the area of one of the beams.

the kinematic region of $95 - 155\text{m}$. The total momentum of the kaon in the lab was constrained to be between $25 - 215\text{GeV}/c^2$. These distributions are shown in figures 6.5 and 6.6¹. The transverse momentum squared², P_T^2 , of the kaon was required to be less than $300(\text{MeV}/c)^2$. Figure 6.7 shows the distribution of P_T^2 vs. $M_{e^+e^-e^+e^-}$ for data and for reconstructed Monte Carlo events with all cuts but the invariant mass and P_T^2 cuts (see table 6.1). The box defines the signal region, keeping about 90% of the events. The $K_L \rightarrow \pi e \nu e e$ Monte Carlo is also shown and is described later in section 6.4. The reconstructed vertex χ^2 was less than 300 and the χ^2 of the offset between track segments projected to the magnet bend plane was required to be less than 100 for all tracks. The vertex χ^2 and magnet offset χ^2 distributions for normalization events compared to Monte Carlo are shown in figures 6.8 and 6.9, for a higher statistics comparison. A cut on the minimum track separation at DC1 was required to be $> 1\text{ mm}$ to get rid of background described later. Finally, the four body invariant mass, $M_{e^+e^-e^+e^-}$, was constrained to be within 30MeV of the neutral kaon mass. Figure 6.10 shows the $M_{e^+e^-e^+e^-}$ distribution after all cuts except the invariant mass cut.

To summarize, a list of all the cuts is shown in table 6.1. The treatment of backgrounds is described in 6.4. In addition, an event display of a typical $K_L \rightarrow e^+e^-e^+e^-$ event is shown in figure 6.11.

6.3 Signal Events

There were 441 events in the signal region after all the cuts described in the previous section. We summarize the total number of events observed in the $K_L \rightarrow e^+e^-e^+e^-$ decay in table 6.2.

¹All $K_L \rightarrow e^+e^-e^+e^-$ Monte Carlo in this chapter includes the KTeV implemented radiative corrections and no form factor, unless otherwise noted.

²The square of the component of the total momentum of the daughter particles ($e^+e^-e^+e^-$) transverse to the kaon line of flight.

Table 6.1: $K_L \rightarrow e^+e^-e^+e^-$ Selection Cuts

List of signal selection cuts	Cut value
Number of tracks that make a vertex	4
Minimum cluster energy	2 GeV
E/P	0.9 - 1.1
Number of electrons (E/P above)	4
Number of e^+e^-	$2e^+, 2e^-$
Max RC, SCIA energy	0.5 GeV
Max CA energy	5.0 GeV
VTXZ	95 – 155m
$P_{e^+e^-e^+e^-}$	$25 - 215 \text{ GeV}/c^2$
$P_T^2_{e^+e^-e^+e^-}$	$< 300 (\text{MeV}/c)^2$
vertex χ^2	< 300
offmag χ^2	< 100
Minimum track separation at DC1	$> 1\text{mm}$
$M_{e^+e^-e^+e^-}$	468 – 528MeV

Table 6.2: Total Number of Signal Mode Events

Total $K_L \rightarrow e^+e^-e^+e^-$ candidate events	441
Winter events	257
Summer events	184
No beam hole events	377
Beam hole events only	64

6.4 Background Estimation in $K_L \rightarrow e^+e^-e^+e^-$

There were two important backgrounds to the decay $K_L \rightarrow e^+e^-e^+e^-$ in this analysis. The first we considered comes from the decays $K_L \rightarrow e^+e^-\gamma$ and $K_L \rightarrow \gamma\gamma$, with the photon(s) converting in the material of the detector (eg, the vacuum window, the air gap and upstream of DC1).

Another possible source of background came from $K_L \rightarrow \pi e \nu \gamma$ (radiative K_{e3}) with an internal or external photon conversion. If the pion was the particle that traveled down the beam hole at the calorimeter then this could have “faked” a $K_L \rightarrow e^+e^-e^+e^-$ event. Therefore, this background was only considered for the beam hole events, events

Table 6.3: $K_L \rightarrow e^+e^-e^+e^-$ Conversion Background Estimate

Type of background	bkgr before conversion cut	bkgr after conversion cut
$K_L \rightarrow e^+e^-\gamma_c$ (single conversion)	$(28 \pm 2)\%$	$(0.84 \pm 0.07)\%$
$K_L \rightarrow \gamma_c\gamma_c$ (double conversion)	$(1.2 \pm 0.1)\%$	$(0.0013 \pm 0.0006)\%$

where one track has gone down the beam hole at the CsI.

6.4.1 Photon Conversions

As mentioned above, a source of background to $K_L \rightarrow e^+e^-e^+e^-$ came from $K_L \rightarrow e^+e^-\gamma$ and $K_L \rightarrow \gamma\gamma$ when their daughter photons interacted with material in the detector. The probability for such an occurrence was measured for our detector and is $(2.74 \pm 0.11) \times 10^{-3}$. The details can be found in [85].

When a photon externally converts to an e^+e^- pair the opening angle of the e^+e^- pair is very small. We used this fact to remove the $K_L \rightarrow e^+e^-\gamma$ and $K_L \rightarrow \gamma\gamma$ backgrounds. By cutting out events that have a minimum track separation at DC1 of much less than 1mm (the minimum distance two tracks can be separated to be in the same drift cell) we significantly reduced this background. Since the tracking algorithm allowed tracks to share y track pairs, we essentially threw out events that had tracks closer than the resolution of our detector and the track separation variable was set to zero.

The amount of conversion background in the data before and after the minimum track separation cut from single and double conversions for $K_L \rightarrow e^+e^-e^+e^-$ is summarized in table 6.3. We estimated the total number of background events from this source is 3.7 ± 0.3 events. These numbers were obtained as follows:

$$N_{K_L \rightarrow e^+e^-\gamma_c} = \#K_L \text{decays} \times B_{K_L \rightarrow e^+e^-\gamma} \times P_{\text{conversion}} \times \text{Acceptance} \quad (6.1)$$

(for single conversions)

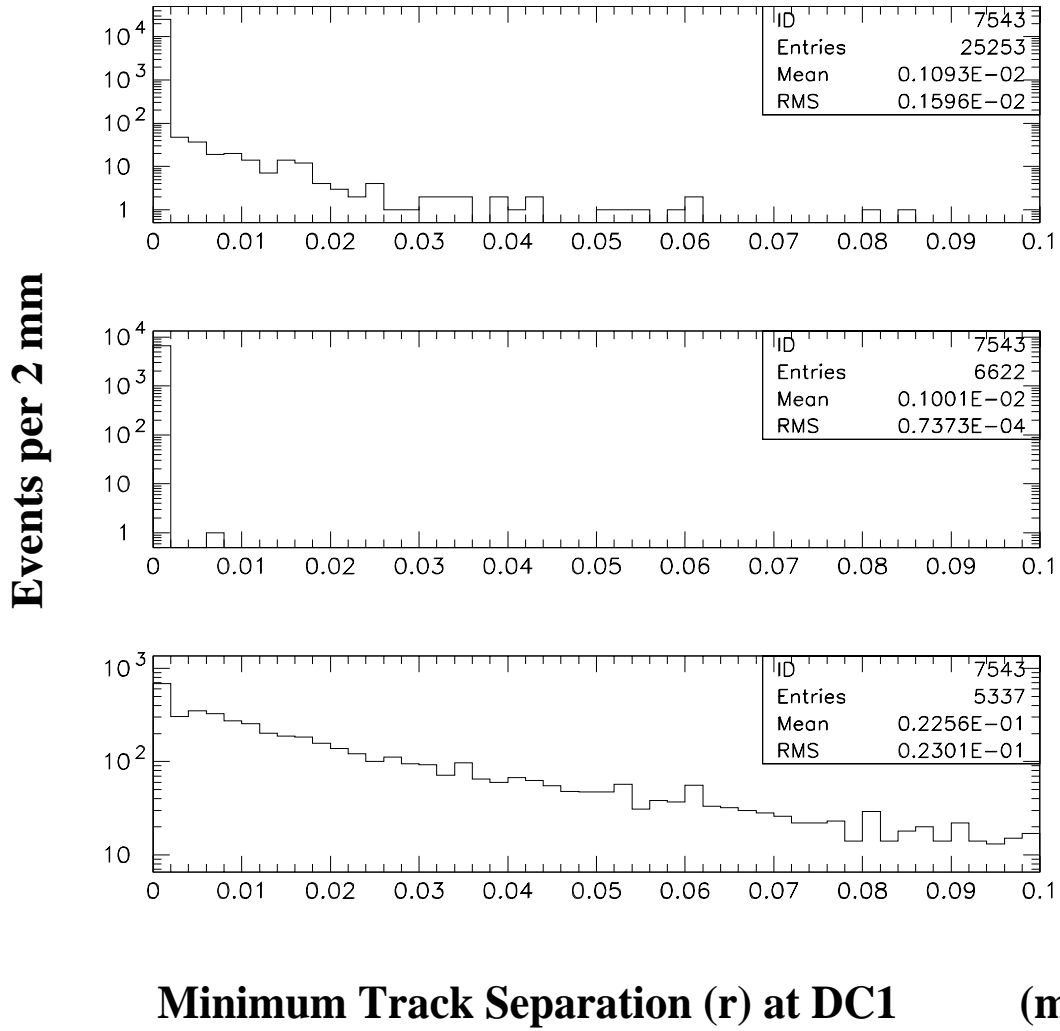


Figure 6.12: The top plot shows the distribution of the minimum track separation at DC1 for $K_L \rightarrow e^+e^-\gamma_c$ MC. The middle plot show this distribution for $K_L \rightarrow \gamma_c\gamma_c$ MC. The bottom is signal MC. These are not normalized to the data.

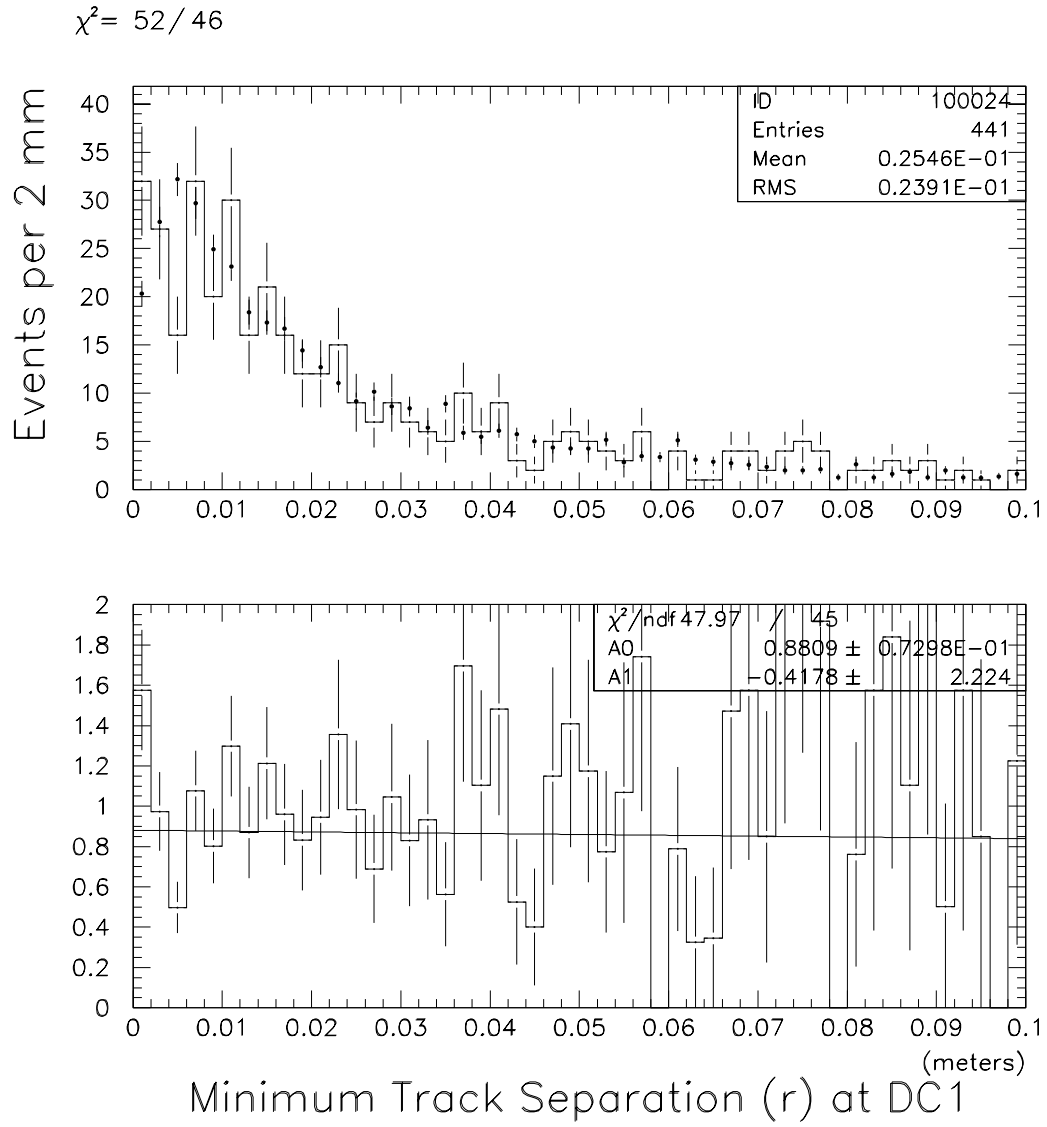


Figure 6.13: Distribution of the minimum track separation at DC1. The histogram is the $K_L \rightarrow e^+e^-e^+e^-$ data and the dots are the MC after the conversion cut has been made. The bottom plot is data over MC.

$$N_{K_L \rightarrow \gamma_e \gamma_e} = \#K_L \text{ decays} \times B_{K_L \rightarrow \gamma \gamma} \times P_{\text{conversion}}^2 \times \text{Acceptance} \quad (6.2)$$

(for double conversions)

These equations give the number of expected conversion events in the data. The calculation of the number K_L decays, or the total number of kaon decays, is discussed further in section 7.4. From Monte Carlo studies signal loss due to the conversion cut was $(8.7 \pm 0.2)\%$.

In figure 6.12, the top plot shows the distribution of the track separation at DC1 for $K_L \rightarrow e^+ e^- \gamma_e$ MC (we forced the photon to externally convert at the vacuum window). The middle plot show this distribution for $K_L \rightarrow \gamma_e \gamma_e$ MC and the bottom plot is signal MC. In figure 6.13 the histogram represents the $K_L \rightarrow e^+ e^- e^+ e^-$ data and the dots represent the MC after the conversion cut was made. The bottom plot is data over MC and illustrates that the data and MC agree over the range shown.

6.4.2 Background from $K_L \rightarrow \pi e \nu e e$

This background was considered only for events where one track traveled down the beam hole at the CsI. If the pion was the particle down the beam hole at the calorimeter then this could have been mistaken for a $K_L \rightarrow e^+ e^- e^+ e^-$ event. The reconstructed K_L invariant mass with the pion misidentified as an electron should be smaller than $478 \text{ MeV}/c^2$; accidental activity and misreconstructions could move this decay into our signal region. Since the branching ratio for $K_L \rightarrow \pi e \nu e e$ has not been measured we studied the background from $K_L \rightarrow \pi e \nu e e$ by using the parent decay $K_L \rightarrow \pi e \nu \gamma$, whose branching ratio has been measured [86]. We simulated $K_L \rightarrow \pi e \nu e e$ by converting the γ from $K_L \rightarrow \pi e \nu \gamma$ at the vertex at the generation stage. Also, since the branching ratio for $K_L \rightarrow \pi e \nu \gamma$ was measured only for $E_\gamma > 30 \text{ MeV}$ and $\theta_{e-\gamma} > 20^\circ$, we generated $K_L \rightarrow \pi e \nu \gamma$ events for the full E_γ and $\theta_{e-\gamma}$ range to obtain the scale factor to scale the measured $K_L \rightarrow \pi e \nu \gamma$ branching ratio. We then estimated:

$$B(K_L \rightarrow \pi e \nu e e) = B(K_L \rightarrow \pi e \nu \gamma) \times \text{scale} \times \alpha_{\text{QED}} \quad (6.3)$$

Figure 6.7 shows the $K_L \rightarrow \pi e \nu e e$ background as a band in P_T^2 vs. $M_{e^+ e^- e^+ e^-}$ and this background is seen in the lower mass region in figure 6.10. These figures contain

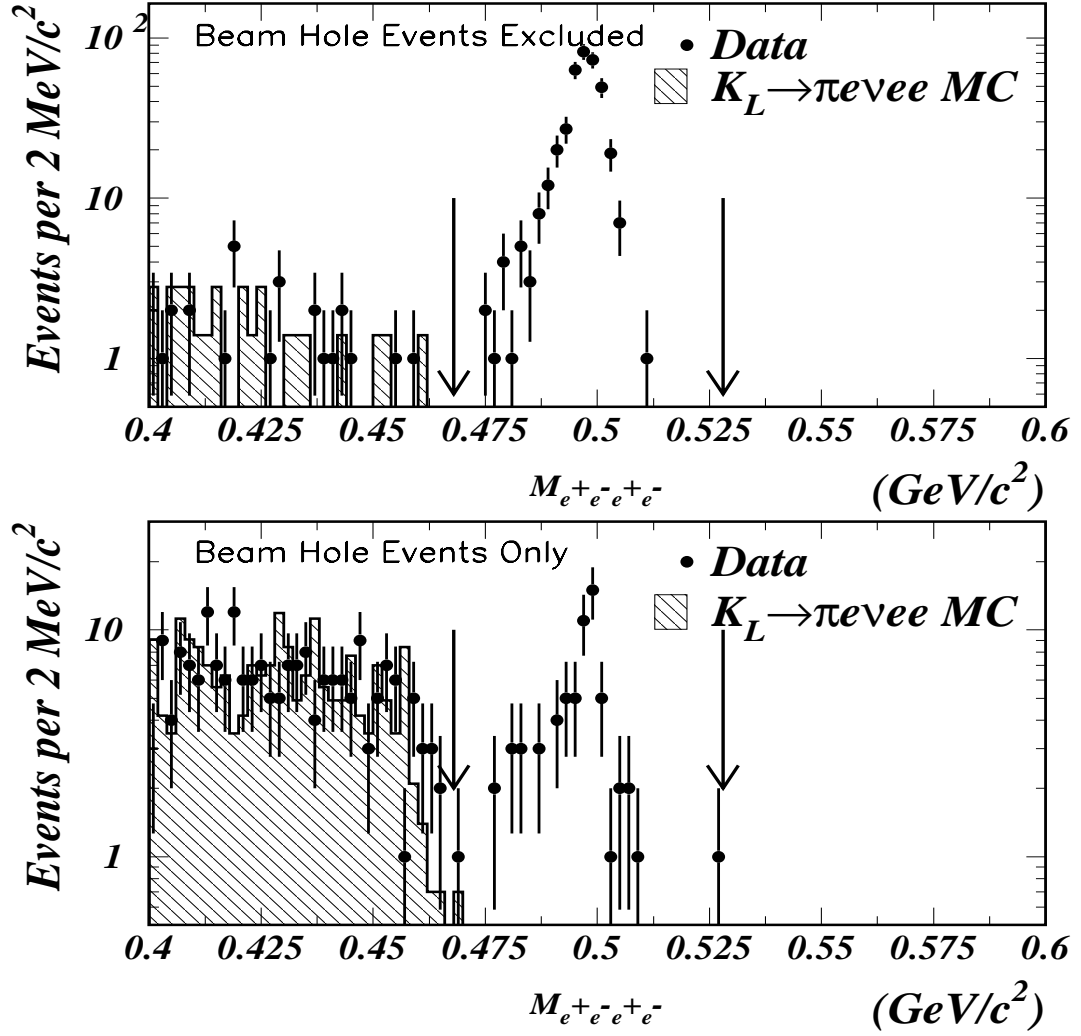


Figure 6.14: The top plot shows the $M_{e^+e^-e^+e^-}$ distribution for data and the $K_L \rightarrow \pi e \nu ee$ Monte Carlo excluding the beam hole events. The bottom plot shows the same distribution for beam hole events only. This illustrates that this background needs to be considered only for the beam hole events. The events between the arrows indicate the accepted region.

the entire $K_L \rightarrow e^+e^-e^+e^-$ sample. Figure 6.14 illustrates that this background needs to be considered only for the beam hole events. The top plot shows the $M_{e^+e^-e^+e^-}$ distribution for data and the $K_L \rightarrow \pi e \nu e e$ Monte Carlo excluding the beam hole events. The bottom plot shows the same distribution for beam hole events only. Using the above approximation of $B(K_L \rightarrow \pi e \nu e e)$ and the Monte Carlo simulation, the background level due to $K_L \rightarrow \pi e \nu e e$ was estimated to be $(0.11 \pm 0.11)\%$ or 0.5 ± 0.5 events.

6.4.3 Summary of All Backgrounds to $K_L \rightarrow e^+e^-e^+e^-$

We summarize the results of the last two sections on backgrounds in table 6.4.

Background to $K_L \rightarrow e^+e^-e^+e^-$:

Table 6.4: Summary of $K_L \rightarrow e^+e^-e^+e^-$ Backgrounds

Type of background	# of bkgr events after all cuts	% bkgr after all cuts
Photon conversions	3.7	0.84
$K_L \rightarrow \pi e \nu e e$	0.5	0.11
Total	4.2	0.95

6.5 Data vs. Monte Carlo

We have shown that the background levels are low, so we show here a few more data vs. MC distribution comparisons. In particular, we compare distributions with the KTeV implemented radiative corrections in the MC versus using PHOTOS. Figures 6.15 and 6.16 show the vertex Z distribution and kaon momentum distributions for $K_L \rightarrow e^+e^-e^+e^-$ events compared to Monte Carlo with PHOTOS. These figures should be compared to figures 6.5 and 6.6 to see that there is reasonable agreement between both sets of distributions.

A visible difference between the two methods of radiative correction implementation shows up in the $M_{e^+e^-e^+e^-}$ distribution. Figures 6.17 and 6.18 show this distribution for data and for Monte Carlo with PHOTOS and without any radiative corrections simulation, respectively. These figures should be compared to figure 6.10 to see that the

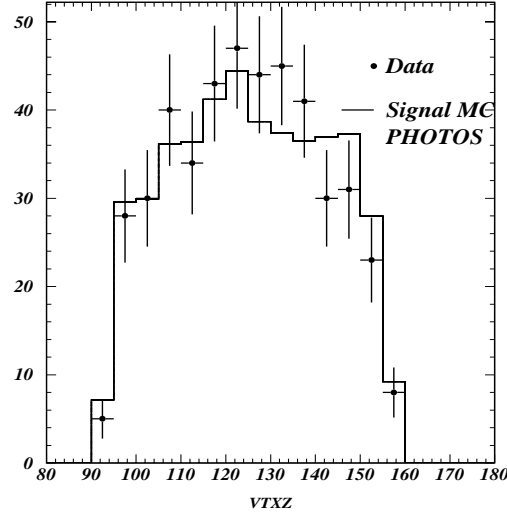


Figure 6.15: Vertex Z distribution for signal events compared to Monte Carlo with PHOTOS. Comparing this figure to figure 6.5 we see that the two Monte Carlos both do an adequate job simulating the data in this variable.

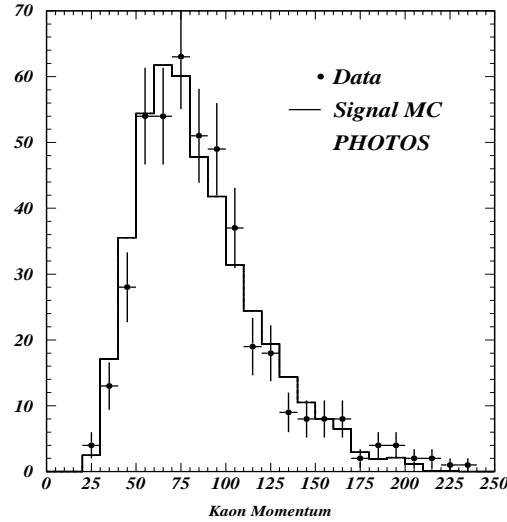


Figure 6.16: Kaon momentum distribution for signal events compared to Monte Carlo PHOTOS. Comparing this figure to figure 6.6 we see that the two Monte Carlos both do an adequate job simulating the data in this variable..

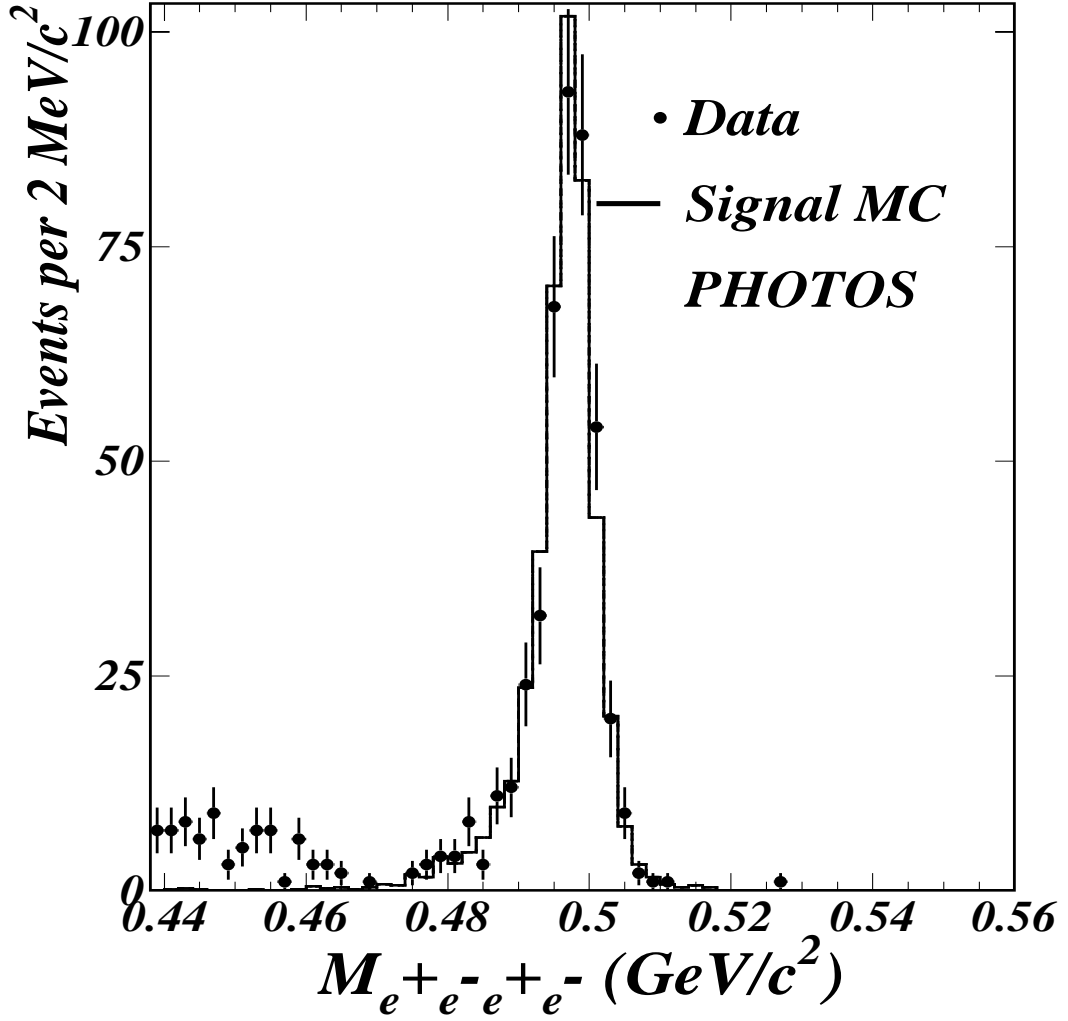


Figure 6.17: The $M_{e^+e^-e^+e^-}$ distribution after all cuts except the invariant mass cut. The dots represent the data and the histogram represents the Monte Carlo simulation using PHOTOS. Comparing this figure to figures 6.10 and 6.18 we see that the KTeV MC with radiative correction implemented was slightly better at simulating the radiative tail compared to PHOTOS.

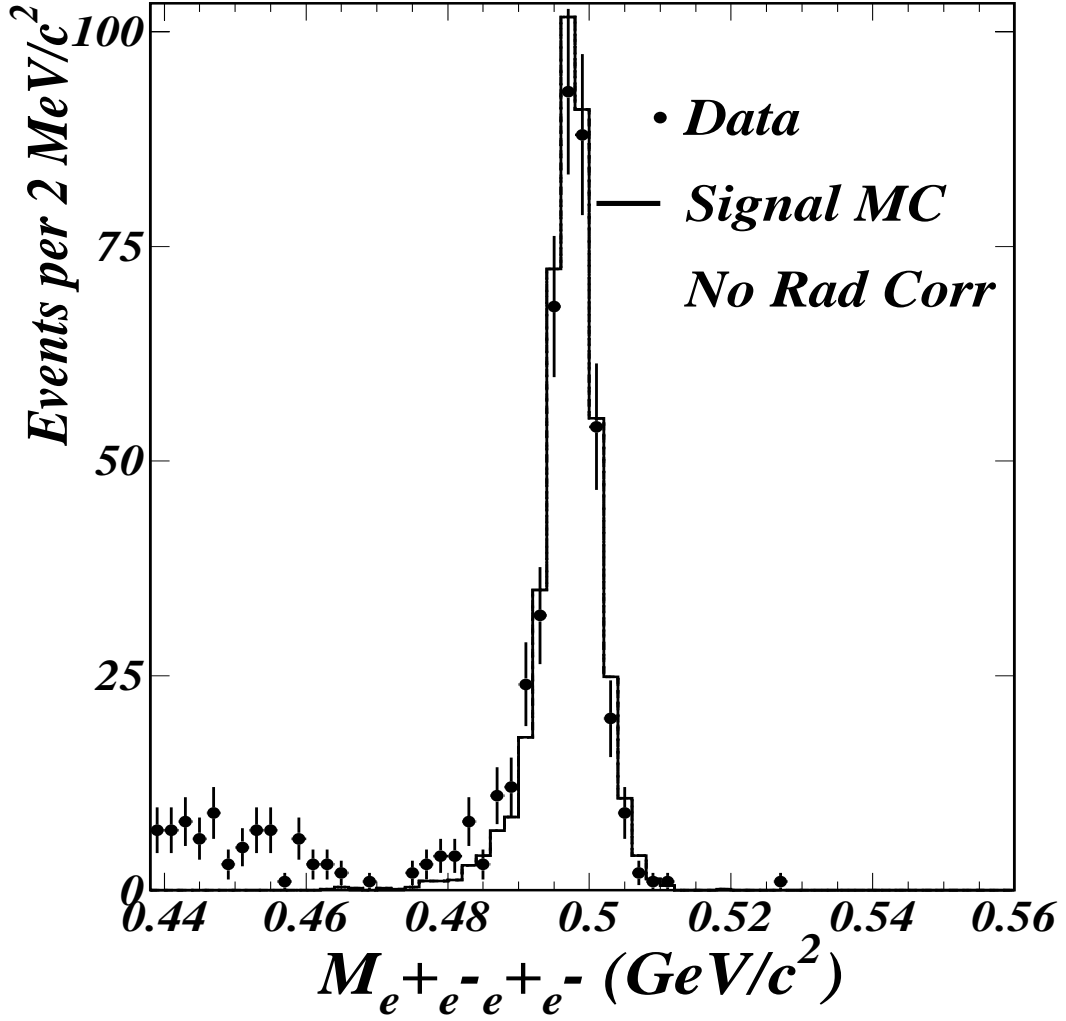


Figure 6.18: The $M_{e^+e^-e^+e^-}$ distribution after all cuts except the invariant mass cut. The dots represent the data and the histogram represents the Monte Carlo without radiative corrections in the MC. Comparing this figure to figures 6.10 and 6.17 we notice the absence of the low-side radiative tail in this MC simulation.

KTeV MC with radiative correction implemented was slightly better at simulating the radiative tail compared to PHOTOS. Therefore, for all analyses in this thesis, the KTeV MC with implemented radiative corrections was used as the default MC simulation and other simulations were used only for systematic studies.

6.6 Summary of $K_L \rightarrow e^+e^-e^+e^-$ Signal Extraction

We observe a total of 441 $K_L \rightarrow e^+e^-e^+e^-$ events with 4.2 background events. This low background is mostly $K_L \rightarrow e^+e^-\gamma$ events with photon conversions. This 441 event sample is used in the form factor (chapter 8) and $B(K_L \rightarrow e^+e^-e^+e^-)$ (chapter 9) analyses. A smaller sub-sample of these events is used in the analysis of the angular distribution (chapter 10).

Chapter 7

Normalization Mode

7.1 Event Signatures and Backgrounds to $K_L \rightarrow \pi^0 \pi_D^0 \pi_D^0$

The normalization mode decay $K_L \rightarrow \pi^0 \pi_D^0 \pi_D^0$ had a similar event signature to the signal mode. The final state of the normalization mode is $e^+ e^- e^+ e^- \gamma \gamma \gamma \gamma$. Again, we looked for two positively charged tracks and two negatively charged tracks all originating from one vertex and identified as electrons or positrons. In addition, we looked for four extra clusters in the CsI with no match to a track. Since the K_L decayed to three π^0 's, we searched for combinations of $\gamma\gamma$ and $e^+ e^- \gamma$ that reconstructed to the invariant mass of the π^0 .

A source of background to the decay $K_L \rightarrow \pi^0 \pi_D^0 \pi_D^0$ was the decay $K_L \rightarrow \pi^0 \pi^0 \pi_D^0$ since both have the same eight particle final state of $e^+ e^- e^+ e^- \gamma \gamma \gamma \gamma$. Another source of background was the decay $K_L \rightarrow \pi^0 \pi^0 \pi_D^0$ when the photon from one of the non-Dalitz π^0 's converted in the detector material. These backgrounds are discussed in detail in section 7.4.

7.2 Selecting Candidate $K_L \rightarrow \pi^0 \pi_D^0 \pi_D^0$ Events

To select $K_L \rightarrow \pi^0 \pi_D^0 \pi_D^0$ events, common cuts to the ones selecting $K_L \rightarrow e^+ e^- e^+ e^-$ were used, such as the particle identification, trigger verification and data quality cuts, described in chapter 6. Again, the winter analysis runs used ranged from run number 8245-8910 and the summer analysis runs from 10463-10970 (see figure 7.1). The normalization mode $K_L \rightarrow \pi^0 \pi_D^0 \pi_D^0$ selection criteria are listed in table 7.1¹.

The distribution of the Z position of the charged vertex and the total momentum

¹ δM_{2D}^2 and δM_{DD}^2 in table 7.1 is defined below in the background section 7.4.

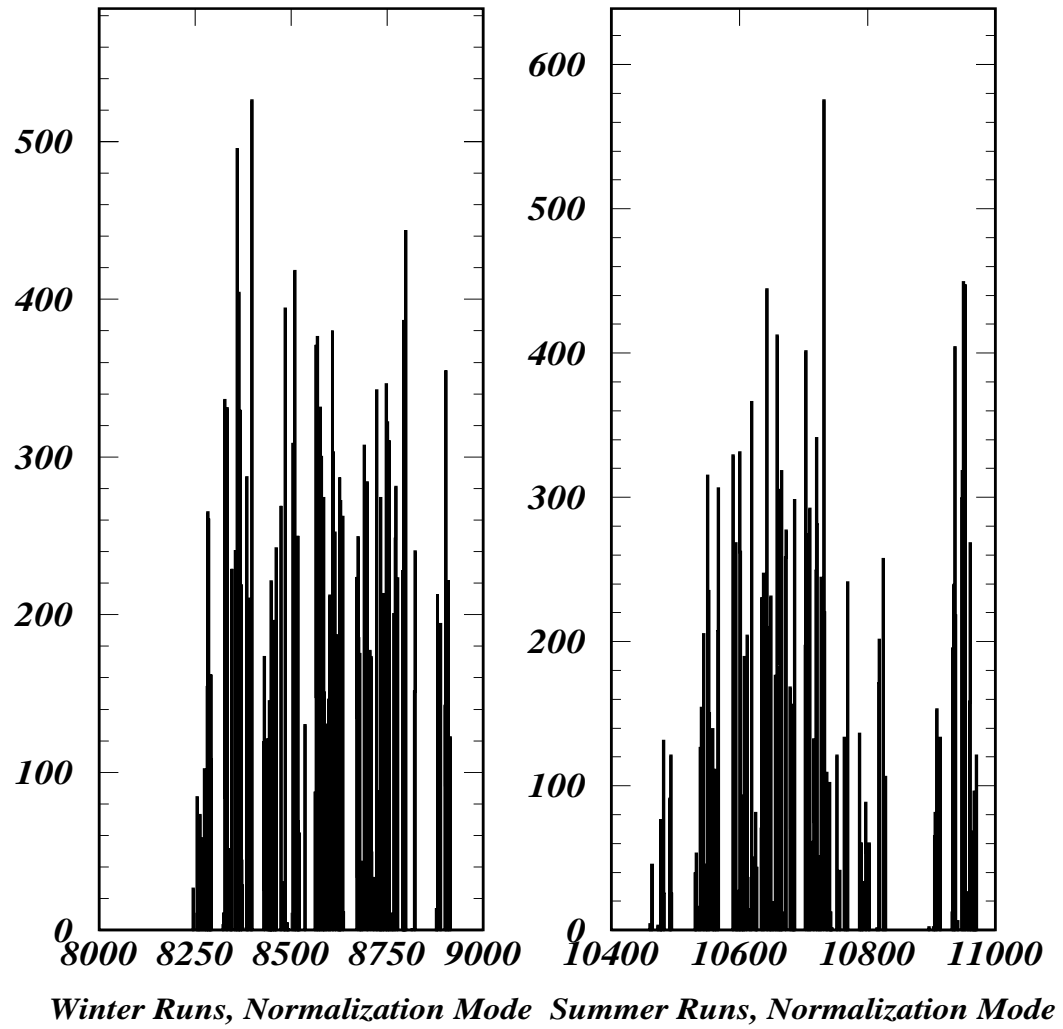


Figure 7.1: Events vs. Run Number for normalization mode events for both winter and summer data taking conditions.

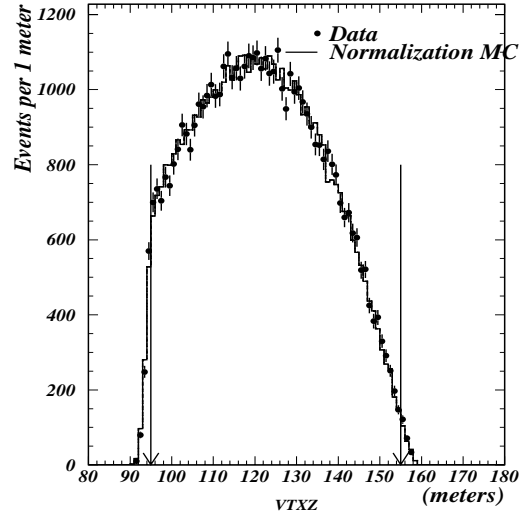


Figure 7.2: Vertex Z distribution for normalization mode events compared to Monte Carlo. The arrows indicate the position of the cut.

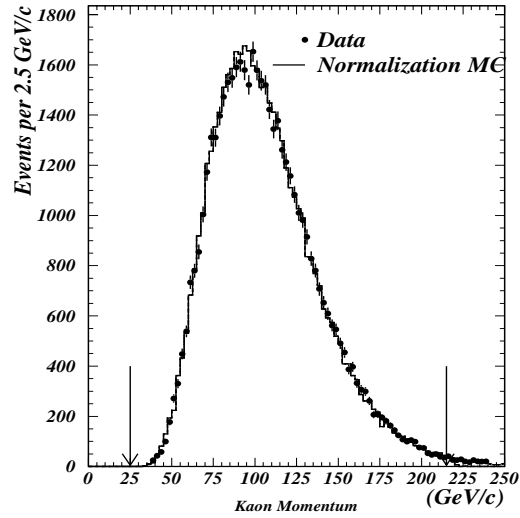


Figure 7.3: Kaon momentum distribution for normalization mode events compared to Monte Carlo. The arrows indicate the position of the cut.

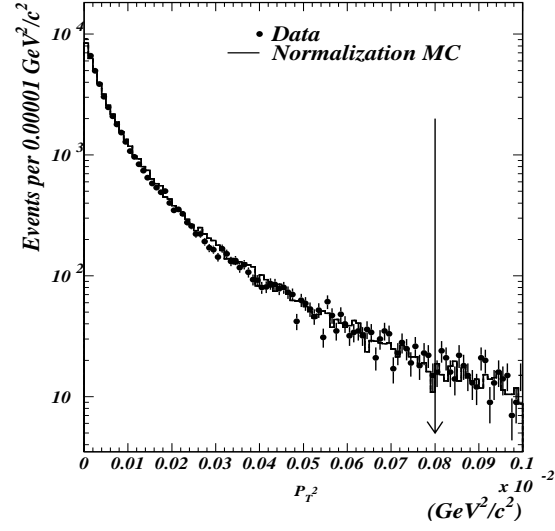


Figure 7.4: The distribution of P_T^2 for candidate $K_L \rightarrow \pi^0 \pi_D^0 \pi_D^0$ events compared to Monte Carlo. The arrow indicates the position of the cut.

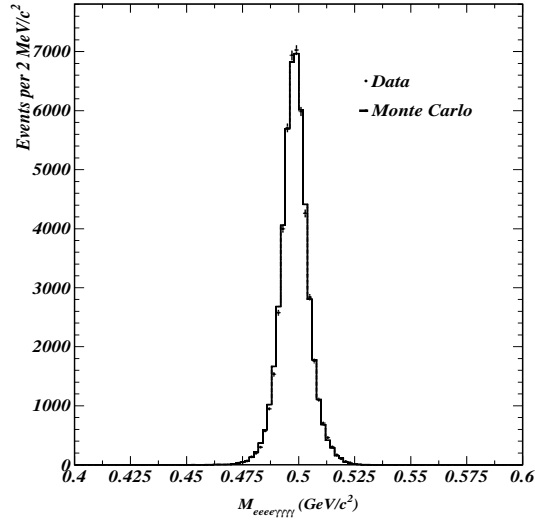


Figure 7.5: The $M_{e^+e^-e^+e^-\gamma\gamma\gamma\gamma}$ distribution for the normalization mode events after all cuts but the cut on the invariant mass. The dots are the data and the histogram is the Monte Carlo simulation.

Table 7.1: $K_L \rightarrow \pi^0 \pi_D^0 \pi_D^0$ Selection Cuts

Normalization Mode cuts	Cut value
Number of tracks that make a vertex	4
Minimum cluster energy	2 GeV
E/P	0.9 - 1.1
Number of electrons (E/P above)	4
Number of e^+e^-	$2e^+, 2e^-$
Max RC, SCIA energy	$0.5 GeV$
Max CA energy	$5.0 GeV$
Number of photons	4
VTXZ	$95 - 155 m$
$P_{e^+e^-e^+e^- \gamma \gamma \gamma \gamma}$	$25 - 215 GeV/c^2$
$P_T^2_{e^+e^-e^+e^- \gamma \gamma \gamma \gamma}$	$< 800 (MeV/c)^2$
vertex χ^2	< 300
offmag χ^2	< 100
$M_{e^+e^-e^+e^- \gamma \gamma \gamma \gamma}$	$478 - 518 MeV$
Minimum track separation at DC1	$> 1 mm$
δM_{2D}^2	$< \delta M_{DD}^2$
$M_{\gamma \gamma}$	$127.5 - 142.5 MeV$
$M_{e^+e^- \gamma}$	$127.5 - 142.5 MeV$
$M_{e^+e^-e^+e^-}$	$\neq 127.5 - 142.5 MeV$

of the kaon in the lab are shown in figures 7.2 and 7.3. Figure 7.4 shows the P_T^2 distribution for normalization mode events. We also show the $M_{e^+e^-e^+e^- \gamma \gamma \gamma \gamma}$ distribution for the normalization mode events after all cuts but the cut on the invariant mass in figure 7.5. These P_T^2 and $M_{e^+e^-e^+e^- \gamma \gamma \gamma \gamma}$ cuts define the $K_L \rightarrow \pi^0 \pi_D^0 \pi_D^0$ signal region with an efficiency of 95%.

7.3 Normalization Events

There were 49089 $K_L \rightarrow \pi^0 \pi_D^0 \pi_D^0$ events after all the cuts described in the previous section. We summarize the total number of events observed in the $K_L \rightarrow \pi^0 \pi_D^0 \pi_D^0$ decay in table 7.2.

Table 7.2: Total Number of Normalization Mode Events

Total $K_L \rightarrow \pi^0 \pi_D^0 \pi_D^0$ candidate events	49089
Winter events	27808
Summer events	21281

7.4 Background Estimation in $K_L \rightarrow \pi^0 \pi_D^0 \pi_D^0$ (Normalization Mode)

7.4.1 Crossover Background

The decay $K_L \rightarrow \pi^0 \pi_D^0 \pi_D^0$ (normalization) and the decay $K_L \rightarrow \pi^0 \pi^0 \pi_D^0$ both have the same eight particle final state of $e^+ e^- e^+ e^- \gamma \gamma \gamma \gamma$. It was important to be able to separate these two decay modes since their branching ratios differ only by roughly a factor of four.

In order to distinguish between these two decays, first we needed to determine how to pair the photons and electrons for each case by creating a χ^2 based on the π^0 masses for each mode. We refer to this as the Mass- χ^2 method. The objective of this technique is to separate the two modes based on the best mass- χ^2 for the corresponding π^0 decay hypothesis (two $\pi^0 \rightarrow \gamma\gamma$ and a $\pi^0 \rightarrow eeee$ or one $\pi^0 \rightarrow \gamma\gamma$ and two $\pi^0 \rightarrow ee\gamma$). Then, comparing the best mass- χ^2 's for each hypothesis provided us with the information needed to decide if an event decayed as $K_L \rightarrow \pi^0 \pi_D^0 \pi_D^0$ or as $K_L \rightarrow \pi^0 \pi_D^0 \pi_D^0$. Specifically, for $K_L \rightarrow \pi^0 \pi_D^0 \pi_D^0$:

$$\delta M_{DD}^2 = \frac{(m_{\gamma\gamma_1} - m_{\pi^0})^2}{\sigma_{\gamma\gamma}^2} + \frac{(m_{\gamma\gamma_2} - m_{\pi^0})^2}{\sigma_{\gamma\gamma}^2} + \frac{(m_{eeee} - m_{\pi^0})^2}{\sigma_{eeee}^2} \quad (7.1)$$

For this mode, there are 3 different ways to pair up the photons. The pair with the lowest δM_{DD}^2 is the one that was chosen. Then for $K_L \rightarrow \pi^0 \pi_D^0 \pi_D^0$:

$$\delta M_{2D}^2 = \frac{(m_{ee\gamma_1} - m_{\pi^0})^2}{\sigma_{ee\gamma}^2} + \frac{(m_{ee\gamma_2} - m_{\pi^0})^2}{\sigma_{ee\gamma}^2} + \frac{(m_{\gamma\gamma} - m_{\pi^0})^2}{\sigma_{\gamma\gamma}^2} \quad (7.2)$$

This time there are 24 different ways to combine 2 $ee\gamma$ s and one $\gamma\gamma$. Again, the pairing with the lowest δM_{2D}^2 was chosen. The σ 's were obtained by fitting a Gaussian to the

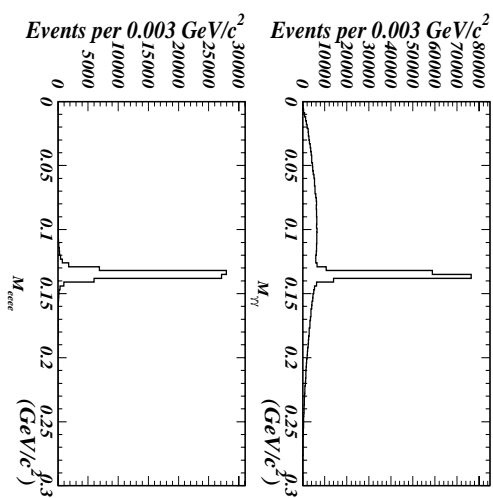


Figure 7.6: $m_{\gamma\gamma}$ (top) and m_{eeee} (bottom) for $K_L \rightarrow \pi^0 \pi_D^0$ Monte Carlo. The top plot contains 3 entries per event and the bottom plot contains 1 entry per event. Mispairings of the photons gives the top distribution a non-Gaussian structure.

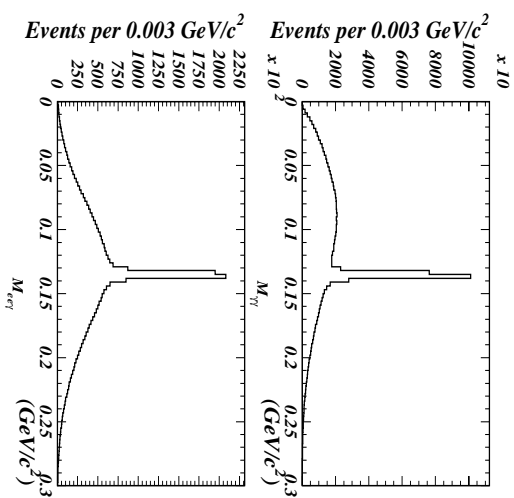


Figure 7.7: $m_{\gamma\gamma}$ (top) and $m_{ee\gamma}$ (bottom) for $K_L \rightarrow \pi^0 \pi_D^0$ Monte Carlo. The top plot contains 6 entries per event and the bottom plot contains 16 entry per event. Mispairings of the particles gives these distributions non-Gaussian structures.

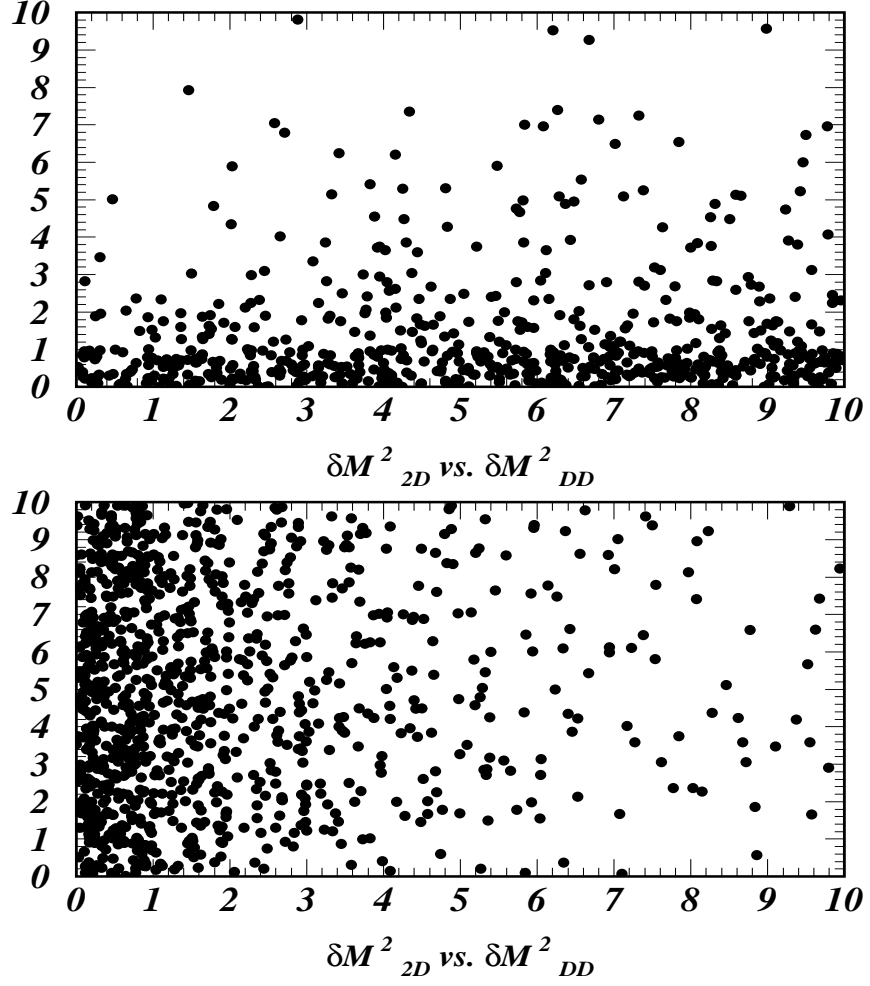


Figure 7.8: The best δM^2_{2D} versus the best δM^2_{DD} for $K_L \rightarrow \pi^0 \pi_D^0 \pi_D^0$ Monte Carlo (top) and $K_L \rightarrow \pi^0 \pi^0 \pi_{DD}^0$ Monte Carlo (bottom). These figures show that δM^2_{2D} is small compared to δM^2_{DD} for $K_L \rightarrow \pi^0 \pi_D^0 \pi_D^0$ events and vice versa.

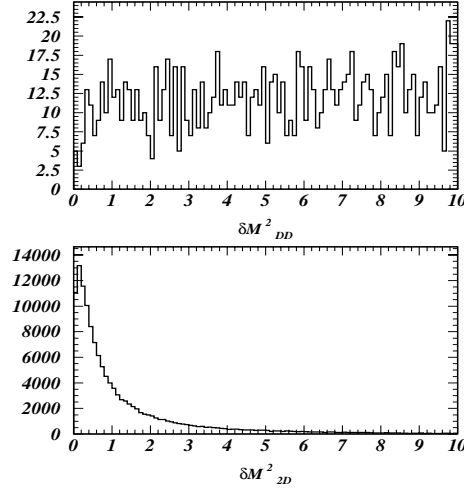


Figure 7.9: The δM^2_{DD} and δM^2_{2D} distributions for $K_L \rightarrow \pi^0 \pi_D^0 \pi_D^0$ MC. The δM^2_{2D} distribution for these events is peaked at low values whereas the δM^2_{DD} distribution is flat. Note that the probability of misidentification drops for lower values of the δM^2 .

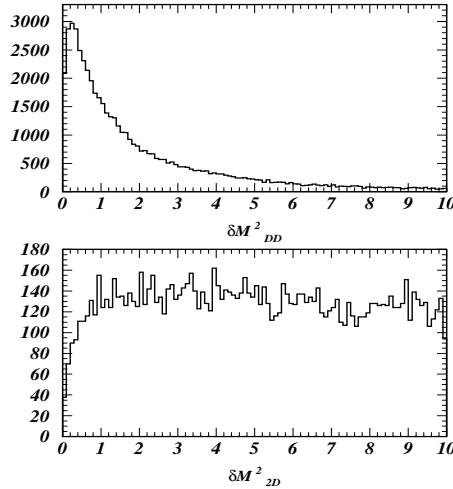


Figure 7.10: The δM^2_{DD} and δM^2_{2D} distributions for $K_L \rightarrow \pi^0 \pi^0 \pi_{DD}^0$ MC. The δM^2_{DD} distribution for these events is peaked at low values whereas the δM^2_{2D} distribution is flat. Note that the probability of misidentification drops for lower values of the δM^2 .

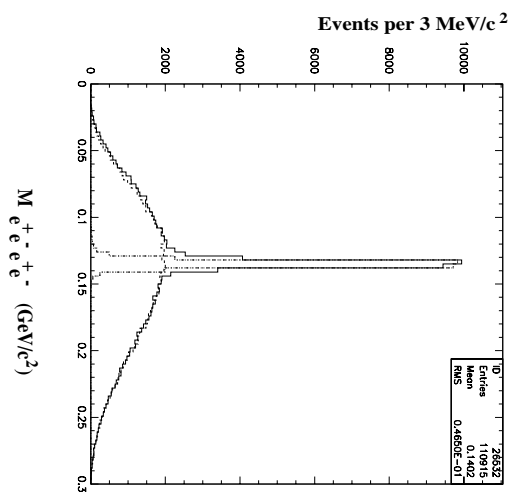


Figure 7.11: $M_{e^+e^-e^+e^-}$: The solid line is data. The dashed dotted line is $K_L \rightarrow \pi^0\pi^0\pi_D^0$ MC and the dashed line is $K_L \rightarrow \pi^0\pi_D^0\pi_D^0$ MC. This shows that the spike at the π^0 mass is the $\pi^0 \rightarrow e^+e^-e^+e^-$ and the broad distribution under the spike is from $K_L \rightarrow \pi^0\pi_D^0\pi_D^0$ events.

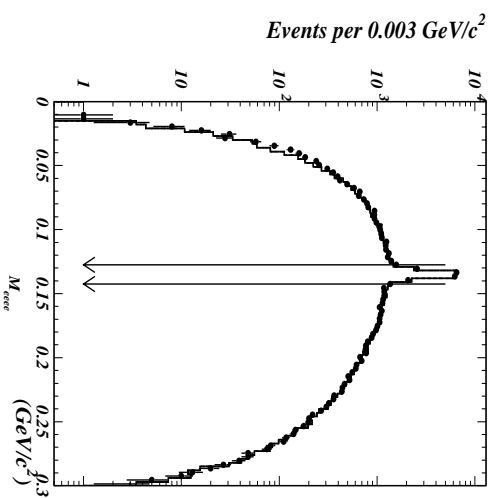


Figure 7.12: Same as figure 7.11 above with a log scale. The dots represent the data and the line represents a normalized combination of the $K_L \rightarrow \pi^0\pi^0\pi_D^0$ and $K_L \rightarrow \pi^0\pi_D^0\pi_D^0$ Monte Carlos, showing excellent agreement between data and Monte Carlo. The events between the arrows indicate the region that is excluded.

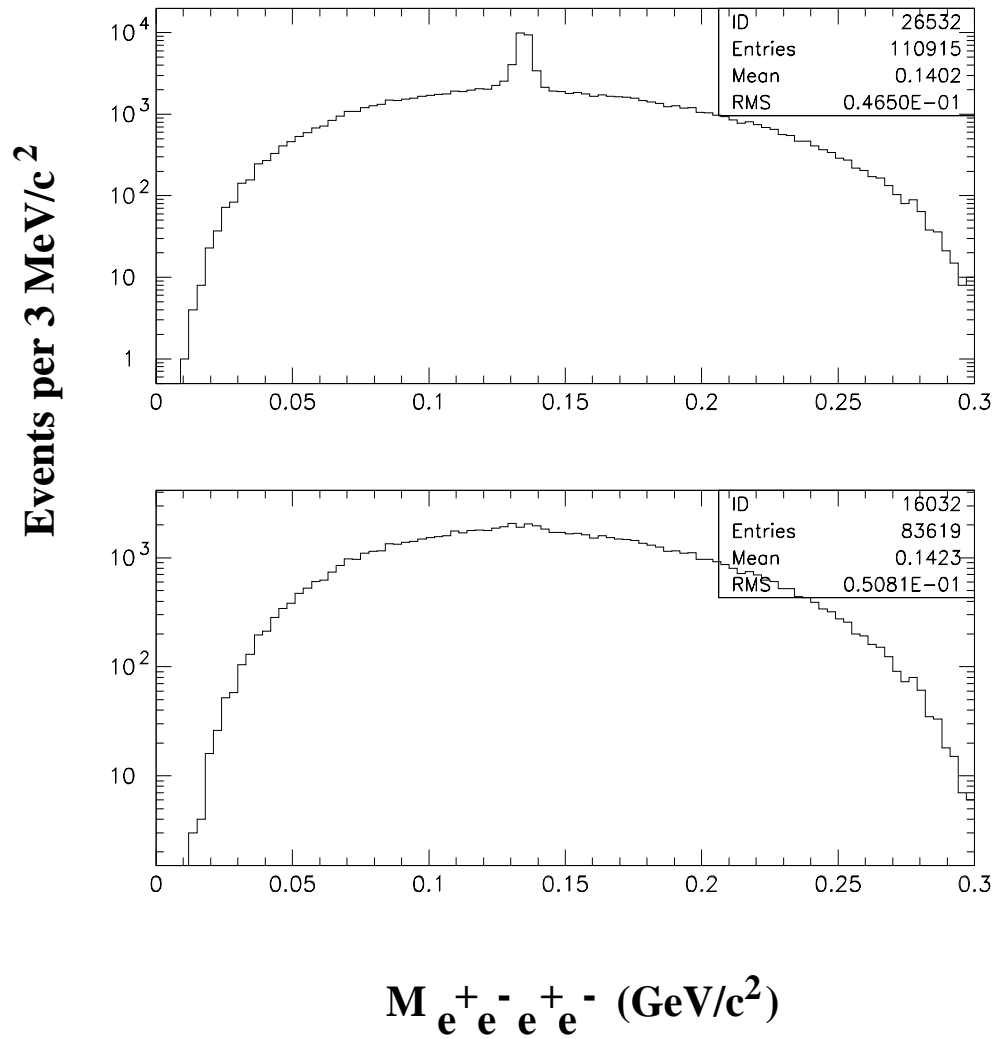


Figure 7.13: $M_{e^+e^-e^+e^-}$: The top plot shows the data before the Mass- χ^2 separation. The bottom plot shows the $K_L \rightarrow \pi^0 \pi_D^0 \pi_D^0$ data after the Mass- χ^2 separation. This technique is very efficient in separating the $K_L \rightarrow \pi^0 \pi_D^0 \pi_D^0$ and $K_L \rightarrow \pi^0 \pi^0 \pi_D^0$ modes.

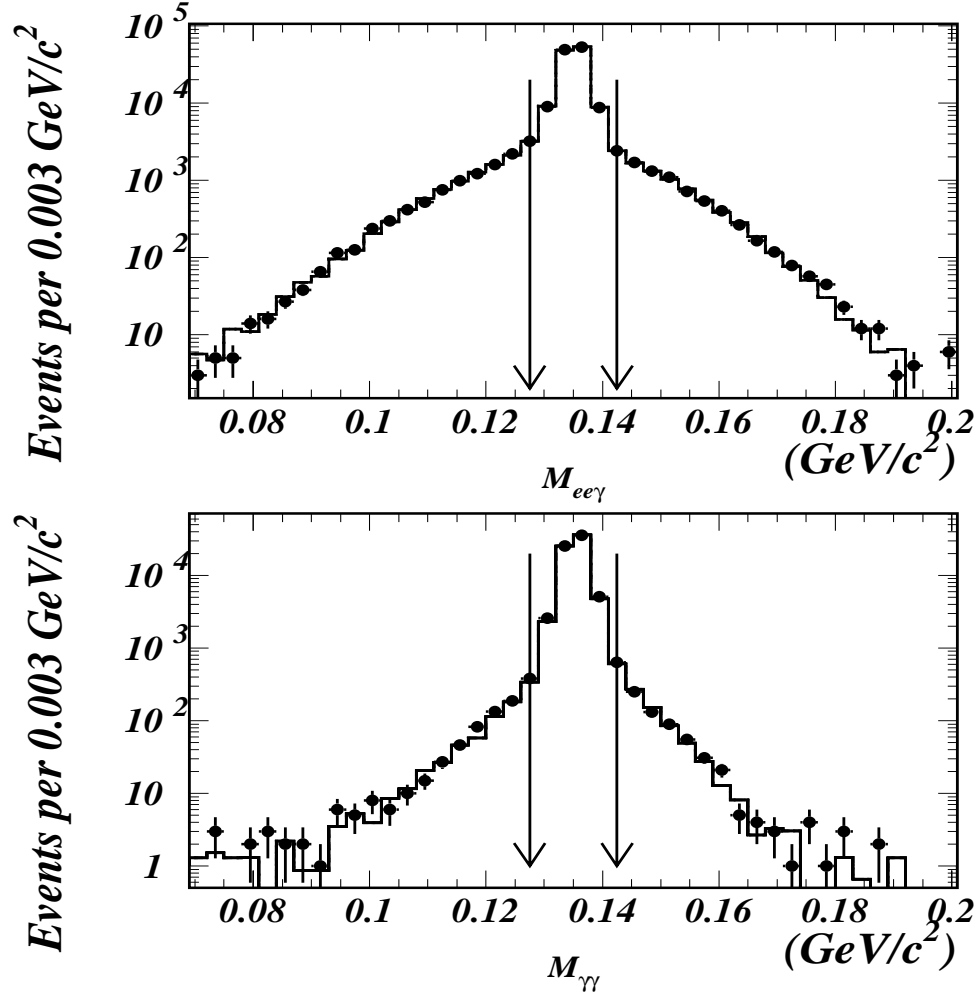


Figure 7.14: The distribution of the $m_{\gamma\gamma}$ and $m_{ee\gamma}$ invariant masses where the dots represent the data and the line represents a normalized combination of the $K_L \rightarrow \pi^0\pi^0\pi_D^0\pi_D^0$ and $K_L \rightarrow \pi^0\pi_D^0\pi_D^0$ Monte Carlos, showing agreement between data and MC. The events between the arrows indicate the region that is included.

central region of each of the π^0 masses, when we plotted one entry for each combination, in data. Figure 7.6 shows the distributions of $m_{\gamma\gamma}$ and m_{eee} for $K_L \rightarrow \pi^0\pi^0\pi_D^0$ Monte Carlo for all 3 possible combinations, while figure 7.7 shows the distributions of $m_{\gamma\gamma}$ and $m_{ee\gamma}$ for $K_L \rightarrow \pi^0\pi_D^0\pi_D^0$ Monte Carlo for all 24 possible combinations.

The best pairing for each case was by now picked, however, the two decays were not separated. Figure 7.8 shows the best δM_{2D}^2 versus the best δM_{DD}^2 for $K_L \rightarrow \pi^0\pi_D^0\pi_D^0$ Monte Carlo (top) and $K_L \rightarrow \pi^0\pi^0\pi_D^0$ Monte Carlo (bottom). These figures show that δM_{2D}^2 is small compared to δM_{DD}^2 for $K_L \rightarrow \pi^0\pi_D^0\pi_D^0$ events and vice versa. Figures 7.9 and 7.10 further illustrate this point. Here we show the δM_{DD}^2 and δM_{2D}^2 distributions for $K_L \rightarrow \pi^0\pi_D^0\pi_D^0$ and $K_L \rightarrow \pi^0\pi^0\pi_D^0$ Monte Carlo simulations. The δM^2 distribution for the respective event type is peaked at low values whereas the other distribution is flat. Therefore, to separate the two, we compared the lowest δM_{DD}^2 to the lowest δM_{2D}^2 . Choosing the smaller of the two determined if an event was a $K_L \rightarrow \pi^0\pi^0\pi_D^0$ or if it was a $K_L \rightarrow \pi^0\pi_D^0\pi_D^0$.

Figure 7.11 shows the distribution of the $e^+e^-e^+e^-$ invariant mass. The solid line represents the data, the dashed dotted line represents the $K_L \rightarrow \pi^0\pi^0\pi_D^0$ MC and the dashed line represents $K_L \rightarrow \pi^0\pi_D^0\pi_D^0$ MC. We see from this figure that the spike at the π^0 mass is the $\pi^0 \rightarrow e^+e^-e^+e^-$ and the broad distribution under the spike is from $K_L \rightarrow \pi^0\pi_D^0\pi_D^0$ events. Figure 7.12 also shows the distribution of the $e^+e^-e^+e^-$ invariant mass where the dots represent the data and the line represents a normalized combination of the $K_L \rightarrow \pi^0\pi^0\pi_D^0$ and $K_L \rightarrow \pi^0\pi_D^0\pi_D^0$ Monte Carlos, indicating agreement between data and Monte Carlo. The region between the arrows is excluded. In figure 7.13 the top plot shows the data before the Mass- χ^2 separation. The bottom plot shows the $K_L \rightarrow \pi^0\pi_D^0\pi_D^0$ data after the Mass- χ^2 separation. These plots show that this technique was very efficient in separating the $K_L \rightarrow \pi^0\pi_D^0\pi_D^0$ and $K_L \rightarrow \pi^0\pi^0\pi_D^0$ modes. We also required that the $m_{\gamma\gamma}$ and $m_{ee\gamma}$ reconstructed to the π^0 mass as shown in figure 7.14. Here the dots represent the data and the line represents a normalized combination of the $K_L \rightarrow \pi^0\pi^0\pi_D^0$ and $K_L \rightarrow \pi^0\pi_D^0\pi_D^0$ Monte Carlos, indicating agreement between data and MC.

The background from a $K_L \rightarrow \pi^0\pi_D^0\pi_D^0$ event crossing over to a $K_L \rightarrow \pi^0\pi^0\pi_D^0$

event, and vice versa, was calculated using Monte Carlo. We estimated this background using the total number of kaon decays in our detector. This number was calculated using the decay $K_L \rightarrow \pi^0 \pi_D^0 \pi_D^0$ ². The number of kaon decays, N_K (“Flux”), was then calculated using:

$$N_K = \frac{N_{\text{observed}}}{B \times \text{Acceptance}} \quad (\text{“Flux”}). \quad (7.3)$$

The branching ratio of $K_L \rightarrow \pi^0 \pi_D^0 \pi_D^0$ from PDG is $(8.98 \pm 0.49) \times 10^{-5}$. The total number of kaon decays was $(2.63 \pm 0.02_{\text{stat}} \pm 0.14_{\text{syst}}) \times 10^{11}$. The systematic error comes from the PDG error in the branching ratio.

We used equation 7.3 above and the value for the total number of kaon decays to find out how many crossover background events there were in the total data. Also, to estimate the level of this background, the PDG value of the branching ratio of $\pi^0 \rightarrow e^+ e^- e^+ e^-$ was used, $(3.14 \pm 0.30) \times 10^{-5}$ [10].

We find that the percentage of $K_L \rightarrow \pi^0 \pi_D^0 \pi_D^0$ events mistaken as a $K_L \rightarrow \pi^0 \pi_D^0 \pi_D^0$ event was about $(0.04 \pm 0.01)\%$ or (21 ± 3) events after the Mass- χ^2 selection. Therefore, this background was negligible after all cuts. The loss of $K_L \rightarrow \pi^0 \pi_D^0 \pi_D^0$ events due to Mass- χ^2 selection and π^0 mass cuts was $(14.62 \pm 0.06)\%$.

7.4.2 Photon Conversions

If in the decay $K_L \rightarrow \pi^0 \pi_D^0 \pi_D^0$ the photon from one of the non-Dalitz π^0 's converted in the vacuum window this would have shown up as background to $K_L \rightarrow \pi^0 \pi_D^0 \pi_D^0$. Again, to remove the photon conversion background we cut on the separation of tracks at DC1. We cut out events that had a minimum track separation of less than 1mm to remove this background.

Only single conversions from the $K_L \rightarrow \pi^0 \pi_D^0 \pi_D^0$ decay were considered since, we will show, the level of this background was very small and double conversions (from $K_L \rightarrow \pi^0 \pi_D^0 \pi_D^0$ where two photons from different π^0 's convert) was even smaller and essentially negligible. To obtain the number of expected conversion events in $K_L \rightarrow$

²A very tight cut on the minimum track separation was used to remove essentially all of the conversion background (the dominant background to $K_L \rightarrow \pi^0 \pi_D^0 \pi_D^0$). See section 7.4.2.

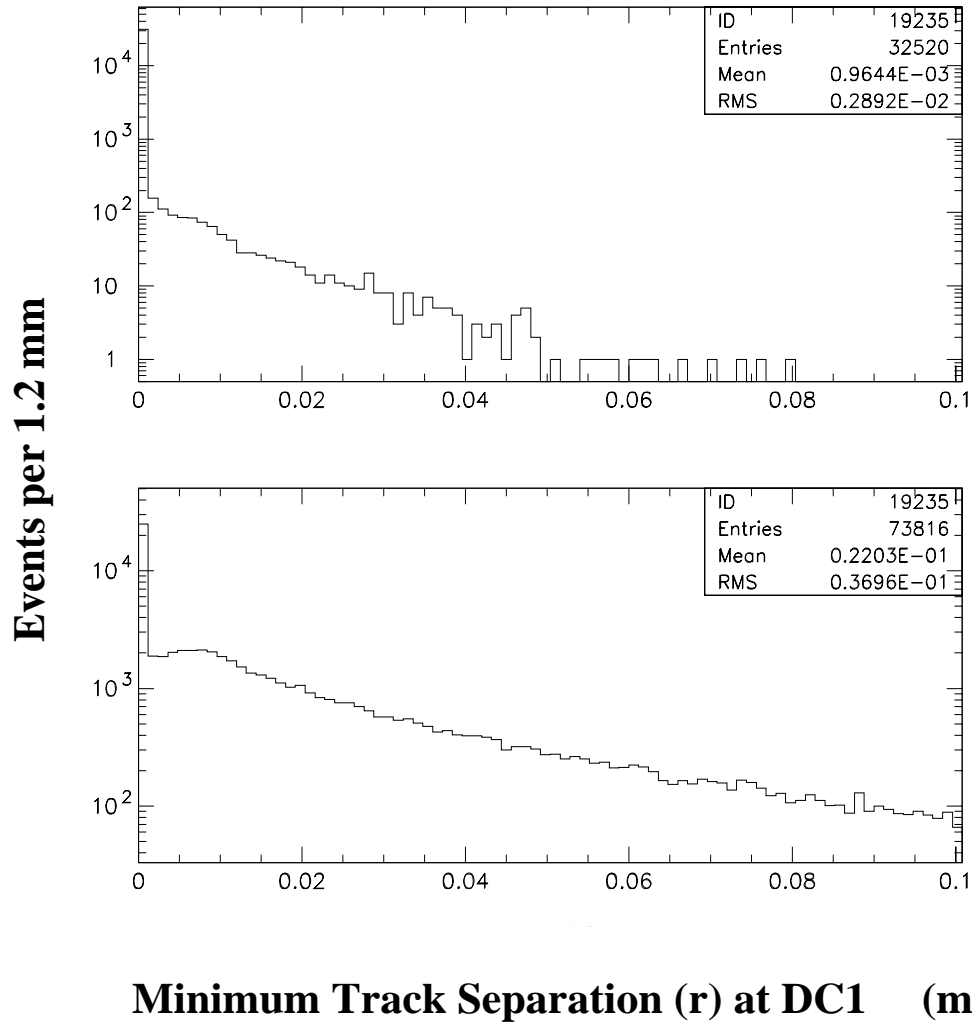


Figure 7.15: The top plot shows the distribution of the minimum track separation at DC1 for $K_L \rightarrow \pi^0 \pi_D^0 \gamma \gamma_c$ MC. The bottom shows the $K_L \rightarrow \pi^0 \pi_D^0 \pi_D^0$ MC (normalization mode). These are not normalized to the data.

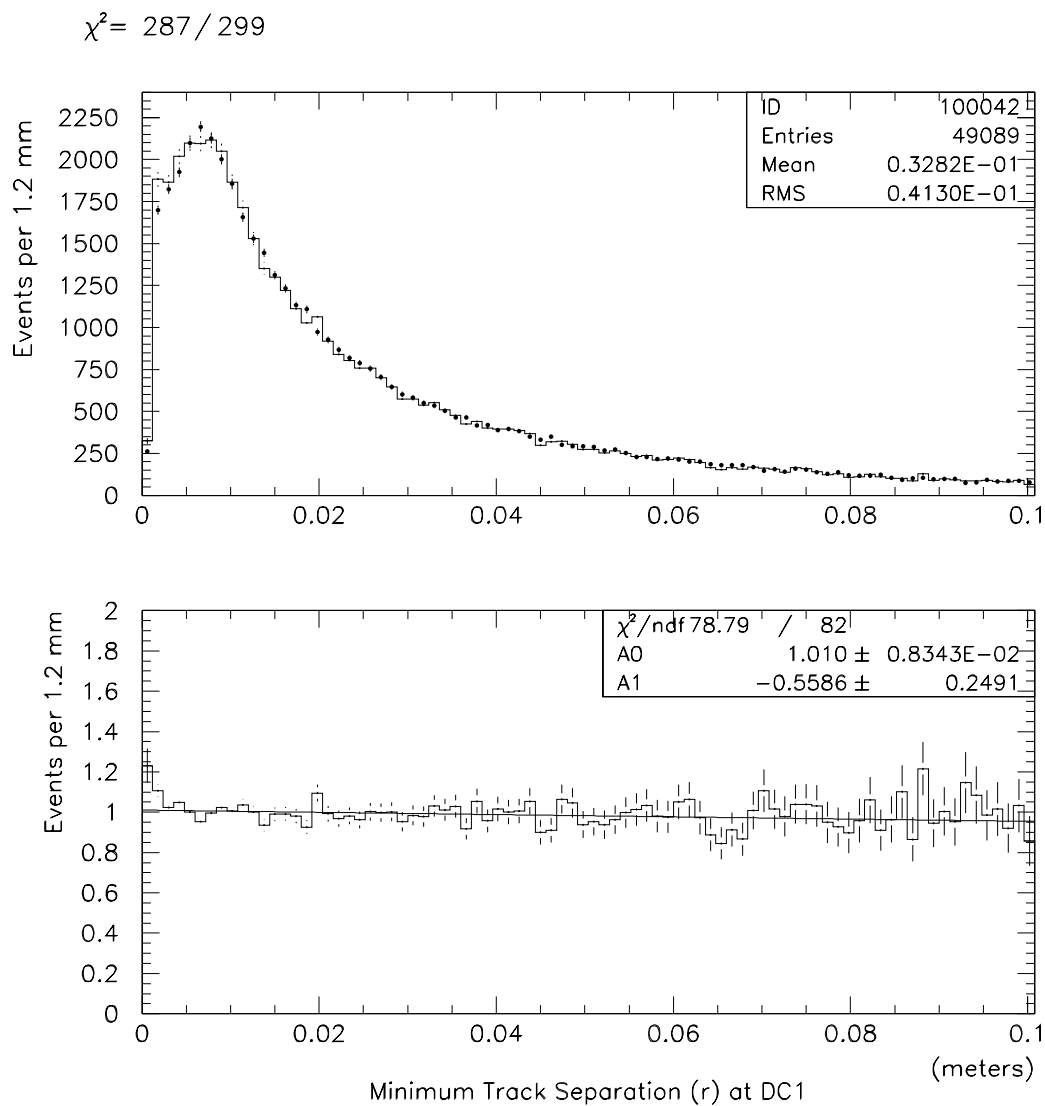


Figure 7.16: Distribution of the minimum track separation at DC1. The histogram is the $K_L \rightarrow \pi^0 \pi_D^0 \pi_D^0$ data and the dots are the MC after the conversion cut has been made. The bottom plot is data over MC. There is residual background visible in the first bin.

Table 7.3: $K_L \rightarrow \pi^0 \pi_D^0 \pi_D^0$ Conversion Background Estimate

Type of bkgr	bkgr before conv. cut	bkgr after cut	# bkgr events after cut
$K_L \rightarrow \pi^0 \pi_D^0 \pi_D^0$ (single conversion)	$(32 \pm 2)\%$	$(1.7 \pm 0.1)\%$	(844 ± 66)

$\pi^0 \pi_D^0 \pi_D^0$ we used an equation similar to equation 6.1, with the relevant acceptance and branching ratio. The conversion background estimation for normalization mode events is summarized in table 7.3.

The fraction of normalization mode events lost was obtained from Monte Carlo studies and was found to be about $(8.97 \pm 0.04_{\text{stat}})\%$. Therefore, the 1 mm cut on minimum track separation at DC1 was chosen to optimize background rejection and to minimize signal loss. As a result of cutting on the minimum separation of tracks at DC1 the level of conversion background was reduced to a tolerable low level.

In figure 7.15 the top plot shows the distribution of the track separation at DC1 for $K_L \rightarrow \pi^0 \pi_D^0 \gamma \gamma_c$ MC (one non-Dalitz π^0 converted). The bottom plot shows the same distribution for $K_L \rightarrow \pi^0 \pi_D^0 \pi_D^0$ MC. In figure 7.16 the histogram represents the $K_L \rightarrow \pi^0 \pi_D^0 \pi_D^0$ data and the dots represent the MC after the conversion cut was made. The bottom plot shows the ratio of data over MC and shows reasonable agreement, except for where we know we are letting in about 2% background.

7.4.3 Summary of All Backgrounds (Normalization Mode)

We summarize the results of the last two sections in table 7.4.

Table 7.4: Summary of $K_L \rightarrow \pi^0 \pi_D^0 \pi_D^0$ Backgrounds

Type of background	# events after all cuts	% bkgr after all cuts
Cross over	21	0.04
Conversion	844	1.7
Total	865	1.76

7.5 Normalization Mode Summary

We observe a total of 49089 $K_L \rightarrow \pi^0 \pi_D^0 \pi_D^0$ events with 865 background events. This low background is mostly $K_L \rightarrow \pi^0 \pi^0 \pi_D^0$ events with a photon conversion. In chapters 6 and 7, we show that the normalization mode events have reasonable agreement in the data and Monte Carlo comparisons for many distributions.

The reader should keep in mind that these events are used only in the $B(K_L \rightarrow e^+ e^- e^+ e^-)$ analysis (see chapter 9). In chapter 9, we see that although $K_L \rightarrow \pi^0 \pi_D^0 \pi_D^0$ is an ideal normalization mode for $K_L \rightarrow e^+ e^- e^+ e^-$, $B(K_L \rightarrow \pi^0 \pi_D^0 \pi_D^0)$ is measured to 5.5% of itself [10] and thus dominates the systematic uncertainty for $B(K_L \rightarrow e^+ e^- e^+ e^-)$. However, this uncertainty is due to an *external* systematic effect (i.e., external to KTeV).

Chapter 8

Form Factor Analysis

8.1 The $K_L \rightarrow e^+e^-e^+e^-$ Form Factor

This chapter discusses the first measurement of the $K_L\gamma^*\gamma^*$ form factor using the decay $K_L \rightarrow e^+e^-e^+e^-$. The details of this form factor were discussed in chapter 1; we present here a summary of that discussion. The $K_L \rightarrow e^+e^-e^+e^-$ form factor illuminates us of the internal structure of the long lived neutral kaon and gives us information about the $K_L \rightarrow \gamma^*\gamma^*$ vertex. The decay $K_L \rightarrow e^+e^-\gamma$ probes the $K_L \rightarrow \gamma\gamma^*$ form factor and has been parametrized by Bergström, Massó, and Singer [1]. The expression for the form factor that comes from the BMS model is [1],[32]:

$$f(x) = \frac{1}{1 - 0.418x} + \frac{2.3\alpha_{K^*}}{1 - 0.308x} \left[\frac{4}{3} - \frac{1}{1 - 0.418x} - \frac{1}{9(1 - 0.405x)} - \frac{2}{9(1 - 0.238x)} \right]. \quad (8.1)$$

In this equation α_{K^*} is the parameter describes the relative strength of an intermediate pseudoscalar decay amplitude and a vector meson decay amplitude with x defined as M_{ee}^2/M_K^2 . Since there is no theoretical model of the form factor in $K_L \rightarrow e^+e^-e^+e^-$ we have applied the model for the decay $K_L \rightarrow e^+e^-\gamma$ to $K_L \rightarrow e^+e^-e^+e^-$. In $K_L \rightarrow e^+e^-e^+e^-$, there are two internal pair productions to e^+e^- so we use a factorized expression for the form factor:

$$F(x_1, x_2) = f(x_1) \cdot f(x_2). \quad (8.2)$$

We also fit for the form factor parametrized by D'Ambrosio, Isidori and Portolés (DIP):

$$f(q_1^2, q_2^2) = 1 + \alpha_{DIP} \left[\frac{x_1}{x_1 - 2.4} + \frac{x_2}{x_2 - 2.4} \right] + \beta_{DIP} \frac{x_1 x_2}{(x_1 - 2.4)(x_2 - 2.4)}, \quad (8.3)$$

where $q = M_{ee}$, and α_{DIP} , β_{DIP} are arbitrary real parameters for a ρ form factor. This parametrization of the $K_L \rightarrow \gamma^* \gamma^*$ process is relatively model independent.

Another model independent form factor we fit for has a simple linear form:

$$f(x) = 1 + \alpha_{Taylor} \cdot x, \quad (8.4)$$

where $x = M_{ee}^2/M_K^2$. Again, we use a factorized expression as in equation 8.2, since we have two e^+e^- pairs in the final state.

8.1.1 Fitting for the BMS Form Factor

We first inspected the distribution $x_1 + x_2$ to visually ascertain the presence of a form factor. Figure 8.1 shows the $x_1 + x_2$ distribution for data (dots) and Monte Carlo with $f(x) = 1$ or a flat form factor and KTeV MC radiative corrections [83]. This plot shows that the overall shapes of the data and MC distributions are different, indicating the presence of a non flat or pointlike form factor in the $K_L \rightarrow e^+e^-e^+e^-$ data. The data in this analysis included the cuts as discussed in chapter 6.

To find the value of α_{K^*} for our $K_L \rightarrow e^+e^-e^+e^-$ data we generated several different correlated Monte Carlo samples with different values of α_{K^*} and for each sample formed a χ^2 with the data. Our measurement of α_{K^*} was the one that gave the minimum χ^2 . The statistical error came from a change of one unit in the minimum χ^2 . However, a slightly better technique was to use a likelihood analysis which depended on all kinematic variables (not just x_1 and x_2) and was also independent of binning. The details of this technique is discussed in appendix A. The log likelihood method was taken as our default method and the χ^2 method was used as a cross-check.

Radiative corrections could potentially have a large effect on the form factor measurement, since the M_{ee} distribution is the distribution most sensitive to the form factor. Therefore, our final measurement excluded radiative corrections since the radiative corrections currently available for $K_L \rightarrow e^+e^-e^+e^-$ does not simulate all higher order terms which could affect this measurement. Hence, we measured an effective parameter, $\alpha_{K^*}^{\text{eff}}$ which takes into account both the form factor and radiative effects. This effect of radiative corrections on the form factor has been observed before in the

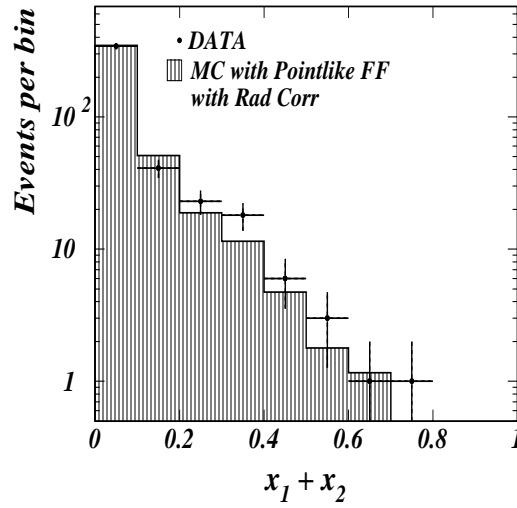


Figure 8.1: This plot shows the distribution of $x_1 + x_2$. In this plot the dots represent the data and the histogram represents the MC with $f(x) = 1$ or a pointlike form factor and KTeV MC radiative corrections included. The overall shapes of the data and MC distributions are different indicating the presence of a non flat form factor in the $K_L \rightarrow e^+e^-e^+e^-$ data. This distribution is used for fitting for α_{K^*} using a Poisson χ^2 . Here, the χ^2 between data and MC is 7.3 out of 3 dof.

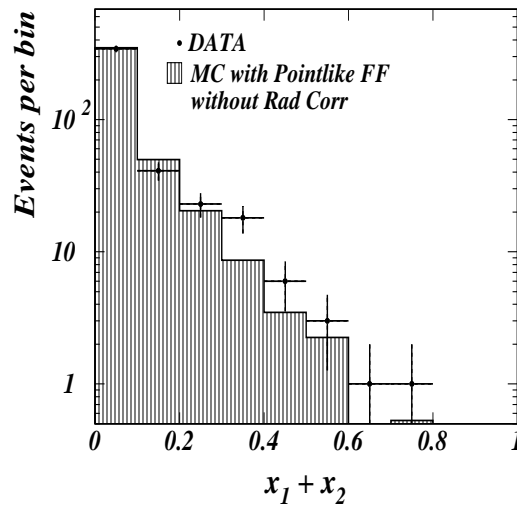


Figure 8.2: The distribution of $x_1 + x_2$. In this plot the dots represent the data and the histogram represents the MC with $f(x) = 1$ or a pointlike form factor and radiative corrections are excluded. Here, the χ^2 between data and MC is 11.2 out of 3 dof. Comparing this to figure 8.1 shows that radiative corrections affect this distribution.

decay $K_L \rightarrow e^+e^-\gamma$. The recent measurement of $\alpha_{K^*}^{\text{eff}} = -0.15 \pm 0.06_{\text{stat}} \pm 0.02_{\text{syst}}$ for the decay $K_L \rightarrow e^+e^-\gamma$ [42] also ignores radiative corrections. Including radiative corrections to $K_L \rightarrow e^+e^-\gamma$, $\alpha_{K^*} = -0.36 \pm 0.06_{\text{stat}} \pm 0.02_{\text{syst}}$ [42]. However, the effect of radiative corrections on α_{K^*} could well be different in the two modes. Figure 8.2 shows the $x_1 + x_2$ distribution for data (dots) and Monte Carlo with $f(x) = 1$ or a flat form factor and no radiative corrections. Comparing this to figure 8.1 shows that radiative corrections affect this distribution.

Before extracting the answer from the data, 10 different MC samples the size of the data were analyzed and fit for α_{K^*} . A known value of α_{K^*} equal to -0.36 (as in the measurement in [42]) was simulated in these MC data sets, so fitting for the parameter helped us evaluate biases, if any, and verify the size of the statistical error. Figure 8.3 shows the fit value of α_{K^*} with the statistical error from the fit for the 10 samples. A fit to a line gives -0.426 ± 0.050 , so we reproduce the value of α_{K^*} put in the MC to within around 1σ . We also know from this figure that our statistical error for α_{K^*} will be approximately 0.16. Figure 8.4 shows the distribution of the fit value minus the expected value of -0.36. This distribution is then fit to a Gaussian. The mean of this distribution is 0.01 ± 0.05 , indicating no bias at the level of expected statistical error from data. Both plots show how well this technique reproduced the expected value of -0.36.

Now that we have shown that we are able to measure α_{K^*} without any biases and know the order of our statistical error, we fit the data. Our result from the data is shown in figures 8.5 and 8.6. These figures show the log likelihood as a function of α_{K^*} for the $K_L \rightarrow e^+e^-e^+e^-$ data. The MC terms in the likelihood were calculated with and without radiative corrections. The range of values of the parameter is from -0.8 to 0.6. Maximizing the log likelihood gives a value for α_{K^*} of $0.03 \pm 0.17_{\text{stat}}$ and $\alpha_{K^*}^{\text{eff}}$ of $-0.14 \pm 0.16_{\text{stat}}$, with and without radiative corrections in the MC, respectively. A cross-check of these measurements using the χ^2 method can be found in appendix B.

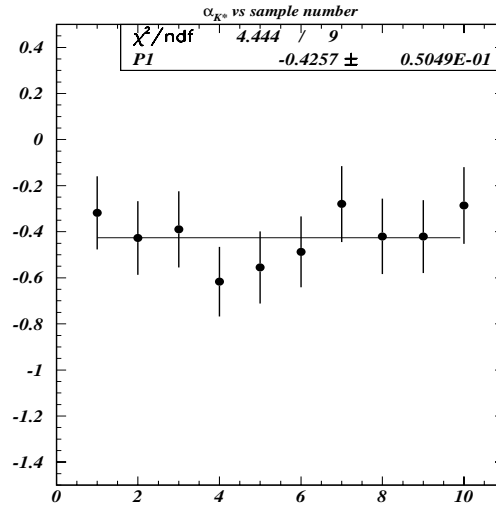


Figure 8.3: This plot shows the fit value of α_{K^*} from the log likelihood with the statistical error from the fit for the 10 MC samples the size of data. The MC samples contain a value of α_{K^*} of -0.36 and we fit -0.43 ± 0.05 (this is a factor of $\sqrt{10}$ less than our data statistics error). This indicates no significant bias in the technique at the level of expected statistical error from data.

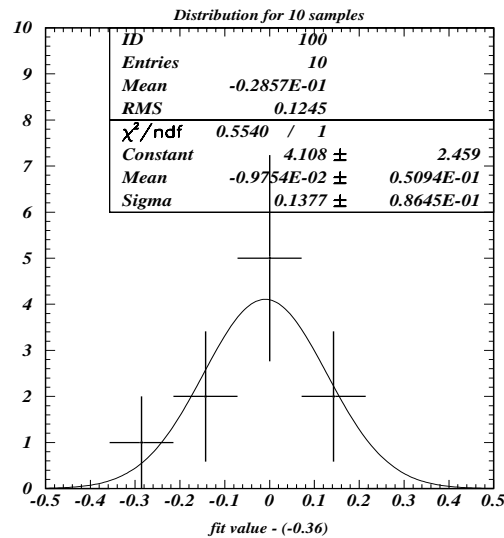


Figure 8.4: The distribution of the fit value from the log likelihood minus the expected value of -0.36. This distribution is then fit to a Gaussian. We see the mean centered about zero and the sigma (RMS) is an indication of our expected data statistics error. This indicates that there is no bias in the technique at the level of expected statistical error from data.

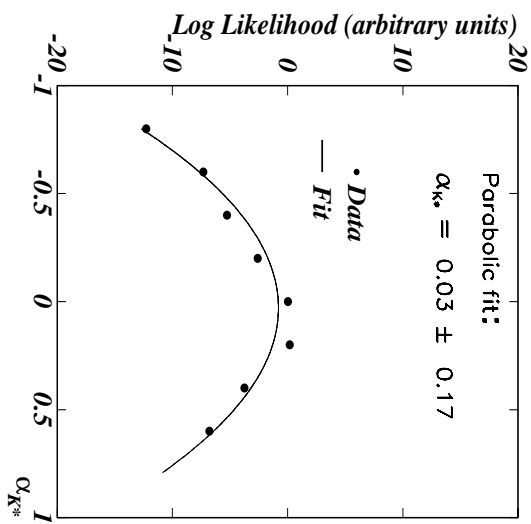


Figure 8.5: This plot shows the log likelihood as a function of α_{K^*} for the $K_L \rightarrow e^+e^-e^+e^-$ data. Radiative corrections are included in the MC. Maximizing the log likelihood gives a value for α_{K^*} of $0.03 \pm 0.17_{\text{stat}}$.

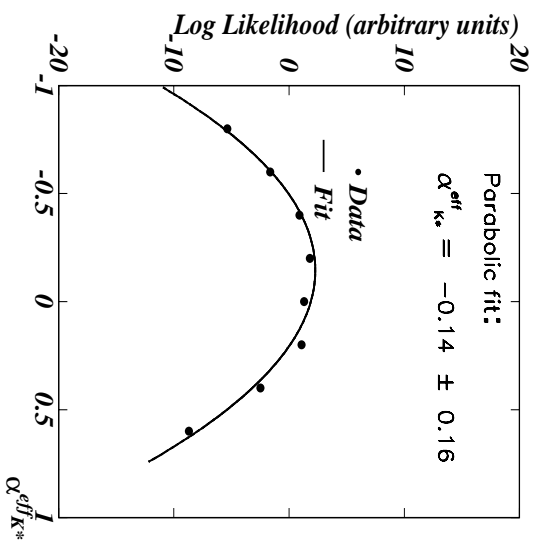


Figure 8.6: This plot shows the log likelihood as a function of $\alpha_{K^*}^{\text{eff}}$ for the $K_L \rightarrow e^+e^-e^+e^-$ data. Radiative corrections have been excluded in the MC. Maximizing the log likelihood gives a value for $\alpha_{K^*}^{\text{eff}}$ of $-0.14 \pm 0.16_{\text{stat}}$.

8.1.2 Fitting for the DIP Form Factor

As mentioned in chapter 1, in $K_L \rightarrow e^+e^-e^+e^-$, only the first order term in the DIP form factor parametrization (α_{DIP}) is relevant, as can be seen in equation 8.3. Due to the dominance of low M_{ee} , we do not expect to be sensitive to the second order term (β_{DIP}).

Neglecting the second order term we get the relation $\alpha_{\text{DIP}} = -1 + 2.8 \alpha_{K^*}$, where α_{K^*} is the BMS parameter described above. Therefore, our expected measurement of α_{DIP} , neglecting the β_{DIP} term, using our measurement of $\alpha_{K^*}(\alpha_{K^*}^{\text{eff}})$ above is $-0.9(-1.1)$ using the log likelihood method. Figures 8.7 and 8.8 show the fit results from the data using the log likelihood method with and without radiative corrections in the MC. The log likelihood results gives $\alpha_{\text{DIP}} = -0.9 \pm 0.5$ and $\alpha_{\text{DIP}}^{\text{eff}} = -1.1 \pm 0.6$ as expected from the α_{K^*} and $\alpha_{K^*}^{\text{eff}}$ measurements. The results using the χ^2 method are given in appendix C.1. Comparing the results of the two methods, we see that the log likelihood method is a slightly more sensitive method as we saw before when fitting for the BMS form factor. In appendix C.2 we present studies of the DIP form factor including the quadratic term β_{DIP} .

8.1.3 Fitting for a Linear Form Factor

A first order Taylor expansion of the $K_L \rightarrow e^+e^-e^+e^-$ form factors yields a generic linear form factor of the form $(1 + \alpha_{\text{Taylor}}(x_1 + x_2))$ as described in chapter 1. We obtain the approximate relations $\alpha_{\text{Taylor}} \approx 0.42 - 1.2\alpha_{K^*} \approx -\alpha_{\text{DIP}}/2.4$. Our expectations and measurements of α_{Taylor} are summarized in tables 8.1 and 8.2 respectively. We see that our measurements of α_{Taylor} and $\alpha_{\text{Taylor}}^{\text{eff}}$ agree with the expected values from our BMS and DIP form factor measurements. The results using the χ^2 method are given in appendix D.

8.1.4 Sources of Systematic Error for the $K_L \rightarrow e^+e^-e^+e^-$ Form Factor

We are taking the measurement of the BMS form factor parameter as our standard result, therefore, all the studies of the sources of systematic error for the form factor

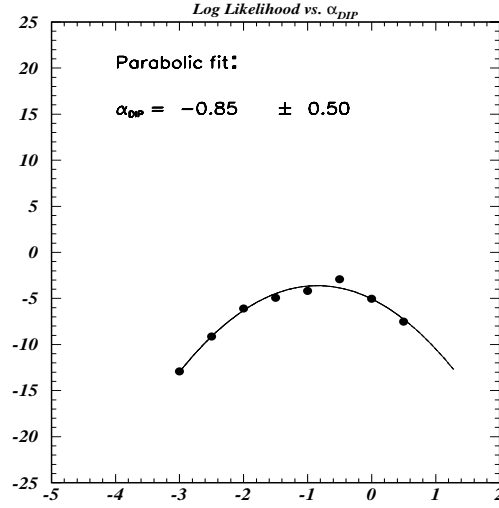


Figure 8.7: This plot shows the log likelihood as a function of the DIP form factor parameter α_{DIP} (with $\beta_{DIP} = 0.0$) for the $K_L \rightarrow e^+e^-e^+e^-$ data. Maximizing the log likelihood gives a value for α_{DIP} of $-0.9 \pm 0.5_{\text{stat}}$.

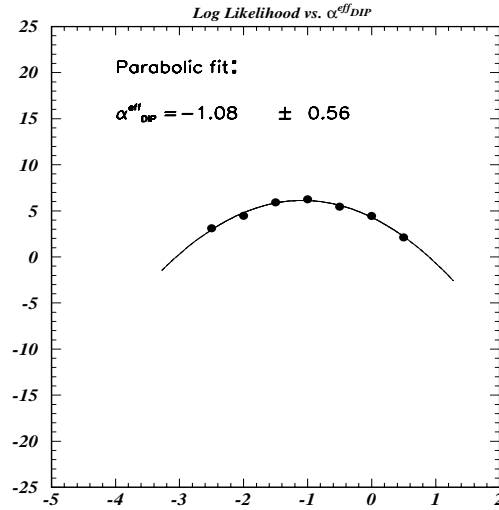


Figure 8.8: This plot shows the log likelihood as a function of the DIP form factor parameter α_{DIP}^{eff} (with $\beta_{DIP} = 0.0$) for the $K_L \rightarrow e^+e^-e^+e^-$ data. Maximizing the log likelihood gives a value for α_{DIP}^{eff} of $-1.1 \pm 0.6_{\text{stat}}$.

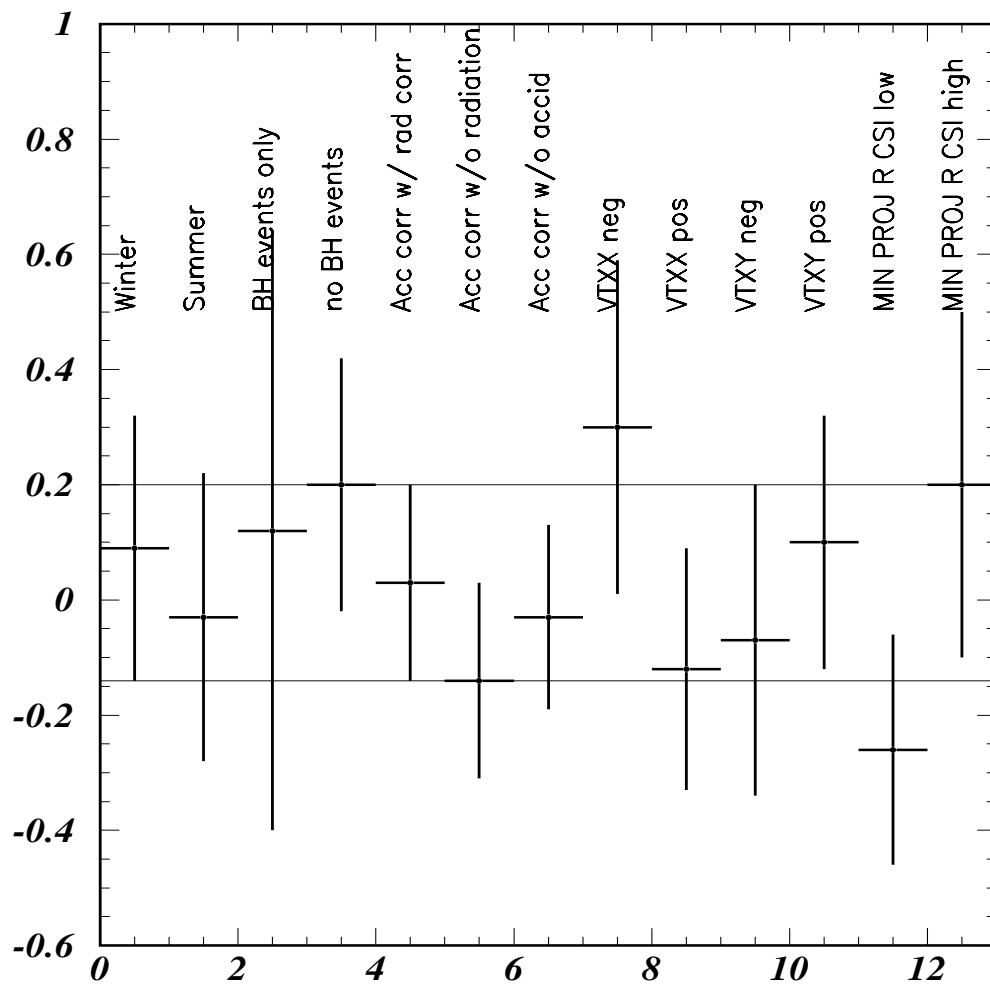


Figure 8.9: Systematic checks for α_{K^*} . The data was split into two different samples and fit for the parameter. We also fit for the parameter using different MC for acceptance correction. The horizontal lines show the size of the statistical error of our measurement of α_{K^*} .

Table 8.1: Expected values of α_{Taylor} from measurements of α_{K^*} and α_{DIP} using the log likelihood method.

	Expected α_{Taylor} and $\alpha_{\text{Taylor}}^{\text{eff}}$
α_{K^*}	0.38
α_{DIP}	0.35
$\alpha_{K^*}^{\text{eff}}$	0.58
$\alpha_{\text{DIP}}^{\text{eff}}$	0.45

Table 8.2: Measurements of α_{Taylor} and $\alpha_{\text{Taylor}}^{\text{eff}}$ using the log likelihood method. These measurements agree with the expected values from our BMS and DIP form factor measurements seen in table 8.1.

	log likelihood method
α_{Taylor}	0.34 ± 0.27
$\alpha_{\text{Taylor}}^{\text{eff}}$	0.50 ± 0.27

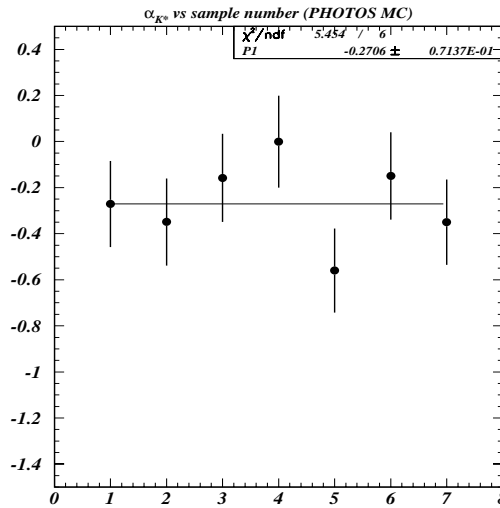


Figure 8.10: This plot shows the fit value of α_{K^*} from the χ^2 method with the statistical error from the fit for the 7 MC samples the size of data that contain PHOTOS. The MC samples were generated with α_{K^*} of 0.0. The MC comparison included PHOTOS. We observe an unexplained bias of -0.27 units in α_{K^*} .

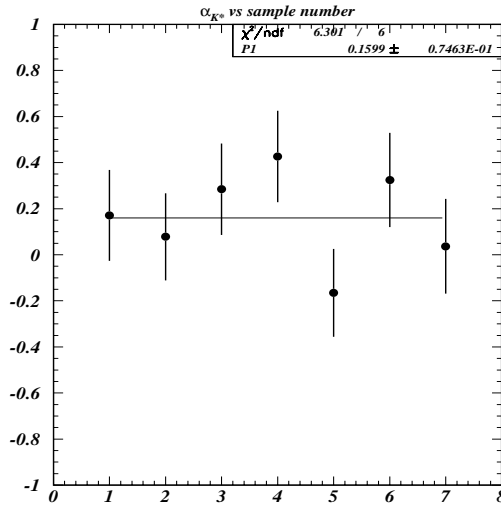


Figure 8.11: This plot shows the fit value of α_{K^*} from the χ^2 method with the statistical error from the fit for the 7 MC samples the size of data that contain PHOTOS. The MC samples were generated with α_{K^*} of 0.0. The MC comparison included radiative corrections using KTeV MC. The difference in this fit for α_{K^*} is about 80% of the statistical error of our measurement.

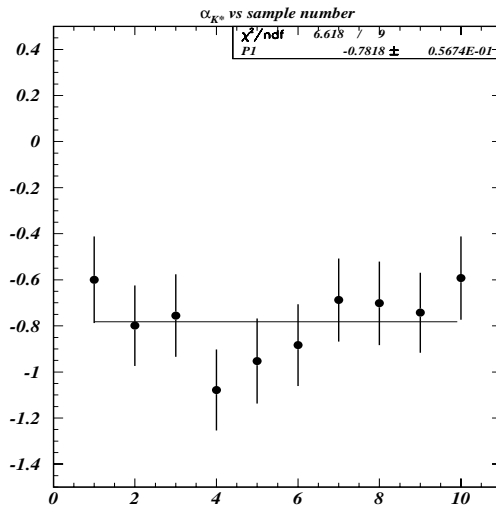


Figure 8.12: This plot shows the fit of α_{K^*} with the statistical error from the fit for the 10 samples using χ^2 . The MC samples contain a value of α_{K^*} of -0.36 and were generated with KTeV MC radiative corrections. The MC comparison included radiative corrections using PHOTOS. We observe a bias of -0.42 units in α_{K^*} . Compare this figure to figure B.1, where we have used KTeV MC radiative corrections in the χ^2 comparison.

were performed assuming this parametrization. Various systematic checks were done by splitting the data up into different samples. In figure 8.9 we see the fits for α_{K^*} when we looked at the winter vs. the summer data; events when one of the four tracks went down the beam hole at the CsI and when no tracks go down the beam hole at the CsI; events that came from the east beam vs. the west beam; events that came from the top of the beam vs. the bottom of the beam; events where we have taken the minimum radial distance of a track projected at the CsI. These plots also show how these parameters vary for different Monte Carlos used in the acceptance correction. For the purposes of systematic studies, we analyzed a MC sample generated without radiative corrections and a MC with no accidental overlays and no radiative corrections. All the error bars in figure 8.9 are statistical. All points in this figure are consistent with each other. This gives us confidence that the systematic uncertainty is not larger than the statistical error.

Next different variables were intentionally scaled thus inducing artificial slopes in data vs. MC comparisons which were used to assign the systematic error. Table 8.3 shows how systematic errors were assigned by scaling. Also, the track momenta and the cluster energies were smeared to get a better understanding of how the uncertainty in the detector (DC, CsI) resolutions affect the fit to α_{K^*} . We found that the uncertainties in the detector resolutions do not affect the fit to the form factor parameter.

To further study the issue of radiative corrections we generated 7 samples of MC the size of our data sample with PHOTOS and with $\alpha_{K^*} = 0.0$. We then fit for α_{K^*} to see how well we can extract what we put in. Again, this gives a rough indication of any systematic biases. For simplicity we used the χ^2 method in these studies. The fit in figure 8.10 indicates a bias of -0.27 units in α_{K^*} . This unexplained bias is most likely due to the fact that since PHOTOS is a package that was added on to the KTeV MC, the matrix element [24] was calculated in our MC and after the event was generated, PHOTOS modified the e^\pm four-vectors if a photon was radiated. The KTeV MC radiative corrections simulation, on the other hand, calculated the matrix element for all the different diagrams it is capable of simulating, tree-level [24] and radiative [83], and then the event was generated (similar to what is found in [84]). We were not

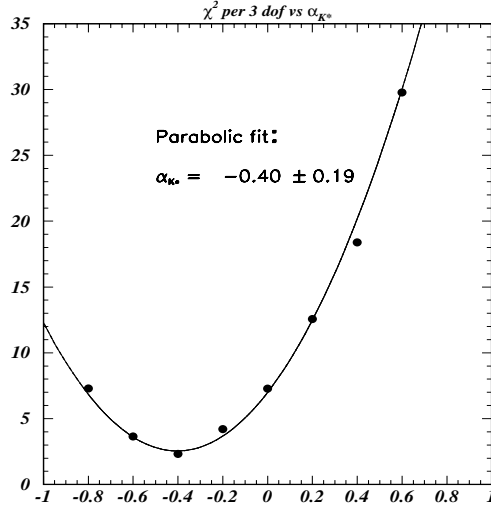


Figure 8.13: This plot shows the Poisson χ^2 as a function of α_{K^*} for the $K_L \rightarrow e^+e^-e^+e^-$ data. Radiative corrections using PHOTOS are included in the MC. Minimizing the χ^2 gives a known biased value for α_{K^*} of $-0.40 \pm 0.19_{\text{stat}}$.

Table 8.3: Form Factor Systematic Studies

Distrib.	orig. slope % per quantity	$\Delta\alpha_{K^*}/\Delta$ slope % per quantity	Systematic error assigned
VTXZ (m)	-0.31 ± 0.29	0.12/0.30	0.12
ENERGCS sum (GeV)	-0.14 ± 0.16	-0.07/0.13	0.09
TRKP sum (GeV)	-0.40 ± 0.21	-0.01/0.29	0.01

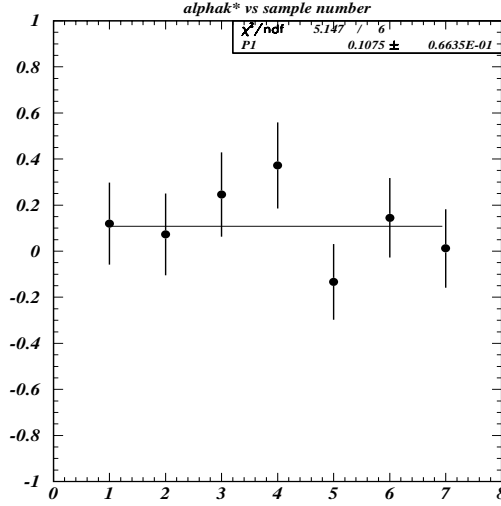


Figure 8.14: This plot shows the fit value of α_{K^*} from the log likelihood with the statistical error from the fit for the 7 MC samples the size of data that contain PHOTOS. The MC samples also have α_{K^*} of 0.0. The difference in this fit for α_{K^*} is about 60% of the statistical error of our measurement.

concerned with this bias since all other studies resulted in consistent answers. We also fit these same 7 samples using the KTeV MC radiative corrections in the χ^2 comparison; the result is shown in figure 8.11. Again we observe a bias of -0.16 units in α_{K^*} . Finally, we fit our 10 original MC samples the size of data that were generated using the KTeV MC radiative corrections with a value of $\alpha_{K^*} = -0.36$ and used PHOTOS in the MC for the χ^2 comparison; the result is shown in figure 8.12. We observe a bias of -0.42 units in α_{K^*} . Compare this figure to figure B.1, where we have used KTeV MC radiative corrections in the χ^2 comparison. We fit our data using PHOTOS in the MC in the χ^2 comparison as seen in figure 8.13. Removing the -0.27 unit bias, the difference between this measurement and the one with the KTeV MC radiative corrections ($\alpha_{K^*} = -0.02 \pm 0.20$) is 0.11 ± 0.10 , where the error is the uncorrelated error due to MC statistics in the two results.

These studies with PHOTOS verify the sensitivity of the form factor to radiative corrections in general. This further justifies the measurement of an *effective* form factor, which parametrizes both the form factor and radiative effects. This parametrization

Table 8.4: Table of Errors for Form Factor Measurements. Recall that $\alpha_{K^*}^{\text{eff}}$ incorporates radiative effects.

Error		in $\alpha_{K^*}^{\text{eff}}$	in α_{K^*}
<i>Statistics</i>		0.16	0.17
<i>Systematic:</i>			
	Detector Acceptance/Spectrum	0.15	0.15
	Detector Resolution	-	-
	Time Dependence	-	-
	Accidentals	-	-
	Radiative Corrections	-	0.11
	<i>total internal systematic</i>	0.15	0.18

eliminated the need for assigning systematic error due to the uncertainty in the radiative corrections. However, we estimated the systematic error of radiative corrections on our measurement of α_{K^*} of 0.03 (log likelihood method), when radiative corrections were included. We also fit the PHOTOS generated samples the size of data with $\alpha_{K^*} = 0.0$ using the KTeV MC radiative corrections in the log likelihood MC terms; the result is shown in figure 8.14. The difference in this fit for α_{K^*} is about 60% of the statistical error of our measurement. This difference of 0.11 is assigned as a conservative estimate of the systematic error of α_{K^*} due to radiation.

We summarize the errors on $\alpha_{K^*}^{\text{eff}}$ and α_{K^*} in table 8.4.

8.1.5 Results of the $K_L \rightarrow e^+e^-e^+e^-$ Form Factor

We measured

$$\alpha_{K^*}^{\text{eff}} = -0.14 \pm 0.16_{\text{stat}} \pm 0.15_{\text{syst}}, \quad (8.5)$$

in $K_L \rightarrow e^+e^-e^+e^-$, where $\alpha_{K^*}^{\text{eff}}$ incorporates the BMS parameterization of the form factor and radiative effects. This result excludes radiative corrections in the MC. Figure 8.15 shows the $x_1 + x_2$ distribution for data (dots) and Monte Carlo with $\alpha_{K^*}^{\text{eff}} = -0.14$, our measured value. This shows better agreement with the data compared to figure 8.2, with a pointlike form factor.

Disentangling radiative corrections, we extract the pure form factor measurement

$$\alpha_{K^*} = 0.03 \pm 0.17_{\text{stat}} \pm 0.18_{\text{syst}}. \quad (8.6)$$

We also show the $x_1 + x_2$ distribution for data (dots) and Monte Carlo with $\alpha_{K^*} = 0.03$, our measured value including radiative corrections in figure 8.16. This also shows better agreement with the data compared to figure 8.1, with a pointlike form factor and radiative corrections included in the MC.

This is the first measurement of the $K_L \gamma^* \gamma^*$ form factor using $K_L \rightarrow e^+ e^- e^+ e^-$. For reference, the PDG world average of the $K_L \gamma \gamma^*$ form factor using $K_L \rightarrow e^+ e^- \gamma$ is:

$$\alpha_{K^*} = -0.33 \pm 0.05.$$

Our result is in agreement with the recent measurement of $\alpha_{K^*}^{\text{eff}} = -0.15 \pm 0.06_{\text{stat}} \pm 0.02_{\text{syst}}$ for the decay $K_L \rightarrow e^+ e^- \gamma$ [42], also obtained by ignoring radiative corrections. Including radiative corrections to $K_L \rightarrow e^+ e^- \gamma$, $\alpha_{K^*} = -0.36 \pm 0.06_{\text{stat}} \pm 0.02_{\text{syst}}$ [42]. As mentioned before, the effect of radiative corrections on α_{K^*} could be different in the two modes.

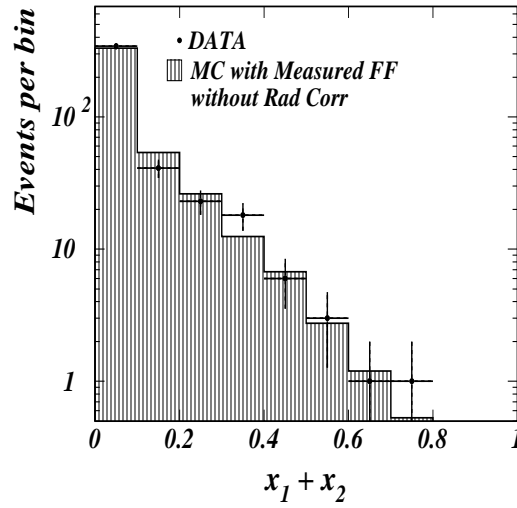


Figure 8.15: This plot shows the distribution of $x_1 + x_2$. In this plot the dots are the data and the histogram is the Monte Carlo with $\alpha_{K^*}^{\text{eff}} = -0.14$, our measured value. This shows better agreement with the data compared to figure 8.2, where a pointlike form factor was assumed. Here, the χ^2 between data and MC is 5.1 out of 3 dof, a much better agreement than in figure 8.2.

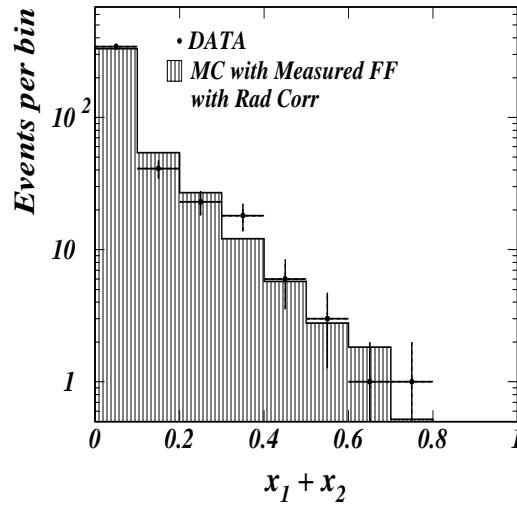


Figure 8.16: Same distribution as in figure 8.15 above. In this plot the dots are the data and the histogram is the Monte Carlo with $\alpha_{K^*} = 0.03$, our measured value. This shows better agreement with the data compared to figure 8.1, where a pointlike form factor was assumed. Here, the χ^2 between data and MC is 5.8 out of 3 dof, a much better agreement than in figure 8.1.

Chapter 9

Branching Ratio Analysis

9.1 The Branching Ratio of $K_L \rightarrow e^+e^-e^+e^-$

To measure the $K_L \rightarrow e^+e^-e^+e^-$ branching ratio, the events were normalized to $K_L \rightarrow \pi^0\pi_D^0\pi_D^0$. The normalization mode was used to measure how many total K_L decays occurred in the KTeV experiment. The branching ratio is then defined as the ratio of the number of times the K_L decayed to $e^+e^-e^+e^-$ to the total number of K_L decays.

Since we now have clean signal and normalization samples with minimal background and have shown that the data and Monte Carlo matches at a fair level it is time to measure the branching ratio of this decay. The $K_L \rightarrow e^+e^-e^+e^-$ branching ratio is given by:

$$B(K_L \rightarrow e^+e^-e^+e^-) = B(K_L \rightarrow \pi^0\pi_D^0\pi_D^0) \frac{N_{K_L \rightarrow e^+e^-e^+e^-}}{N_{K_L \rightarrow \pi^0\pi_D^0\pi_D^0}} \frac{A_{K_L \rightarrow \pi^0\pi_D^0\pi_D^0}}{A_{K_L \rightarrow e^+e^-e^+e^-}}, \quad (9.1)$$

where N stands for the number of events for that decay with background subtracted and A is the acceptance of that decay from Monte Carlo.

The number of observed signal events in the entire E799II data set is 441 with 4.2 background events and the number of normalization events ($K_L \rightarrow \pi^0\pi_D^0\pi_D^0$) is 49089 with 865 background events. The signal acceptance is $(4.51 \pm 0.05_{\text{stat}})\%$ and the normalization acceptance is $(0.206 \pm 0.001_{\text{stat}})\%$, where the errors are due to limited MC statistics. The signal acceptance has been calculated without radiative corrections and with $\alpha_K^{\text{eff}} = -0.14$, our measured effective form factor. These numbers yield:

$$B(K_L \rightarrow e^+e^-e^+e^-) = (3.72 \pm 0.18_{\text{data stat}} \pm 0.04_{\text{mc stat}}) \times 10^{-8}. \quad (9.2)$$

9.1.1 Systematic Error Estimates for $B(K_L \rightarrow e^+e^-e^+e^-)$

QED Radiative Corrections and Form Factor

When the signal acceptance was calculated with radiative corrections and with $\alpha_{K^*} = 0.03$, our measured form factor the branching ratio becomes:

$$B(K_L \rightarrow e^+e^-e^+e^-) = (3.64 \pm 0.17_{\text{data stat}} \pm 0.05_{\text{mc stat}}) \times 10^{-8}.$$

This number is different from the value above (equation 9.2) by 0.08 ± 0.06 in units of 10^{-8} of the branching ratio, where the error is the uncorrelated error between the two values. The $B(K_L \rightarrow e^+e^-e^+e^-)$ as a function of $\alpha_{K^*}^{\text{eff}}$ and α_{K^*} is shown in figures 9.1 and 9.2. To estimate the systematic error due to $\alpha_{K^*}^{\text{eff}}$ on the branching ratio measurement above 9.2, we varied $\alpha_{K^*}^{\text{eff}}$ by our measured uncertainty of ± 0.23 . This yielded a systematic uncertainty in the $K_L \rightarrow e^+e^-e^+e^-$ branching ratio of 0.9% or 0.03×10^{-8} , due to $\alpha_{K^*}^{\text{eff}}$, the combined effect of the uncertainty in the radiative corrections and the form factor.

We also show that the addition of final state bremsstrahlung in the Monte Carlo simulation does not affect this result significantly. As previously described, until recently, the PHOTOS package [82] was the only simulation we had for radiative corrections for the signal mode. We also had an internal simulation package [83]. The differences between the two simulations are described in section 5.6. In the case of generating normalization mode MC with radiative corrections, we also had a choice of using the PHOTOS package or using the the QED calculated radiative corrections [84] again described in section 5.6. Using data versus MC studies, we showed that both Monte Carlo simulations of the radiative corrections simulated the data well (see chapter 6). Table 9.1 shows the $B(K_L \rightarrow e^+e^-e^+e^-)$ with and without radiative corrections in the MC acceptance and that the results are consistent. In addition, all MC samples used in this study were generated with a pointlike form factor, $f(x) = 1$. There is a $(0.05 \pm 0.08) \times 10^{-8}$ difference between PHOTOS and KTeV MC radiative corrections, a $(0.08 \pm 0.09) \times 10^{-8}$ difference between KTeV MC radiative corrections and no radiative corrections, and a $(0.03 \pm 0.09) \times 10^{-8}$ difference between PHOTOS and no radiative corrections.

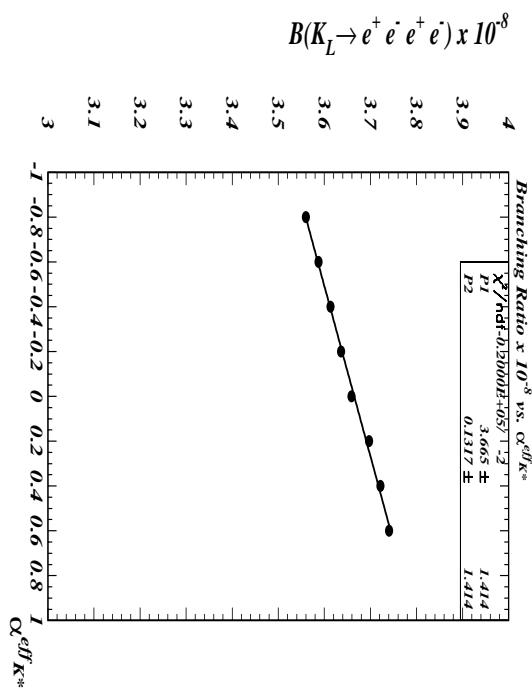


Figure 9.1: $B(K_L \rightarrow e^+ e^- e^+ e^-) \times 10^{-8}$ vs. $\alpha_{K^*}^{\text{eff}}$. A fit to a straight line is shown. The errors on P1 and P2 (intercept and slope, respectively) should be ignored; we assumed no errors on the points since they are all correlated.

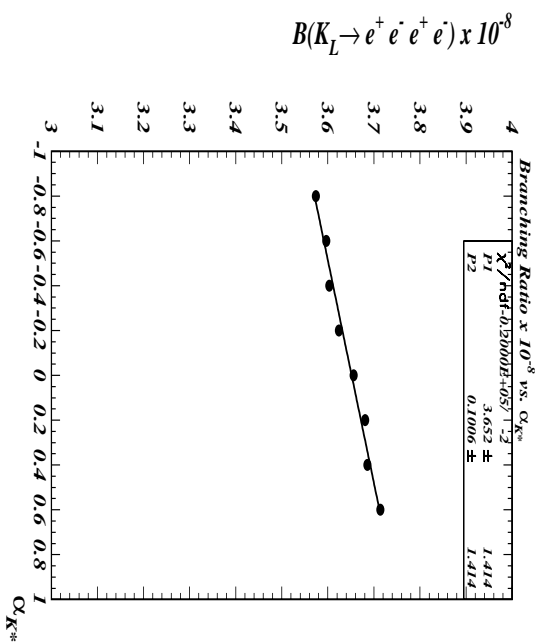


Figure 9.2: $B(K_L \rightarrow e^+ e^- e^+ e^-) \times 10^{-8}$ vs. α_{K^*} . A fit to a straight line is shown. The errors on P1 and P2 (intercept and slope, respectively) should be ignored; we assumed no errors on the points since they are all correlated.

Table 9.1: Branching Ratio with and without Radiative corrections in MC Acceptance. The MC errors in this table are uncorrelated. These results are consistent.

MC used for Acceptance	B ($\times 10^{-8}$)	data stat	MC stat
KTeV MC rad corr	3.73	0.18	0.06
PHOTOS	3.78	0.18	0.06
No rad corr	3.81	0.18	0.07

“Two-part” Studies

To have a global understanding of the total internal systematic error we split the data into two subsets using various criteria and compared the branching ratios for the two subsets. Examples of such criteria are two time periods, east beam vs. west beam, etc. In cases where it was necessary to find the midpoint of the distribution the normalization mode, $K_L \rightarrow \pi^0 \pi_D^0 \pi_D^0$, was used. Neglecting correlations between the various criteria, the spread in the different measurements is an indicator of the systematic spread. We used this technique as a diagnostic tool to get a qualitative understanding of the systematic effects.

From figures 9.3 through 9.6 we see that the spread is consistent with the statistical error. Figures 9.3 and 9.5 show the measurement for each subset versus the criteria. Figures 9.4 and 9.6 show the spread of the measurements. This gives confidence that the systematic error of the branching ratio is small, on the scale of the statistical error, due to detector understanding.

In addition to splitting the data up as just described, it was also split between the winter and summer data and no significant change in the branching ratio was seen. The data was also split into events where no tracks were allowed to go down the beam hole and events where one track was required to go down the beam hole. Again, there was no significant difference in the branching ratio between these two subsets of data.

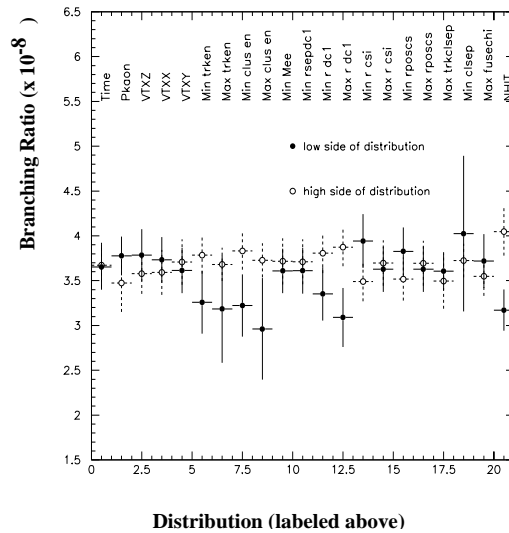


Figure 9.3: “Two-part” study. Data was split into two subsets using various criteria (labeled above) and compare the branching ratios for the two subsets. Examples of such criteria are two time periods, east beam vs. west beam, etc. In cases where was necessary to find the midpoint of the distribution the normalization mode, $K_L \rightarrow \pi^0 \pi_D^0 \pi_D^0$, was used. Neglecting correlations between the various criteria, the spread in the different measurements is an indicator of the systematic spread. We are using this technique as a diagnostic tool to get a qualitative understanding of the systematic effects.

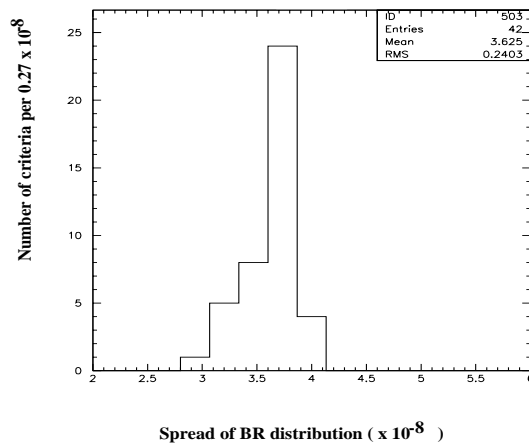


Figure 9.4: Spread of the distribution of the “two-part” study. This is the spread of the distributions in figure 9.3. This gives confidence that the systematic error of the branching ratio is small, on the scale of the statistical error, due to detector understanding.

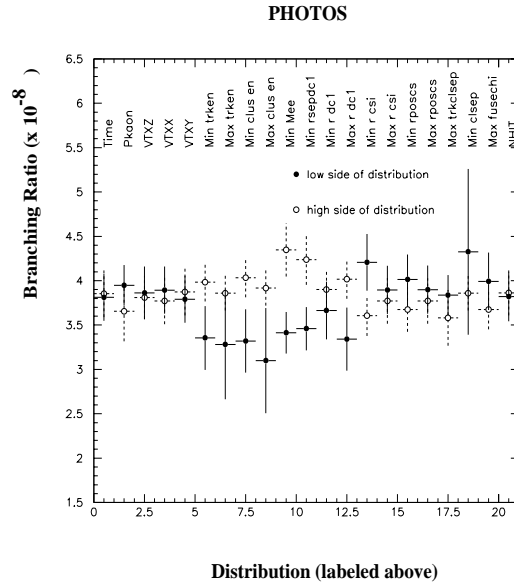


Figure 9.5: “Two-part” study using PHOTOS, as in figure 9.3. We are using this technique as a diagnostic tool to get a qualitative understanding of the systematic differences between the two MC simulations. Notice that the spread here is greater than in figure 9.3.

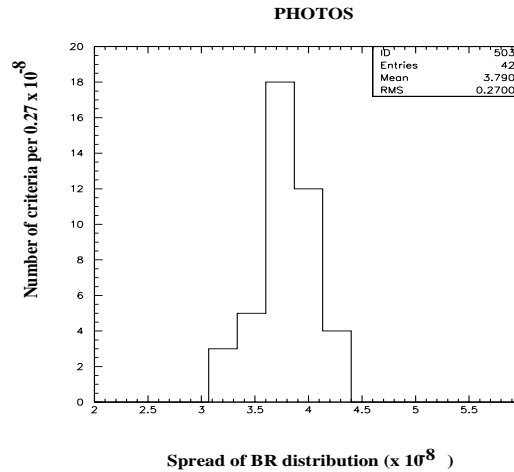


Figure 9.6: Spread of the distribution of the “two-part” study using PHOTOS. This is the spread of the distributions in figure 9.5. As with figure 9.4, this gives confidence that the systematic error of the branching ratio is small, on the scale of the statistical error, due to detector understanding. Notice that the spread, or the RMS, is greater than in figure 9.4.

Table 9.2: Branching Ratio Systematic Studies

Distrib.	original slope	slope change	B	% syst error
	% per quantity	% per quantity (arbitrary)	$\times 10^{-8}$	assigned
-	-	-	3.73	-
TRKP fudge (GeV)	-0.047 ± 0.063	0.049	3.78	1.7
ENERGCS fudge (GeV)	0.043 ± 0.019	0.051	3.67	1.3
VTXZ (m)	0.052 ± 0.037	0.178	3.78	0.39

Specific Systematic Studies

Next, we artificially scaled (fudged) the data and artificially worsened the detector resolution (smeared) in different variables thus inducing slopes in data versus MC comparisons and assigned systematic error to each of these effects. As anticipated from the two-part studies described above the systematic effects appear to be negligible and are listed in table 9.2. Since the normalization mode, $K_L \rightarrow \pi^0 \pi_D^0 \pi_D^0$, has more than a factor of 100 times statistics of $K_L \rightarrow e^+ e^- e^+ e^-$, data versus MC studies were done using this mode.

The uncertainty in the σ 's in the Mass- χ^2 procedure for selection of double-Dalitz events versus double-single-Dalitz events were also considered as a source for systematic error. The charged σ was changed by $\pm 10\%$ of itself while leaving the neutral σ 's alone and vice versa. No significant change in the branching ratio was observed.

The track momenta and the cluster energies were smeared to get a better understanding of how the uncertainty in the detector (DC, CsI) resolutions affect the branching ratio measurement. These studies yield negligible changes and thus do not contribute to the systematic error.

Finally, the $K_L \rightarrow e^+ e^- e^+ e^-$ branching ratio was measured using Monte Carlo without accidental overlays. They change the answer by less than one statistical sigma. This is not a significant change and therefore no systematic error is assigned due to accidentals.

9.1.2 Summary of Branching Ratio of $K_L \rightarrow e^+e^-e^+e^-$ Results

List of Errors

The contributions to the $B(K_L \rightarrow e^+e^-e^+e^-)$ error are summarized in table 9.3.

Table 9.3: Table of Branching Ratio Errors

Error		%
<i>Data Statistics</i>		4.8
<i>MC Statistics</i>		1.1
<i>Systematic:</i>		
	Detector Acceptance/Spectrum	2.2
	Detector Resolution	-
	Time Dependence	-
	Accidentals	-
	<i>total internal systematic</i>	2.2
<i>Rad corr and FF</i>		0.9
<i>PDG error on π_D^0</i>		5.5

Results

Using the errors in the table in the previous section (combining MC statistics, internal systematics and radiative corrections), the branching ratio of $K_L \rightarrow e^+e^-e^+e^-$ is,

$$B(K_L \rightarrow e^+e^-e^+e^-) = (3.72 \pm 0.18_{\text{stat}} \pm 0.10_{\text{syst}} \pm 0.20_{\text{norm}}) \times 10^{-8},$$

where “norm” refers to the measurement uncertainty in the normalization branching ratio [10]). This result is consistent with the theoretical prediction 3.65×10^{-8} [24] and the most precise published experimental result $(3.96 \pm 0.78_{\text{stat}} \pm 0.32_{\text{syst}}) \times 10^{-8}$ [38].

The measurement of this branching ratio is the most precise so far.

Chapter 10

Angular Distribution Analysis

10.1 $K_L \rightarrow e^+e^-e^+e^-$ Angular Distribution

This section describes how we studied possible CP violating effects in the decay $K_L \rightarrow e^+e^-e^+e^-$ by studying ϕ , the angle between the planes of the two e^+e^- pairs. When we introduce CP violation the decay rate of $K_L \rightarrow e^+e^-e^+e^-$ can be written as

$$\frac{d, (K_L \rightarrow e^+e^-e^+e^-)}{d\phi} \propto (1 + \beta_{\text{CP}} \cos(2\phi) + \gamma_{\text{CP}} \sin(2\phi)) \quad (10.1)$$

with

$$\beta_{\text{CP}} = -\frac{1 - |\epsilon r|^2}{1 + |\epsilon r|^2} B \approx B \quad , \quad \gamma_{\text{CP}} = \frac{2\text{Re}(\epsilon r)}{1 + |\epsilon r|^2} C \approx 2\text{Re}(\epsilon r)C, \quad (10.2)$$

where B is 0.20, ϵ measures CP violation in mixing, constant r (which is approximately unity) is the ratio of the amplitudes of K_1 and K_2 to decay to $e^+e^-e^+e^-$ and the constant C depends on the extent and nature of CP violation. There are no theoretical predictions for C. We determined the values of β_{CP} and γ_{CP} from the distribution of the angle ϕ in the $K_L \rightarrow e^+e^-e^+e^-$ events.

The angle between the e^+e^- pairs is calculated as follows:

$$\begin{aligned} \cos(\phi) &= \frac{(\vec{p}_{1+} \times \vec{p}_{1-}) \cdot (\vec{p}_{2+} \times \vec{p}_{2-})}{|\vec{p}_{1+} \times \vec{p}_{1-}| |\vec{p}_{2+} \times \vec{p}_{2-}|} \\ \sin(\phi) &= \left(\frac{(\vec{p}_{1+} \times \vec{p}_{1-})}{|\vec{p}_{1+} \times \vec{p}_{1-}|} \times \frac{(\vec{p}_{2+} \times \vec{p}_{2-})}{|\vec{p}_{2+} \times \vec{p}_{2-}|} \right) \cdot \hat{z} \end{aligned} \quad (10.3)$$

where p_{1+} and p_{1-} come from one virtual photon and p_{2+} and p_{2-} come from the other virtual photon and \hat{z} is the unit vector in the direction of one of the e^+e^- pairs in the center of mass of the kaon. We find the angle by taking the arctan(ϕ).

10.1.1 M_{ee} Dependence on Angular Distribution

The decay rate of $K_L \rightarrow e^+e^-e^+e^-$ from QED depends on the invariant mass of the e^+e^- pairs in addition to the angle ϕ [24], [25]. We integrate over all M_{ee} to get to this equation 1.21 above. Therefore, we expect the angle ϕ to have a dependence on M_{ee} .

For the purposes of this measurement, we choose the e^+e^- pairing that minimizes the product of the two e^+e^- invariant masses. The invariant mass of an internal conversion to e^+e^- peaks at zero, so we expect each M_{ee} to be very small. In reality, both pairings contribute to the matrix element since there are identical particles in the final state; the pairing we choose is the dominant contribution.

As above, the angle ϕ is defined to be the angle between the planes of the two e^+e^- pairs. In order to have two well-defined planes both opening angles must be large enough. In other words, we cut on the invariant mass of the two e^+e^- pairs, M_{ee1} and M_{ee2} . To place this cut we studied the RMS of the distribution of the generated and reconstructed difference in ϕ (in degrees) from MC studies¹. In figure 10.1 we plotted the RMS versus the value of the M_{ee} cut (in MeV). We required that M_{ee1} and M_{ee2} both be greater than $8MeV$, at which point the detector resolution in ϕ is around 1.5° . This cut was made to optimize simultaneously the detector resolution of ϕ and the statistical error.

We also checked that we can extract β_{CP} from the Monte Carlo at the generation level¹, reproducing what we input in for all M_{ee} , namely -0.20 . For this study the Monte Carlo contained the Kroll-Wada formula including the interference term [24] and included a flat or pointlike form factor. Figure 10.2 shows ϕ for all generated events. The top plot fits for β_{CP} using equation 1.21, where we have folded over angles greater than 90° into angles less than 90° since we are fitting to a cosine. We obtained the value of β_{CP} that we expect, -0.20 . The bottom plot fits for γ_{CP} using equation 1.22 and we obtain zero, as expected.

¹Generated means the point in the simulation before an event is traced through our detector; all information came purely from the physics of the decay. Reconstructed means the event was traced through the detector and was subjected to our selection criteria.

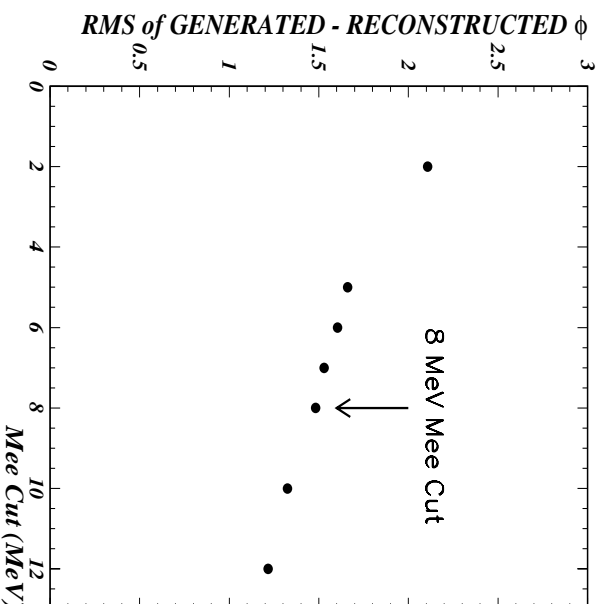


Figure 10.1: The RMS from the generated and reconstructed difference in ϕ (in degrees) from MC studies versus the value of the M_{ee} cut (in MeV). We place our M_{ee} cut at 8 MeV in the angular distribution analysis.

After testing the fitting procedure, we explored the dependence of ϕ on M_{ee} . Figure 10.3 illustrates this dependence. Using $K_L \rightarrow e^+e^-e^+e^-$ Monte Carlo we fit the angular distribution for β_{CP} and γ_{CP} in bins of M_{ee} (in MeV) at the generation level. We expect the MC to give us β_{CP} equal to -0.20 and γ_{CP} equal to zero when averaged over the whole M_{ee} range. The flat line fit of these parameters as a function of M_{ee} yielded the expected numbers. We also noticed that β_{CP} , which tests the CP state of the system, approaches zero for small M_{ee} or small opening angles of the e^+e^- pairs, where parity starts becoming undefined. Also, γ_{CP} is generated flat over the whole M_{ee} range.

We mentioned above that we required that M_{ee1} and M_{ee2} both be greater than 8 MeV . We also just showed that the angular distribution depends on M_{ee} . Therefore, our expectations of the fit parameters β_{CP} and γ_{CP} could change. In figure 10.4 we show ϕ for generated events with the M_{ee} cut. The top plot fits for β_{CP} and we obtain a value of -0.25 . The bottom plot fits for γ_{CP} and again we get a value consistent with

zero. This MC was generated without radiative corrections and with $\alpha_{K^*}^{\text{eff}} = -0.14$, our measured effective form factor.

10.1.2 Fitting the Acceptance Corrected Angular Distribution

After all cuts discussed in the chapter 6, including the $8\text{MeV}M_{ee}$ cut, 264 $K_L \rightarrow e^+e^-e^+e^-$ events remained that were used to fit for β_{CP} and γ_{CP} . The raw angular distribution is shown in the top plots of figures 10.5 and 10.6, where we show the folded ($0^\circ - 90^\circ$) and unfolded ($0^\circ - 180^\circ$) distributions respectively. The bottom plots in these figures show the acceptance as a function of ϕ . Again, the acceptance was calculated without radiative corrections and with $\alpha_{K^*}^{\text{eff}} = -0.14$, our measured effective form factor.

Next we correct the data for acceptance and fit for β_{CP} and γ_{CP} . Figure 10.7 shows these plots with the fits. From these fits we measure,

$$\beta_{\text{CP}} = -0.231 \pm 0.091_{\text{data}} \pm 0.021_{\text{mc}} \quad , \quad \gamma_{\text{CP}} = -0.093 \pm 0.085_{\text{data}} \pm 0.019_{\text{mc}}.$$

The dashed line in figure 10.7 shows the $CP = +1(K_1)$ prediction and further confirms that the decay proceeds predominantly through the $CP = -1(K_2)$ state.

To check these 2 and 1 sigma measurements of the β_{CP} and γ_{CP} terms respectively, we calculated the acceptance corrected asymmetry, defined as

$$\text{Asymmetry} = \frac{N^+ - N^-}{N^+ + N^-}. \quad (10.4)$$

For β_{CP} , N^+ is the number of events when $\cos(2\phi)$ is positive ($0^\circ \leq 2\phi \leq 90^\circ$) and N^- is the number of events when $\cos(2\phi)$ is negative ($90^\circ \leq 2\phi \leq 180^\circ$). For γ_{CP} , N^+ is the number of events when $\sin(2\phi)$ is positive ($0^\circ \leq 2\phi \leq 180^\circ$) and N^- is the number of events when $\sin(2\phi)$ is negative ($180^\circ \leq 2\phi \leq 360^\circ$). This gives us asymmetries of

$$\text{Asymmetry}(\beta_{\text{CP}}) = (-13.2 \pm 6.3_{\text{stat}})\%, \quad (10.5)$$

$$\text{Asymmetry}(\gamma_{\text{CP}}) = (-6.3 \pm 6.3_{\text{stat}})\%,$$

consistent with the measurements above. This is also consistent with the fact that the asymmetry is related to β_{CP} and γ_{CP} by

$$\text{Asymmetry}(\beta_{\text{CP}}) = \frac{N^+ - N^-}{N^+ + N^-} = \frac{2\beta_{\text{CP}}}{\pi} = (-14.6 \pm 5.7)\%, \quad (10.6)$$

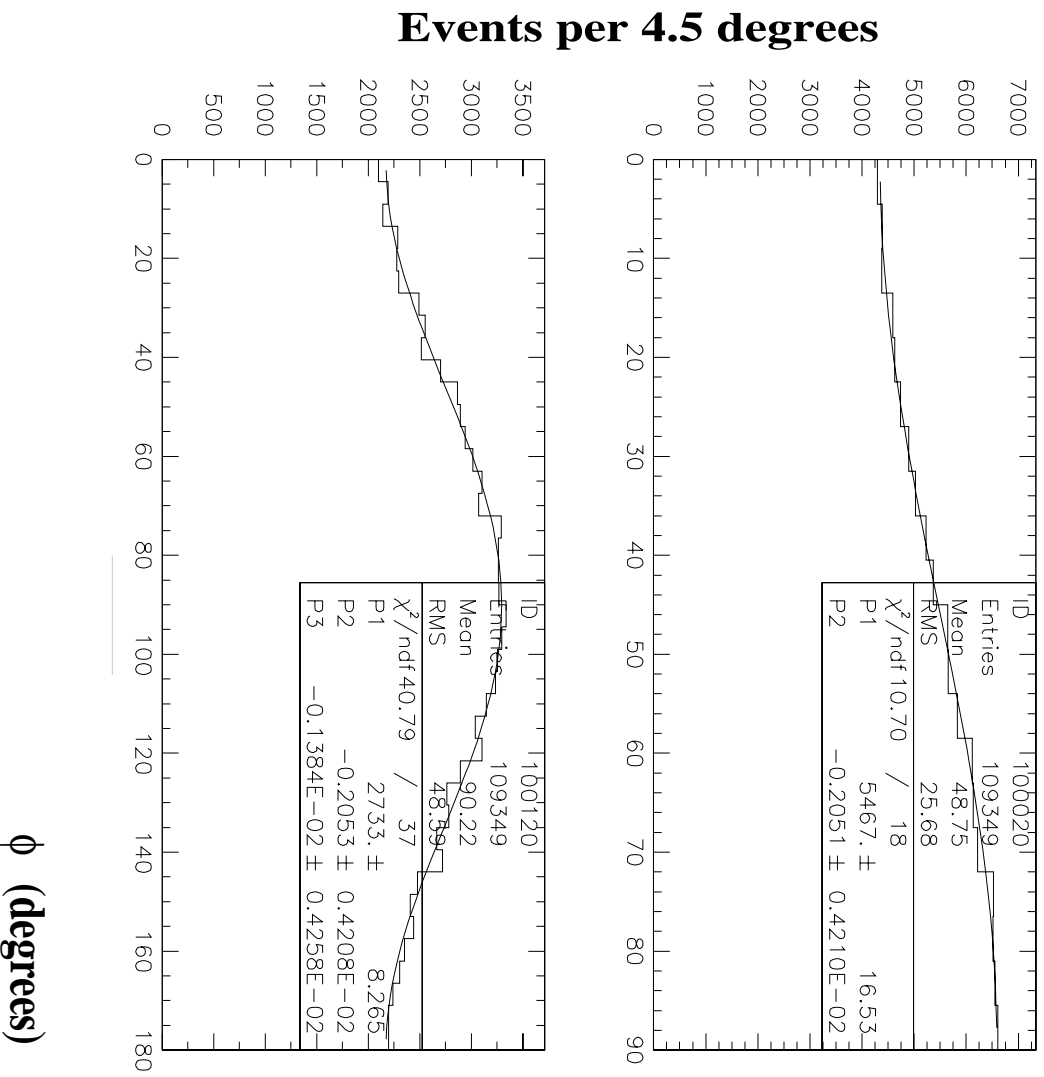


Figure 10.2: The angle ϕ for all generated events. The top plot fits for β_{CP} using equation 1.21 and we obtain the value of β_{CP} that we expect, -0.20. The bottom plot fits for γ_{CP} using equation 1.22 and we get zero, as expected.

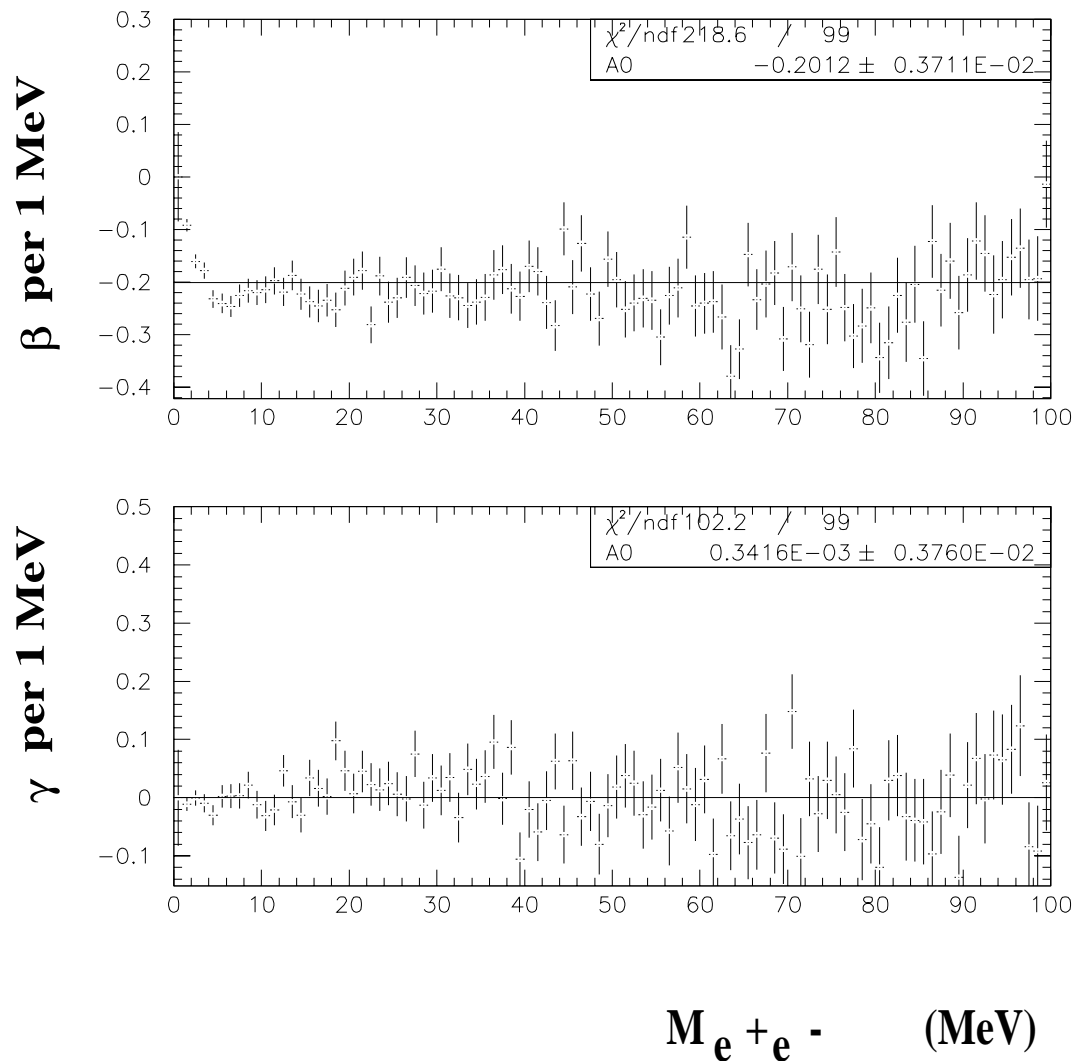


Figure 10.3: These plots come from signal MC at the generation level. We fit for β_{CP} and γ_{CP} in bins of M_{ee} (in MeV). We expect the MC to give us β_{CP} equal to -0.20 and γ_{CP} equal to zero when averaged over the whole M_{ee} range. The flat fit of these parameters as a function of M_{ee} yields the expected numbers. We also notice that β_{CP} , which tests the CP state of the system, approaches zero for small M_{ee} or small opening angles of the e^+e^- pairs, where parity starts becoming undefined. Also, γ_{CP} is generated flat over the whole M_{ee} range.

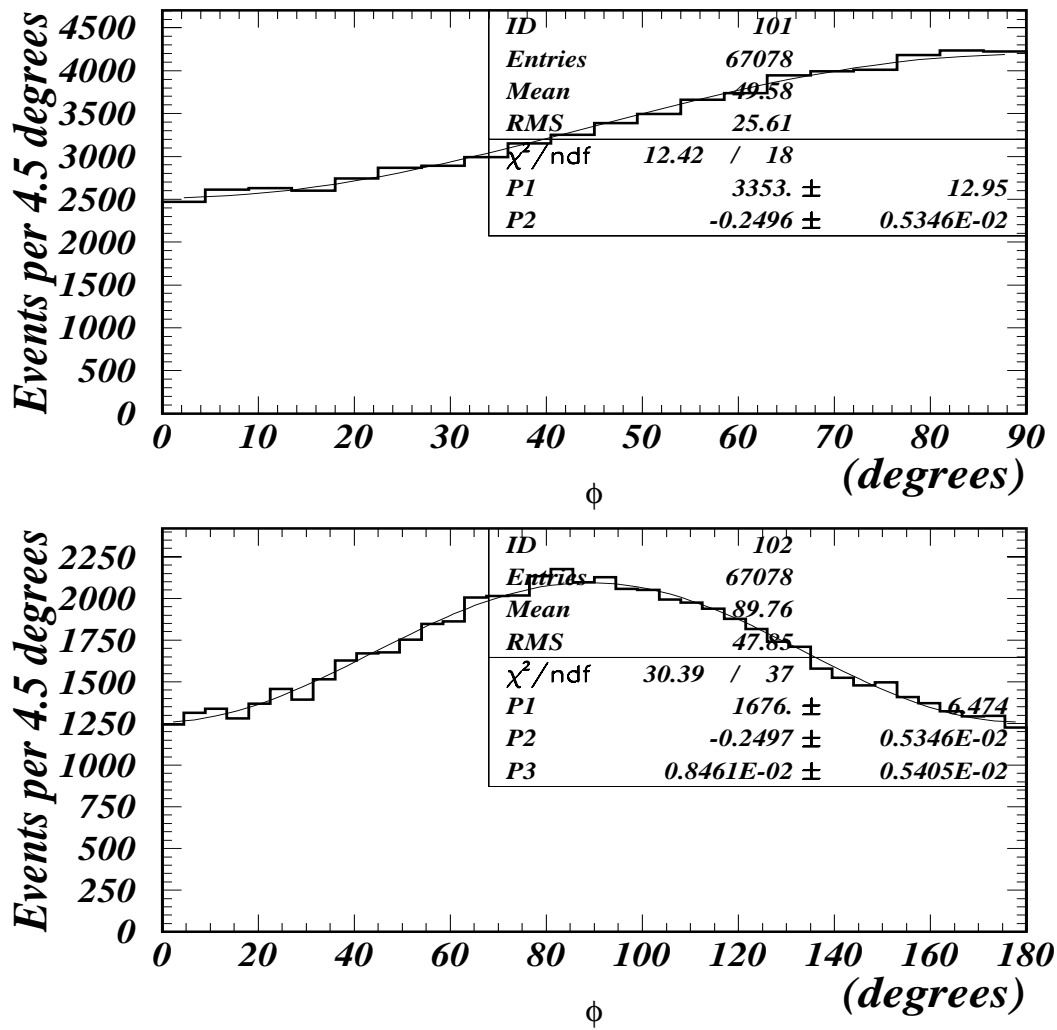


Figure 10.4: We show ϕ for generated events with the M_{ee} cut of 8 MeV. The top plot fits for β_{CP} and we obtain a value of -0.25. The bottom plot fits for γ_{CP} and again we get a value consistent with zero.

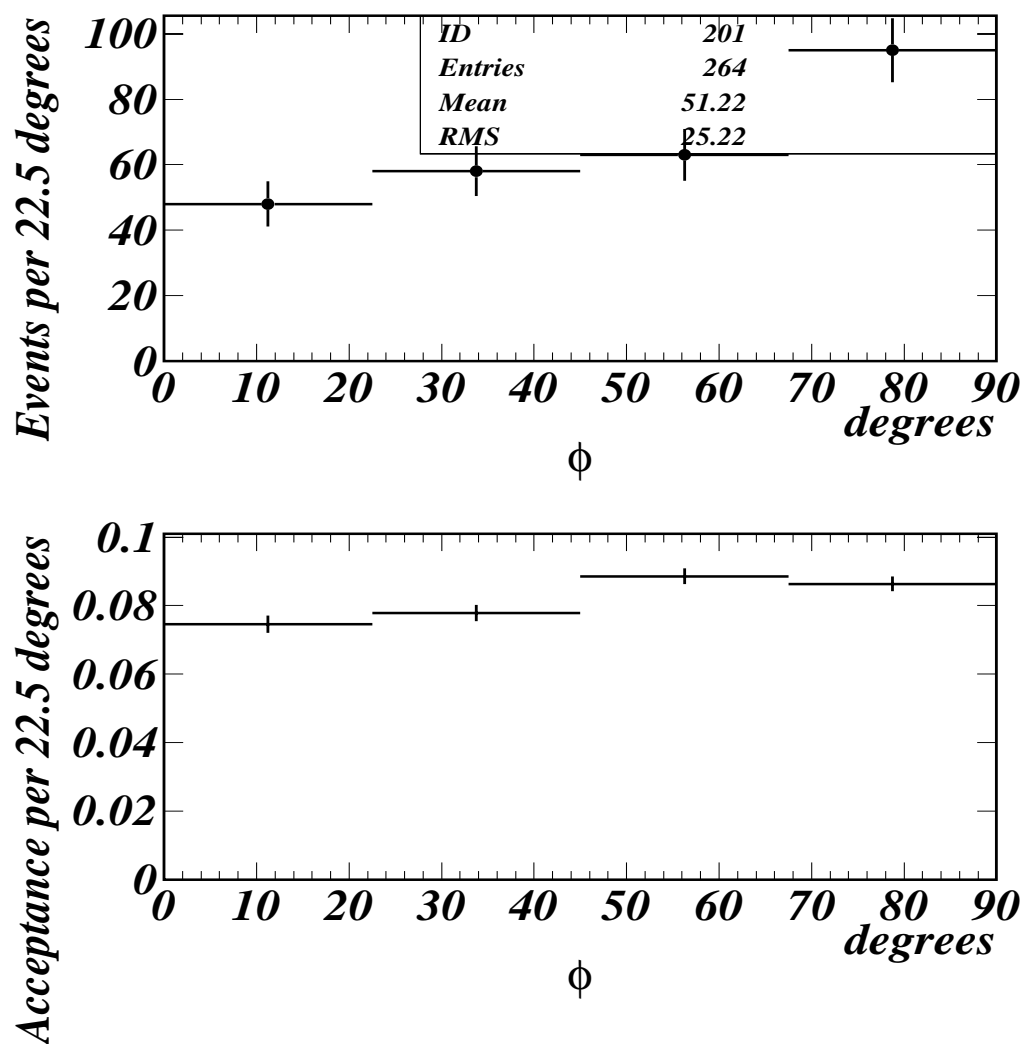


Figure 10.5: The top plot shows the angular distribution (folded) for the data, without acceptance correction. The bottom plot shows the acceptance as a function of the angle (folded).

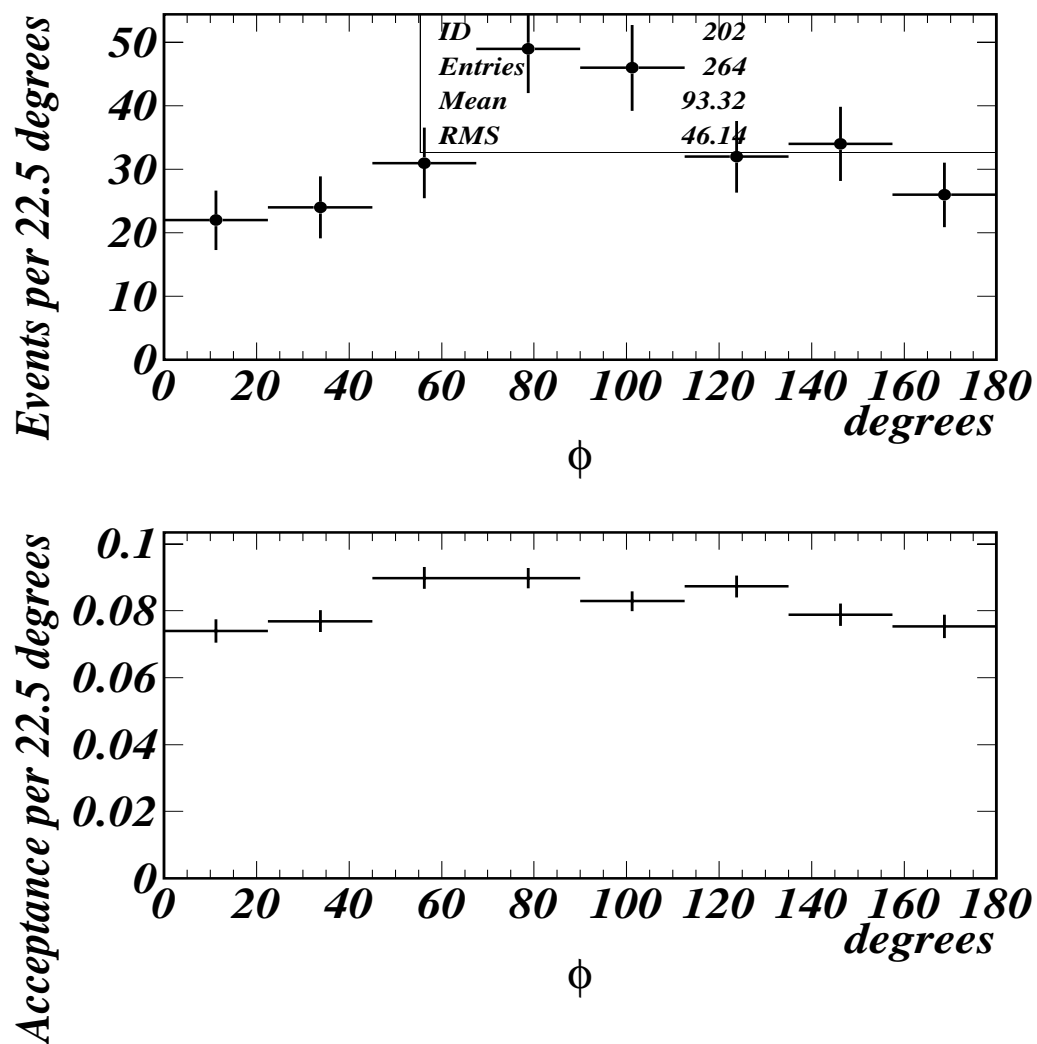


Figure 10.6: The top plot shows the angular distribution from $0^\circ - 180^\circ$ for the data, without acceptance correction. The bottom plot shows the acceptance as a function of the angle.

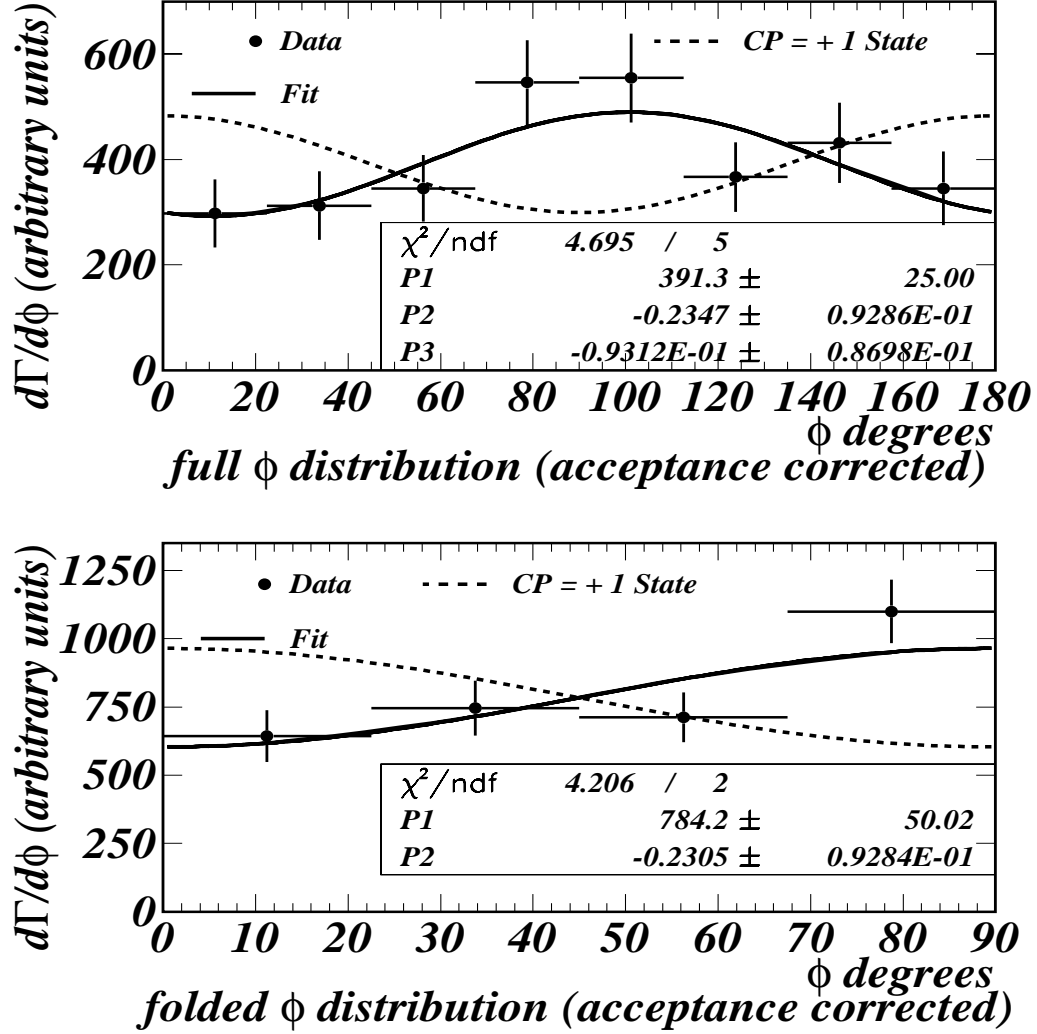


Figure 10.7: The distribution of the angle ϕ between the planes of the two e^+e^- pairs. In the bottom figure, the ϕ distribution from $90^\circ - 180^\circ$ is folded into $0^\circ - 90^\circ$. We fit these distributions to equations 1.21 and 1.22 and measure $\beta_{CP} = -0.23 \pm 0.09_{\text{stat}} \pm 0.02_{\text{syst}}$ and $\gamma_{CP} = -0.09 \pm 0.09_{\text{stat}} \pm 0.02_{\text{syst}}$. The errors on the fits are from data and MC statistics. The dashed line shows the $CP = +1(K_1)$ prediction and further confirms that the decay proceeds predominantly through the $CP = -1(K_2)$ state.

Table 10.1: β_{CP} and γ_{CP} with different MC used for acceptance. The MC error is the uncorrelated error.

MC used for Acceptance	β_{CP}	γ_{CP}
KTeV Rad corr and $\alpha_{K^*} = 0.03$	$-0.20 \pm 0.10_{\text{data}} \pm 0.03_{\text{mc}}$	$-0.09 \pm 0.09_{\text{data}} \pm 0.03_{\text{mc}}$
KTeV Rad corr and no FF	$-0.22 \pm 0.09_{\text{data}} \pm 0.03_{\text{mc}}$	$-0.10 \pm 0.08_{\text{data}} \pm 0.03_{\text{mc}}$
PHOTOS and no FF	$-0.21 \pm 0.09_{\text{data}} \pm 0.04_{\text{mc}}$	$-0.09 \pm 0.08_{\text{data}} \pm 0.03_{\text{mc}}$
No rad corr and no FF	$-0.22 \pm 0.09_{\text{data}} \pm 0.04_{\text{mc}}$	$-0.08 \pm 0.08_{\text{data}} \pm 0.03_{\text{mc}}$

$$\text{Asymmetry}(\gamma_{\text{CP}}) = \frac{N^+ - N^-}{N^+ + N^-} = \frac{2\gamma_{\text{CP}}}{\pi} = (-5.7 \pm 5.7)\%.$$

10.1.3 Systematic Studies for the $K_L \rightarrow e^+e^-e^+e^-$ Angular Distribution Analysis

Various systematic checks were done by splitting the data up into different samples, correcting for acceptance and then fitting. In figure 10.8 we fit for β_{CP} and γ_{CP} for various sets of data; the winter vs. the summer data; events when one of the four tracks went down the beam hole at the CsI and when no tracks go down the beam hole at the CsI; events that came from the east beam vs. the west beam; events that came from the top of the beam vs. the bottom of the beam. These plots also show how these parameters vary for different Monte Carlos used in the acceptance correction. For example, MC with KTeV radiative corrections [83] vs. radiative corrections using the PHOTOS package [82]. For the purposes of systematic studies, we also analyzed a MC sample generated with out radiative corrections and a MC with no accidental overlays. All the error bars in figure 10.8 are statistical and all points in this figure are consistent with each other. This gives us confidence that the systematic uncertainty is not large. The statistical error band is also shown in this figure. For reference, table 10.1 shows the fit values for β_{CP} and γ_{CP} with different MC used for acceptance, indicating an overall consistency.

Next, different variables were intentionally scaled thus inducing artificial slopes in data vs. MC comparisons, which were used to assign the systematic error. Table 10.2 shows how systematic errors were assigned by scaling.

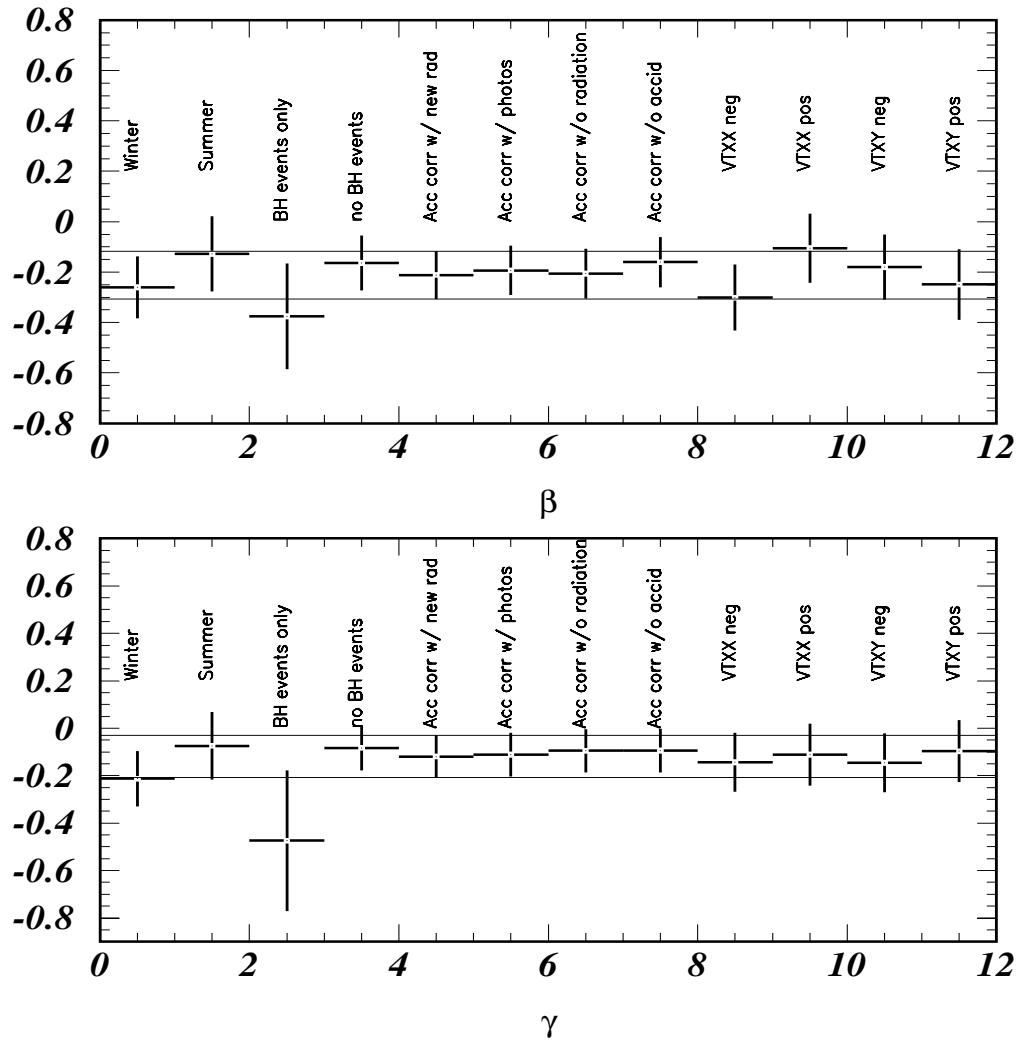


Figure 10.8: Some systematic checks on β_{CP} and γ_{CP} . The statistical error band is also shown in this figure. This figure shows fits for β_{CP} and γ_{CP} when we look at the winter vs. the summer data; events when one of the four tracks went down the beam hole at the CsI and when no tracks go down the beam hole at the CsI; events that came from the east beam vs. the west beam; events that came from the top of the beam vs. the bottom of the beam. These plots also show how these parameters vary for different Monte Carlos used in the acceptance correction. All the error bars in this figure are statistical and all points in this figure are consistent with each other. This gives us confidence that the systematic uncertainty is not large.

Table 10.2: Systematic Studies of Angular Distribution

Distrib.	orig. slope % per quantity	slope change % per quantity (arbitrary)	β_{CP}	syst error assigned	γ_{CP}	syst error assigned
Nominal	-	-	-0.231	-	-0.093	-
VTXZ (m)	-0.352 ± 0.388	0.382	-0.243	0.012	-0.105	0.012
TRKP fudge (GeV)	0.102 ± 0.180	0.334	-0.221	0.005	-0.075	0.010
ENERGCS fudge	$0.097+/-0.210$	0.295	-0.226	0.004	-0.073	0.014

Also, the track momenta and the cluster energies were smeared to get an understanding of how the uncertainty in the detector (DC, CsI) resolutions affect the fits to β_{CP} and γ_{CP} . Our uncertainty in the track momentum resolution yields a systematic uncertainty of 0.008 and 0.003 in β_{CP} and γ_{CP} respectively. Our uncertainty in the cluster energy resolution gives a systematic uncertainty of 0.002 and 0.007 in β_{CP} and γ_{CP} respectively.

10.1.4 Results of Angular Distribution Analysis

Summary of Errors of β_{CP} and γ_{CP}

The contributions to the errors for β_{CP} and γ_{CP} are summarized in table 10.3.

Table 10.3: Table of Errors on Angular Distribution Measurements

Error		in β_{CP}	in γ_{CP}
<i>Statistics</i>		0.093	0.087
<i>Systematic:</i>	Detector Acceptance/Spectrum	0.014	0.021
	Detector Resolution	0.008	0.008
	Time Dependence	-	-
	Accidentals	-	-
	<i>total internal systematic</i>	0.016	0.022

Results

With the present level of statistics in $K_L \rightarrow e^+e^-e^+e^-$ we see no evidence for direct or indirect CP violation. We measured

$$\beta_{\text{CP}} = -0.23 \pm 0.09_{\text{stat}} \pm 0.02_{\text{syst}} \quad , \quad \gamma_{\text{CP}} = -0.09 \pm 0.09_{\text{stat}} \pm 0.02_{\text{syst}}$$

in $K_L \rightarrow e^+e^-e^+e^-$, where β_{CP} is an indication of the CP eigenstate and γ_{CP} measures the amount of CP violation in the decay. These results are consistent with the hypothesis that the K_L is the $CP = -1$ (K_2) state. These parameters are insensitive to the form factor and to the inclusion of final state bremsstrahlung in the Monte Carlo.

As we discussed in section 10.1.1, the expectation for β_{CP} is -0.25 and the expectation for γ_{CP} is small. We also, for the first time, placed a limit on the value of γ_{CP} . The 90% CL limit on $|\gamma_{\text{CP}}|$ is < 0.21 .

For reference, the previous measurement was based on 27 events and did not include an explicit M_{ee} cut (1994):

$$\beta_{\text{CP}} = -0.22 \pm 0.30[38, 19].$$

We have an order of magnitude more statistics than the previous measurement and have done a factor of 3 better in the statistical error of β_{CP} . Also, this is the first time a limit has been placed on γ_{CP} .

Chapter 11

Conclusions

We observed 441 $K_L \rightarrow e^+e^-e^+e^-$ events with a background of 4.2 events, an increase in statistics of a factor of 16 compared to the previous most precise measurement [38, 19].

We measured the branching ratio of $K_L \rightarrow e^+e^-e^+e^-$ to be

$$B(K_L \rightarrow e^+e^-e^+e^-) = (3.72 \pm 0.18_{\text{stat}} \pm 0.10_{\text{syst}} \pm 0.20_{\text{norm}}) \times 10^{-8}.$$

(the last error is in the measurement of the normalization mode $B(K_L \rightarrow \pi^0\pi_D^0\pi_D^0)$ in the PDG). This result assumes a $K_L\gamma^*\gamma^*$ form factor parametrized by Bergström, Massó, and Singer (BMS) [1]. The theoretical models assuming a form factor show an increase in the branching ratio compared to a pointlike form factor (see table 1.2 in chapter 1). Given our statistical error in the branching ratio measurement, we cannot truly discriminate between the theoretical models with and without a form factor. However, we do observe a non-trivial form factor and believe that the branching ratio models including a form factor are favored. We conclude that our branching ratio measurement, our observation of a non-trivial form factor and the theoretical models including a form factor are consistent. Figure 11.1 shows the experimental measurements of the $B(K_L \rightarrow e^+e^-e^+e^-)$ over the years. This figure also includes the various predictions of the $B(K_L \rightarrow e^+e^-e^+e^-)$ as summarized in table 1.2.

We measured the BMS form factor parameter $\alpha_{K^*}^{\text{eff}} = -0.14 \pm 0.16_{\text{stat}} \pm 0.15_{\text{syst}}$, which takes into account both the form factor and radiative effects. This is the first measurement of the form factor parameter α_{K^*} using the decay $K_L \rightarrow e^+e^-e^+e^-$. Our result agrees well with the recent measurement of $\alpha_{K^*}^{\text{eff}} = -0.15 \pm 0.06_{\text{stat}} \pm 0.02_{\text{syst}}$ for the decay $K_L \rightarrow e^+e^-\gamma$ [42], also obtained by ignoring radiative corrections. As mentioned before, the effect of radiative corrections on α_{K^*} could be different in the two

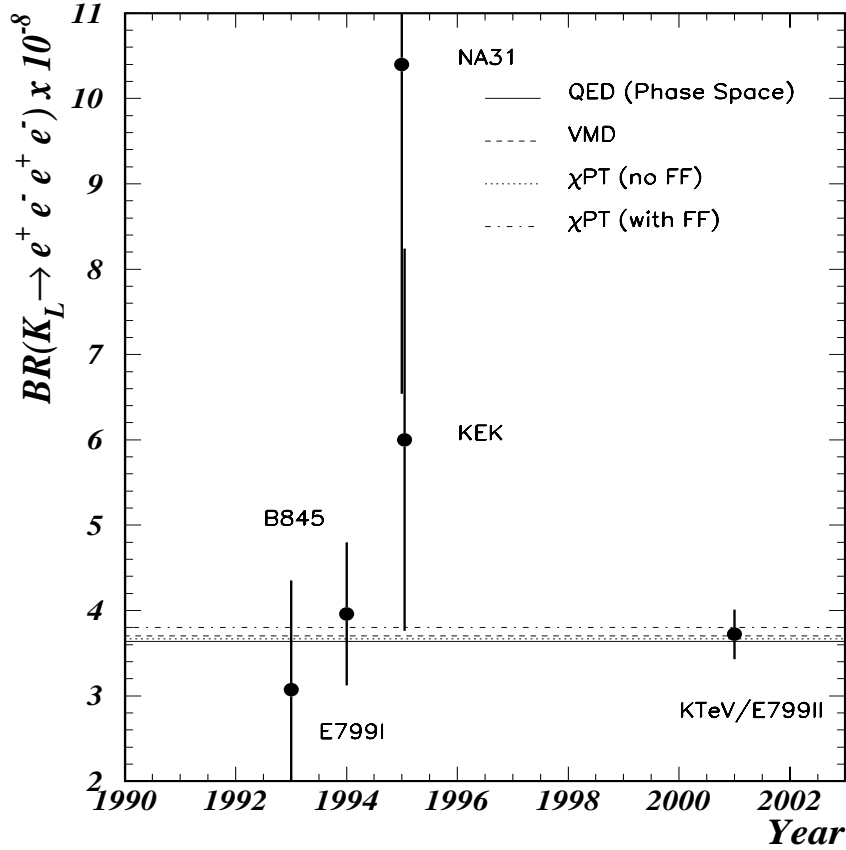


Figure 11.1: $B(K_L \rightarrow e^+e^-e^+e^-) (\times 10^{-8})$ vs. year. The lines represent the various predictions of the $B(K_L \rightarrow e^+e^-e^+e^-)$ as summarized in table 1.2. Given our statistical error in our branching ratio measurement, we cannot truly discriminate between the theoretical models with and without a form factor.

modes. A comparison of our result and the NA48 result of $\alpha_{K^*}^{\text{eff}}$ is shown in figure 11.2 (left); we see here that the two results agree well.

Disentangling radiative corrections, we measure $\alpha_{K^*} = 0.03 \pm 0.17_{\text{stat}} \pm 0.18_{\text{syst}}$ with $K_L \rightarrow e^+e^-e^+e^-$. The PDG world average of the $K_L\gamma\gamma^*$ form factor using $K_L \rightarrow e^+e^-\gamma$ is $\alpha_{K^*} = -0.33 \pm 0.05$. Our result agrees with the PDG average to within 1.4σ . The PDG average of α_{K^*} from the $K_L \rightarrow e^+e^-\gamma$ analyses and the result from this analysis are shown in figure 11.3; this figure illustrates the effect of a non-pointlike form factor on the x distribution. Also recall that $\alpha_{K^*} \simeq 0.3$ approximates a

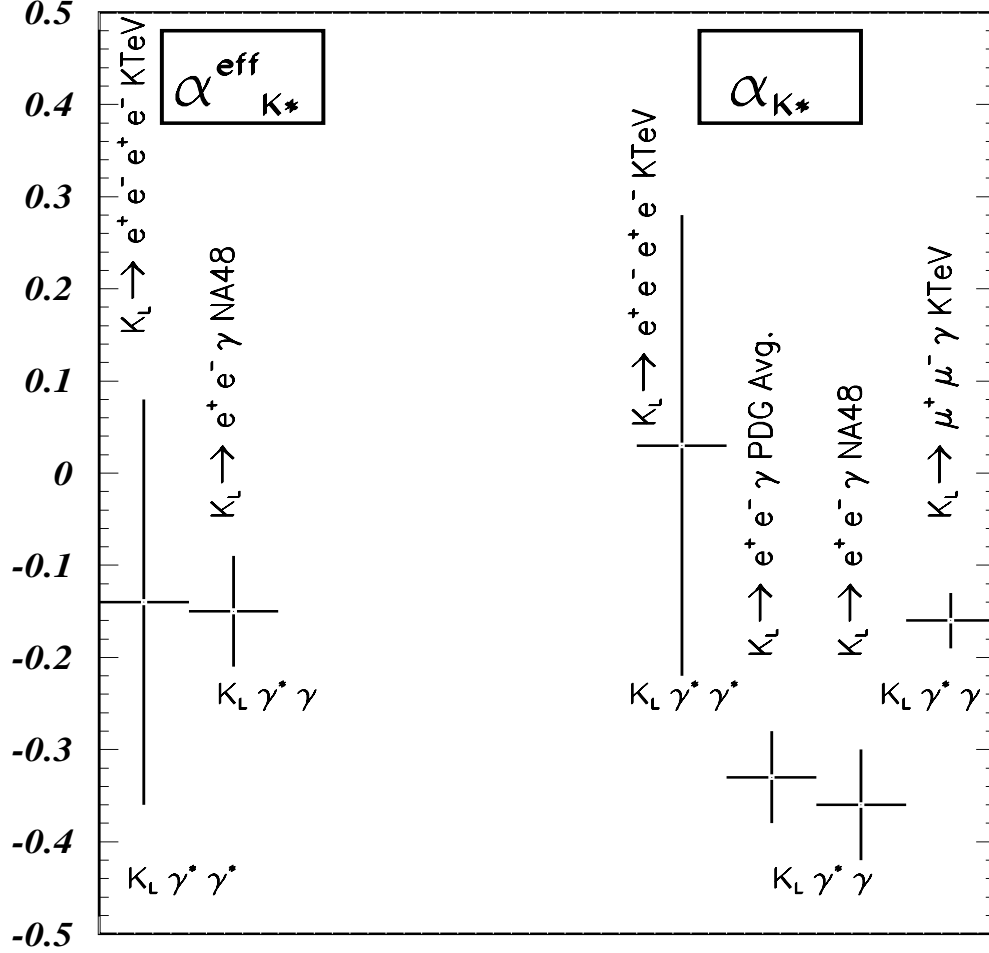


Figure 11.2: Left: A comparison of our result $\alpha_{K^*}^{\text{eff}} = -0.14 \pm 0.22$ for $K_L \rightarrow e^+e^-e^+e^-$ and the NA48 result $\alpha_{K^*}^{\text{eff}} = -0.15 \pm 0.06$ for $K_L \rightarrow e^+e^-\gamma$ [42]. We see here that the two results agree well. Right: A comparison of our result $\alpha_{K^*} = 0.03 \pm 0.25$ for $K_L \rightarrow e^+e^-e^+e^-$, the PDG world average using $K_L \rightarrow e^+e^-\gamma$, $\alpha_{K^*} = -0.33 \pm 0.05$ [10], the NA48 result using $K_L \rightarrow e^+e^-\gamma$, $\alpha_{K^*} = -0.36 \pm 0.06$ [42], and the recent KTeV result using $K_L \rightarrow \mu^+\mu^-\gamma$, $\alpha_{K^*} = -0.163^{+0.026}_{-0.027}$ [41]. Our result agrees with the PDG average to within 1.4σ and agrees well with the $K_L \rightarrow \mu^+\mu^-\gamma$ result. The average of the $K_L \rightarrow e^+e^-\gamma$ results and the recent result using $K_L \rightarrow \mu^+\mu^-\gamma$ [41] are different by 3σ . The reason for this electron-muon mode difference is not understood since the form factor should be independent of the final state. Also note that radiative effects are not important in $K_L \rightarrow \mu^+\mu^-\gamma$ but contribute significantly to $K_L \rightarrow e^+e^-\gamma$ and $K_L \rightarrow e^+e^-e^+e^-$.

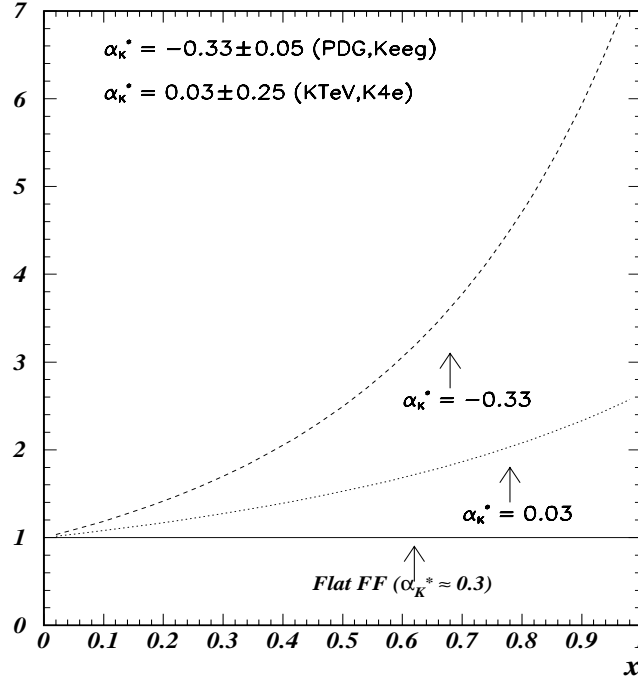


Figure 11.3: This figure shows the form factor as a function of x for different results of α_{K^*} , pointed to by the arrows. Shown are the PDG world average using the $K_L \rightarrow e^+e^-\gamma$ decay (dominated by the NA48 result $\alpha_{K^*} = -0.36 \pm 0.06_{\text{stat}} \pm 0.02_{\text{syst}}$ [42]) and our result for $K_L \rightarrow e^+e^-e^+e^-$. Compare these to a flat form factor shown. Our result agrees with the PDG average to within 1.4σ .

flat (or pointlike) form factor using a first order Taylor expansion. Figure 11.2 (right) shows a comparison of our result and other recent results for α_{K^*} . The average of the $K_L \rightarrow e^+e^-\gamma$ results and the recent result using $K_L \rightarrow \mu^+\mu^-\gamma$ [41] are different by 3σ . The reason for this electron-muon mode difference is not understood since the form factor should be independent of the final state. We hope in the near future that higher order terms of the radiative corrections for $K_L \rightarrow e^+e^-e^+e^-$ can be simulated so that the true form factor can be studied further. An improved experimental measurement of the $K_L\gamma^*\gamma^*$ form factor is essential to understand long distance contributions to other rare K_L decays, in particular $K_L \rightarrow \mu^+\mu^-$ [11, 12, 13, 14, 15].

Using the the distribution of the angle between the planes of the e^+e^- pairs, we measured

$$\beta_{\text{CP}} = -0.23 \pm 0.09_{\text{stat}} \pm 0.02_{\text{syst}} \quad , \quad \gamma_{\text{CP}} = -0.09 \pm 0.09_{\text{stat}} \pm 0.02_{\text{syst}}$$

in $K_L \rightarrow e^+e^-e^+e^-$, where β_{CP} is an indication of the CP eigenstate and γ_{CP} measures the amount of CP violation in the decay. These measurements are based on 264 events with M_{ee1} and M_{ee2} both $< 8\text{MeV}$. We have a tenfold increase in statistics compared to the previous measurement, improving the statistical error of β_{CP} by a factor of 3. This is the first measurement of γ_{CP} and we placed a 90% CL limit on $|\gamma_{\text{CP}}|$ of < 0.21 . The expectation for β_{CP} is -0.25 and for γ_{CP} zero, with M_{ee1} and M_{ee2} both $< 8\text{MeV}$. Although this is the largest sample of $K_L \rightarrow e^+e^-e^+e^-$ events observed so far, with the present level of statistics we see no evidence for direct or indirect CP violation.

Appendix A

Log Likelihood Method of Fitting for the Form Factor

In general, the likelihood is defined as

$$L(\alpha) = \prod_i f(x_i; \alpha), \quad (\text{A.1})$$

where the product is over all events, f is the probability density function normalized to unity, x_i are independent variables (phase space) describing the event and α is the set of unknown parameters. In our case, we have only one parameter, α_{K^*} . So for the likelihood and normalized probability density function we have:

$$L(\alpha_{K^*}) = \frac{\prod_{i=1}^N P_M^i(x_i; \alpha_{K^*}) P_a^i(x_i)}{[\int_{ps} P_M(x; \alpha_{K^*}) P_a(x) dx]^N}, \quad (\text{A.2})$$

where the product is over all events (N), $P_M(x; \alpha_{K^*})$ is a probability based on the matrix element [24] and is a function of all kinematic variables x , and $P_a(x)$ is the detector acceptance probability and is model independent. Notice that the denominator, integrated over the entire phase space, normalizes the likelihood. The steps leading to the likelihood function used to fit for the form factor parameter can be found in [49, 87]. The log of the likelihood function we used is:

$$\log(L(\alpha_{K^*})) = \sum_{i=1}^N \log(w_i(\alpha_{K^*})) - N \log(T(\alpha_{K^*})) - N \log(A(\alpha_{K^*})) \quad (\text{A.3})$$

where N is the number of events in our data sample, w_i is the weight of the i^{th} event and comes from the matrix element calculation in the KTeV MC, T is the total integral of the matrix element over the entire phase space, and A is the total detector acceptance. The value α_{K^*} that maximized the likelihood function for our data was our best estimate of this parameter. The statistical error came from a change of half a unit in the maximum log likelihood. As a check, we computed the minimum χ^2 as well.

The first term in the log likelihood function above came from the matrix element calculation used in the KTeV MC for each data event as a function of α_{K^*} . The second term, which is the total integral of the matrix element over the entire phase space as a function of α_{K^*} , is difficult to calculate analytically. Alternatively, we approximated this integral using a Monte Carlo integration technique. The third term, which is just the total acceptance as a function of α_{K^*} , was obtained by generating different sets of MC for different values of the parameter. These different MC sets were generated in a correlated fashion to minimize statistical fluctuations between the sets.

Appendix B

Fitting for BMS Form Factor Using the χ^2 method

As mentioned in chapter 8, we also computed a χ^2 between data and MC as a function of α_{K^*} . We chose the distribution $x_1 + x_2$ as shown in figures 8.1 and 8.2. In these figures the dots represent the data and the histogram represents the Monte Carlo with $f(x) = 1$.

A Poisson χ^2 was used to fit the data [88]. Again before fitting the data, 10 different samples the size of the data were analyzed and fit for α_{K^*} . The same 10 samples with α_{K^*} equal to -0.36 were used. Figure B.1 shows the fit value of α_{K^*} with the statistical error from the fit for the 10 samples. A fit to a line gives us -0.37 ± 0.06 , so we see that value of α_{K^*} was put in the MC is extracted by the fit, indicating no bias at the level of expected statistical error from data. We also know from this figure that the size of our statistical error of our measurement of α_{K^*} will be approximately 0.19. Figure B.2 shows the distribution of the fit value minus the expected value of -0.36. This distribution is then fit to a Gaussian. The mean of this distribution is 0.0 ± 0.06 . Both plots show that using a Poisson χ^2 reproduces the expected value of -0.36 without a bias.

The result from our data is shown in figures B.3 and B.4. These figures show the Poisson χ^2 as a function of α_{K^*} and $\alpha_{K^*}^{\text{eff}}$ for the $K_L \rightarrow e^+e^-e^+e^-$ data. Minimizing the χ^2 gives a value for α_{K^*} of $-0.02 \pm 0.20_{\text{stat}}$ and $\alpha_{K^*}^{\text{eff}}$ of $-0.16 \pm 0.18_{\text{stat}}$. These results are statistically consistent with the ones from the log likelihood analysis. Note that the statistical error from the log likelihood is slightly smaller than the one from the χ^2 , 0.17 versus 0.20 respectively.

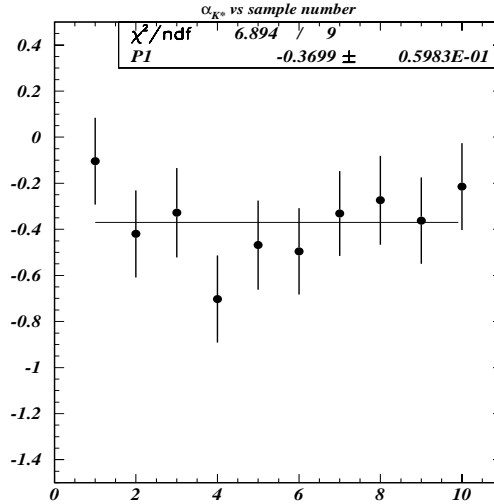


Figure B.1: This plot shows the fit value of α_{K^*} with the statistical error from the fit for the 10 samples using χ^2 . The MC samples contain a value of α_{K^*} of -0.36 and we fit -0.37 ± 0.06 (this is a factor of $\sqrt{10}$ less than our data statistics error using the χ^2 technique). This indicates no bias in the technique at the level of expected statistical error from data.

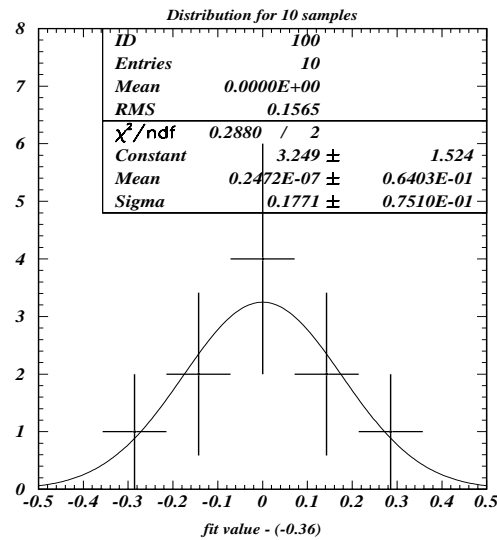


Figure B.2: The distribution of the fit value minus the expected value of -0.36 using χ^2 . This distribution is then fit to a Gaussian. We see the mean centered about zero and the sigma (RMS) is an indication of our expected data statistics error due to the χ^2 technique. This indicates that there is no bias in the technique at the level of expected statistical error from data.

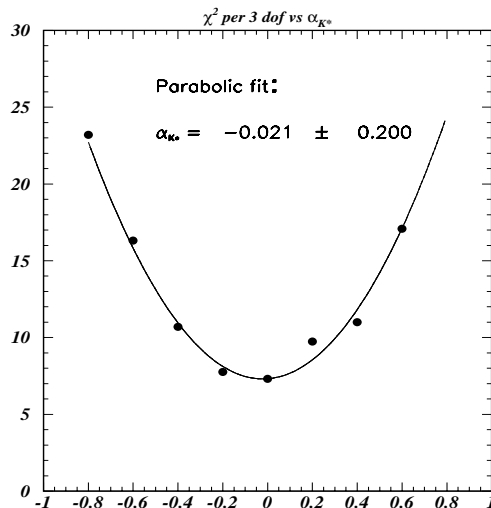


Figure B.3: This plot shows the Poisson χ^2 as a function of α_{K^*} for the $K_L \rightarrow e^+e^-e^+e^-$ data. Radiative corrections are included in the MC. Minimizing the χ^2 gives a value for α_{K^*} of $-0.02 \pm 0.20_{\text{stat}}$, consistent with the value from the log likelihood method (see figure 8.5).

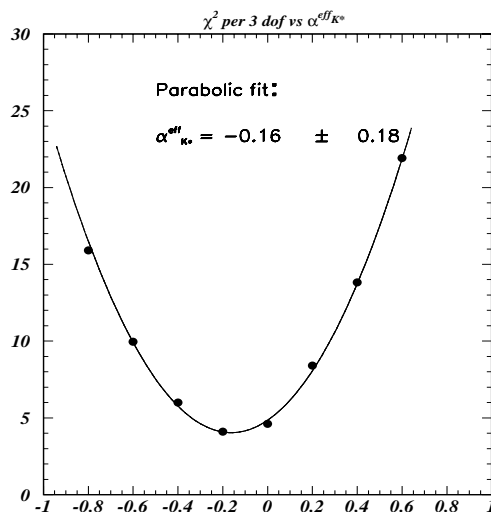


Figure B.4: This plot shows the Poisson χ^2 as a function of $\alpha_{K^*}^{\text{eff}}$ for the $K_L \rightarrow e^+e^-e^+e^-$ data. Radiative corrections have been excluded in the MC. Minimizing the χ^2 gives a value for $\alpha_{K^*}^{\text{eff}}$ of $-0.16 \pm 0.18_{\text{stat}}$, consistent with the value from the log likelihood method (see figure 8.6).

Appendix C

Fitting for the DIP Form Factor Using the χ^2 method

C.1 Fitting for the Linear Term α_{DIP}

The relation between the DIP and BMS parameters is $\alpha_{\text{DIP}} = -1 + 2.8 \alpha_{K^*}$. Therefore, our expected measurement of α_{DIP} , neglecting the β_{DIP} term, using our measurement of $\alpha_{K^*}(\alpha_{K^*}^{\text{eff}})$ above is -1.4(-1.4), using the χ^2 method. Figures C.1 and C.2 show the fit results from the data using the χ^2 method with and without radiative corrections in the MC. The χ^2 method gives $\alpha_{\text{DIP}} = -1.2 \pm 0.7$ and $\alpha_{\text{DIP}}^{\text{eff}} = -1.5 \pm 0.7$ as expected from the α_{K^*} and $\alpha_{K^*}^{\text{eff}}$ measurements. Comparing the log likelihood method results in section 8.1.2 we also see that the log likelihood method is a slightly more sensitive method as we saw before when fitting for the BMS form factor.

C.2 Fitting for the Quadratic Term β_{DIP}

Although we do not expect to be sensitive to the quadratic term β_{DIP} , we studied the effects of including this term. For simplicity the following studies were done using the χ^2 method and we also included the radiative corrections in the MC. Since the expected value for β_{DIP} is around +1 we set $\beta_{\text{DIP}} = 1.0$ in the MC and fit again for α_{DIP} . So, for $\beta_{\text{DIP}} = 1.0$, we measure $\alpha_{\text{DIP}} = -1.04 \pm 0.70$ and should be compared to $\beta_{\text{DIP}} = 0.0$, $\alpha_{\text{DIP}} = -1.20 \pm 0.66$. The 'uncorrelated' difference is less than 1σ .

To further check our sensitivity to β_{DIP} , both α_{DIP} and β_{DIP} were varied and a χ^2 between the data and MC was calculated. The results are shown in table C.1. Note that the χ^2 is only changing when the value of α_{DIP} changes. This is an indication of our insensitivity to β_{DIP} . As a final test, we fit for β_{DIP} for $\alpha_{\text{DIP}} = -1.20$, our measurement above. The fit for β_{DIP} is shown in figure C.3. The error on β_{DIP} is on

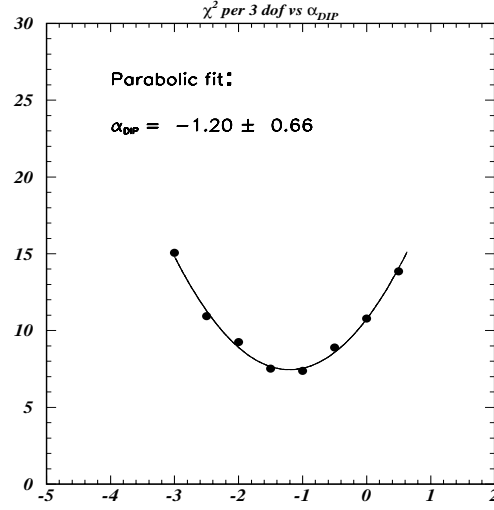


Figure C.1: This plot shows the Poisson χ^2 as a function of the DIP form factor parameter α_{DIP} (with $\beta_{\text{DIP}} = 0.0$) for the $K_L \rightarrow e^+e^-e^+e^-$ data. Minimizing the χ^2 gives a value for α_{DIP} of $-1.2 \pm 0.7_{\text{stat}}$, consistent with the value from the log likelihood (see figure 8.7).

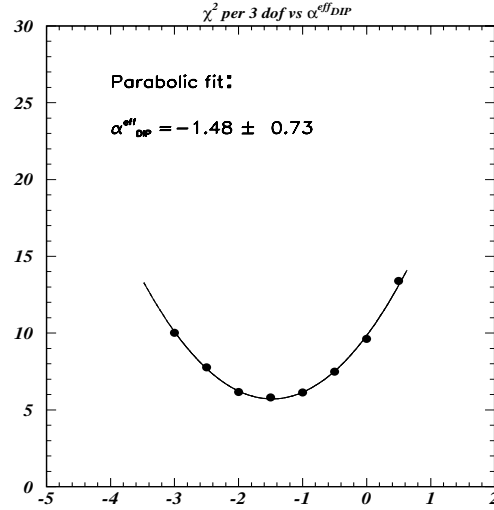


Figure C.2: This plot shows the Poisson χ^2 as a function of the DIP form factor parameter $\alpha_{\text{DIP}}^{\text{eff}}$ (with $\beta_{\text{DIP}} = 0.0$) for the $K_L \rightarrow e^+e^-e^+e^-$ data. Minimizing the χ^2 gives a value for $\alpha_{\text{DIP}}^{\text{eff}}$ of $-1.5 \pm 0.7_{\text{stat}}$, consistent with the value from the log likelihood (see figure 8.8).

the order of 35.0 on a parameter whose expectation is around 1.4. This without a doubt shows that $K_L \rightarrow e^+e^-e^+e^-$ is not sensitive to the DIP parameter β_{DIP} . In fact, to measure β_{DIP} to ± 1.0 we need about 1200 times more events since the error on 400 events is ± 35.0 . This means that to get a sensitivity of ± 1 on β_{DIP} we need around 500,000 $K_L \rightarrow e^+e^-e^+e^-$ events.

Table C.1: Table of DIP Form Factor Parameters vs. χ^2

α_{DIP}	β_{DIP}	χ^2 per 3 dof
-5.0	5.0	38.04
-5.0	1.0	37.35
-5.0	-3.0	37.05
-1.0	5.0	6.04
-1.0	1.0	6.04
-1.0	-3.0	6.37
3.0	5.0	78.90
3.0	1.0	78.90
3.0	-3.0	79.61

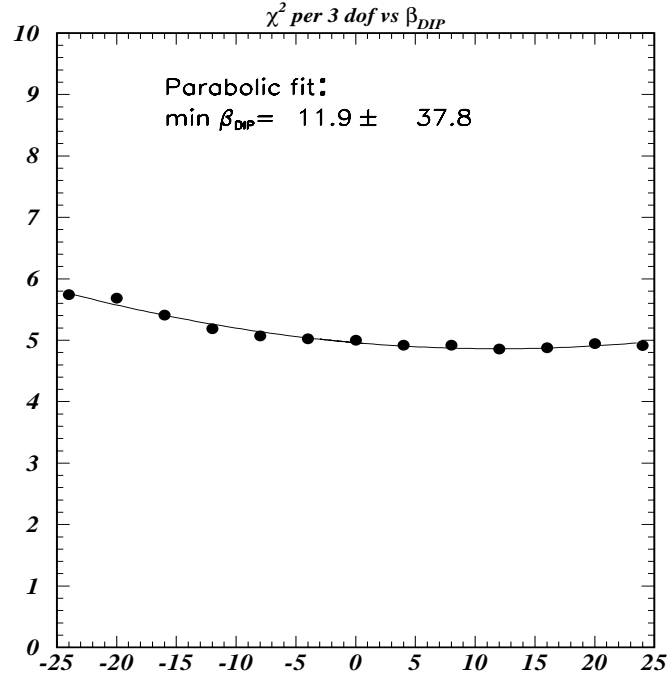


Figure C.3: This plot shows the Poisson χ^2 as a function of the DIP form factor parameter β_{DIP} (with $\alpha_{\text{DIP}} = 1.20$) for the $K_L \rightarrow e^+e^-e^+e^-$ data. Minimizing the χ^2 gives a value for β_{DIP} of $11.9 \pm 37.8_{\text{stat}}$. The expectation is around 1.4. This shows that $K_L \rightarrow e^+e^-e^+e^-$ is insensitive to the parameter β_{DIP} , a second order term.

Appendix D

Fitting for a Linear Form Factor Using the χ^2 method

A first order Taylor expansion of the $K_L \rightarrow e^+e^-e^+e^-$ form factors yields a generic linear form factor of the form $(1 + \alpha_{\text{Taylor}}(x_1 + x_2))$ as described in chapter 1. We obtain the approximate relations $\alpha_{\text{Taylor}} \approx 0.42 - 1.2\alpha_{K^*} \approx -\alpha_{\text{DIP}}/2.4$. Our expectations and measurements of α_{Taylor} are summarized in tables D.1 and D.2 respectively. We see that our measurements of α_{Taylor} and $\alpha_{\text{Taylor}}^{\text{eff}}$ agree with the expected values from our BMS and DIP form factor measurements.

Table D.1: Expected values of α_{Taylor} from measurements of α_{K^*} and α_{DIP} using the χ^2 method.

	Expected α_{Taylor} and $\alpha_{\text{Taylor}}^{\text{eff}}$
α_{K^*}	0.44
α_{DIP}	0.50
$\alpha_{K^*}^{\text{eff}}$	0.61
$\alpha_{\text{DIP}}^{\text{eff}}$	0.62

Table D.2: Measurements of α_{Taylor} and $\alpha_{\text{Taylor}}^{\text{eff}}$ using the χ^2 method. These measurements agree with the expected values from our BMS and DIP form factor measurements seen in table D.1.

	χ^2
α_{Taylor}	0.51 ± 0.30
$\alpha_{\text{Taylor}}^{\text{eff}}$	0.60 ± 0.34

References

- [1] L. Bergström *et al.*, Phys. Rev. Lett. **131**, 229 (1983).
- [2] W. Pauli, Nuovo Cim. **6**, 204 (1957).
- [3] G. D. Rochester and C. C. Butler, Nature **160**, 855 (1947).
- [4] C. S. Wu *et al.*, Phys. Rev. **105**, 1413 (1957).
- [5] T. D. Lee and C. N. Yang, Phys. Rev. **104**, 254 (1956).
- [6] J. H. Christenson, J. W. Cronin, V. L. Fitch, and R. Turlay, Phys. Rev. Lett. **13**, 138 (1964).
- [7] B. Winstein and L. Wolfenstein, Rev. Mod. Phys. **65**, 1113 (1993).
- [8] L. Wolfenstein, Nuovo Cim. **63 A**, 269 (1969).
- [9] K. Kleinknecht. *CP Violation*. edited by C. Jarlskog, (World Scientific, Singapore), page 41, 1989.
- [10] Particle Data Group, D. E. Groom *et al.*, Eur. Phys. J. C **15**, 395 (2000).
- [11] G. Bélanger and C. Q. Geng, Phys. Rev. D **43**, 140 (1991).
- [12] P. Ko, Phys. Rev. D **45**, 174 (1992).
- [13] L. Bergström *et al.*, Phys. Lett. B **249**, 141 (1990).
- [14] L. Bergström *et al.*, Phys. Lett. B **134**, 373 (1984).
- [15] G. D'Ambrosio, G. Isidori, and J. Portolés, Phys. Lett. B **423**, 385 (1998).
- [16] A. Alavi-Harati *et al.*, 'Branching Ratio Measurement of the Decay $K_L \rightarrow e^+e^-\mu^+\mu^-$ ', submitted to Phys. Rev. Lett. (April 2001).
- [17] A. Lath, KTeV Internal Note 747 ¹
- [18] P. Gu *et al.*, Phys. Rev. Lett. **76**, 4312 (1996).
- [19] P. Gu, Ph.D. thesis (Rutgers, The State University of New Jersey, January, 1995).
- [20] S. Adler *et al.*, Phys. Rev. Lett. **84**, 3769 (2000).
- [21] S. Adler *et al.*, Phys. Rev. Lett. **79**, 2204 (1997).
- [22] G. Buchalla and A. J. Buras, Nucl. Phys. **B548**, 309 (1999).

¹All KTeV Internal Notes are available at Fermilab.

- [23] A. Alavi-Harati *et al.*, 'Measurements of the Rare Decay $K_L \rightarrow e^+e^-e^+e^-$ ', accepted by Phys. Rev. Lett. (February 2001).
- [24] T. Miyazaki and E. Takasugi, Phys. Rev. D **8**, 2051 (1973). With a correction to the interference term (see [38, 19]).
- [25] N. M. Kroll and W. Wada, Phys. Rev. **98**, 1355 (1955).
- [26] Z. E. S. Uy, Phys. Rev. D **43**, 802 (1991).
- [27] Z. E. S. Uy, Phys. Rev. D **43**, 1572 (1991).
- [28] C. Quigg and J. D. Jackson, Preprint 18487, UCRL, unpublished, (1968).
- [29] L. Zhang and J. L. Goity, Phys. Rev. D **57**, 7031 (1998).
- [30] G. D. Barr *et al.*, Phys. Lett. B **240**, 283 (1990).
- [31] M. Spencer *et al.*, Phys. Rev. Lett. **74**, 3323 (1995).
- [32] K.E. Ohl *et al.*, Phys. Rev. Lett. **65**, 1407 (1990).
- [33] G. D. Barr *et al.*, Phys. Lett. B **259**, 389 (1991).
- [34] G. D. Barr *et al.*, Z. Phys. C **65**, 361 (1995).
- [35] M. R. Vagins *et al.*, Phys. Rev. Lett. **71**, 35 (1993).
- [36] T. Akagi *et al.*, Phys. Rev. D **51**, 2061 (1995).
- [37] T. Akagi *et al.*, Phys. Rev. D **47**, R2644 (1993).
- [38] P. Gu *et al.*, Phys. Rev. Lett. **72**, 3000 (1994).
- [39] R. Plano *et al.*, Phys. Rev. Lett. **3**, 525 (1959).
- [40] N. P. Samios *et al.*, Phys. Rev. **126**, 1844 (1962).
- [41] G. B. Quinn, Ph.D. thesis (The University of Chicago, June, 2000).
- [42] V. Fanti *et al.*, Phys. Lett. B **458**, 553 (1999).
- [43] P. L. Michelsons, Ph.D. thesis (The University of Colorado, December, 1999).
- [44] G. E. Graham, Ph.D. thesis (The University of Chicago, August, 1999).
- [45] K. Hanagaki, Ph.D. thesis (The University of Osaka, Japan, August, 1998).
- [46] E. D. Zimmerman, Ph.D. thesis (The University of Chicago, March, 1999).
- [47] A. Alavi-Harati, Ph.D. thesis (The University of Wisconsin, Madison, April, 1999).
- [48] P. S. Shawhan, Ph.D. thesis (The University of Chicago, September, 1999).
- [49] K. Senyo, Ph.D. thesis (The University of Osaka, Japan, December, 1999).
- [50] R. Coleman *et al.*, KTeV Internal Note 213.

- [51] A. Alavi-Harati *et al.*, Phys. Rev. Lett. **83**, 22 (1999).
- [52] D. A. Jensen and Y. B. Hsiung, KTeV Internal Note 124.
- [53] L. K. Gibbons, Ph.D. thesis (The University of Chicago, August, 1993).
- [54] R. A. Briere, Ph.D. thesis (The University of Chicago, June, 1995).
- [55] K. S. McFarland, Ph.D. thesis (The University of Chicago, March, 1994).
- [56] T. Barker and U. Nauenberg, KTeV Internal Note 102.
- [57] T. Barker and U. Nauenberg, KTeV Internal Note 132.
- [58] A. Roodman, KTeV Internal Note 403.
- [59] R. J. Yarema *et al.*, KTeV Internal Note 203.
- [60] K. Hanagaki and T. Yamanaka, KTeV Internal Note 177.
- [61] S. Schnetzer, KTeV Internal Note 191.
- [62] T. Alexopoulos, A. Erwin, and R. S. Kessler, KTeV Internal Note 207.
- [63] C. Bown *et al.*, KTeV Internal Note 298.
- [64] C. Bown *et al.*, Nucl. Instr. and Meth. **A369**, 248 (1996).
- [65] P. Shawhan, KTeV Internal Note 257.
- [66] V. O'Dell and T. Yamanaka, KTeV Internal Note 184.
- [67] I. Albuquerque, R. Kessler, and P. Shawhan, KTeV Internal Note 318.
- [68] The University of Virginia Group, KTeV Internal Note 501.
- [69] J. Graham, KTeV Internal Note 467.
- [70] E. Cheu and A. Roodman, KTeV Internal Note 239.
- [71] A. Roodman, KTeV Internal Note 575.
- [72] A. Roodman, KTeV Internal Note 482.
- [73] A. Roodman, KTeV Internal Note 577.
- [74] R. Brun *et al.*, *GEANT User's Guide*. CERN, Geneva (1985).
- [75] M. Pang, KTeV Internal Note 404.
- [76] A. J. Malensek, Preprint FN-341, FN-341A (errata), Fermilab, (1981).
- [77] H. A. Bethe, Phys. Rev. **89**, 1256 (1953).
- [78] W. T. Scott, Rev. Mod. Phys. **35**, 231 (1963).
- [79] J. D. Jackson. *Classical Electrodynamics*. New York: J. Wiley, (1975).

- [80] W. R. Nelson *et al.* *The EGS4 code system*. SLAC Report 265, (1985).
- [81] A. Roodman, KTeV Internal Note 317.
- [82] E. Barberio *et al.*, Preprint 7033, CERN-TH., (1993).
- [83] P. Toale, KTeV Internal Note 678.
- [84] K. O. Mikaelian and J. Smith, *Phys. Rev. D* **5**, 1763 (1972).
- [85] E. D. Zimmerman, *Nucl. Instr. and Meth.* **A426**, 229 (1999).
- [86] F. Leber *et al.*, *Phys. Lett. B* **369**, 69 (1996).
- [87] M. Arenton *et al.*, KTeV Internal Note 549.
- [88] Particle Data Group, D. E. Groom *et al.*, *Eur. Phys. J. C* **15**, 195 (2000).

Vita

Eva Halkiadakis

- 1990** Graduated from Edison Township High School, Edison, New Jersey.
- 1990-95** Attended Rutgers, The State University of New Jersey, New Brunswick, New Jersey. Majored in Physics and French.
- 1995** B.S., Rutgers, The State University of New Jersey.
- 1995-2001** Graduate research in Experimental High Energy Physics, Rutgers, The State University of New Jersey, New Brunswick, New Jersey.
- 1995-96** Graduate Assistance in Areas of National Need (GAANN) Fellow, Department of Physics and Astronomy, Rutgers, The State University of New Jersey, New Brunswick, New Jersey.
- 1996-98** Graduate Assistant, Department of Physics and Astronomy, Rutgers, The State University of New Jersey, New Brunswick, New Jersey.
- 1998-99** Graduate Assistance in Areas of National Need (GAANN) Fellow, Department of Physics and Astronomy, Rutgers, The State University of New Jersey, New Brunswick, New Jersey.
- 1999-2000** Teaching Assistant, Department of Physics and Astronomy, Rutgers, The State University of New Jersey, New Brunswick, New Jersey.
- 2001** Ph.D. in Physics and Astronomy, Rutgers, The State University of New Jersey.